Epitaxial Growth, Chemical Doping and Electronic Applications of Two-Dimensional Transition Metal Dichalcogenides

池, 賢九

Epitaxial Growth, Chemical Doping and Electronic Applications of Two-Dimensional Transition Metal Dichalcogenides

A thesis presented

by

Hyun Goo Ji

to

Interdisciplinary Graduate School of Engineering Sciences

of Kyushu University

for the degree of

Doctor of Philosophy

Kyushu University

Fukuoka, JAPAN

August, 2020

Abstract

Since the memorable discovery of graphene, enormous studies have been performed on atomically thin two-dimensional (2D) materials, such as zero-gap graphene, semiconducting transition metal dichalcogenides (TMDs), and insulating hexagonal boron nitride (h-BN). From the extensive research, many unique physical properties of these 2D materials have been revealed, and recently some of them can be synthesized in a controlled manner using chemical vapor deposition (CVD) method. Especially, the TMDs are known to have superior semiconducting transport property together with interesting electronic behavior, making them promising candidates for post-silicon electronics. However, in spite of the importance of preparation method to obtain highly crystalline and wafer-scale TMD semiconductors, still there are several issues to be solved, such as crystal defects including grain boundary. In this thesis, epitaxial growth of highly crystalline WS_2 using hydrogen gas is demonstrated. By strong reducing effect of hydrogen gas, crystal quality of WS_2 is obviously improved. In addition, by realizing epitaxial growth on c-plane sapphire, formation of grain boundary is significantly suppressed. The epitaxial growth resulted in atomically smooth stitching between merging grains and improved the chemical stability as well as electrical transport property.

C-plane sapphire is one of the most widely used growth substrate for the CVD growth of TMDs due to their similar hexagonal lattice structures. However, despite the importance of growth substrate in CVD synthesis, there is almost no report studying how the sapphire substrate changes the growth mechanism. Therefore, in this thesis, influence of c-plane sapphire on the growth behavior of WS_2 is investigated. More lattice strain was found to be induced in the epitaxially grown WS_2 grains by strong van der Waals interaction with underlying sapphire and it resulted in preferential overlayer deposition and photoluminescence (PL) quenching.

Most of semiconducting TMDs including MoS_2 and WS_2 show unipolar n-type electrical transport property. However, for practical applications, both p- and n-type transport materials are required. In this thesis, by using chemical doping technique, ambipolar CVD-grown WSe_2 is selectively converted to p- and n-type. The chemical doping significantly improved the effective carrier mobilities up to three to four orders of magnitude. Using p- and n-type doped WSe_2, a complementary metal-oxide-semiconductor (CMOS) was fabricated which shows outstanding performance. Finally, by combining chemical doping and lithography techniques, a p-n junction was fabricated within a single triangle grain of WSe_2 which shows clear rectification behavior and light response.

This thesis presents the studies on 2D TMDs from their bottom-up synthesis using CVD method to their application for advanced electronics, which proves the prospect potential of 2D materials in the coming era.

Table of Contents

Chapter 5. Chemical Control of Electrical Transport Polarity of Transition Metal Dichalcogenides for Advanced Electronics

Chapter 6. Conclusions and Future Outlook

Chapter 1

Introduction

1.1. Tow-dimensional (2D) Materials

1.1.1. Graphene

Since the memorable discovery of graphene in 2004 with its impressive electrical conductivity,[1] extensive studies have been done and accumulated so far. Graphene is a single layer of carbon sheet, in which the carbon atoms are connected in-plane by covalent bond and additional π bond while having no chemical bond in the out-of-plane direction (Figure 1.1a). When graphene layers are stacked, only weak van der Waals interaction between layers holds their layered structure. A. K. Geim and K. S. Novoselov used an adhesive tape to detach pieces of graphene layers from the bulk graphite and measured their electrical property. The monolayer graphene with subnanometer thickness showed very high carrier mobility ~200,000 cm^2/Vs, and this attracted huge attention from researchers.[2] Since this discovery, many theoretical and experimental studies with interesting expectation and measurement were reported for several years. In spite of the superior physical properties of graphene, however, there was a lacking point in graphene that is the gapless nature. Having high electrical and thermal conductivities[3] together with mechanical flexibility and transparency,[3] graphene can be used for various applications in electronics. However, graphene does not have a band gap so that it is difficult to be used for semiconducting devices. Therefore, by the dedication of

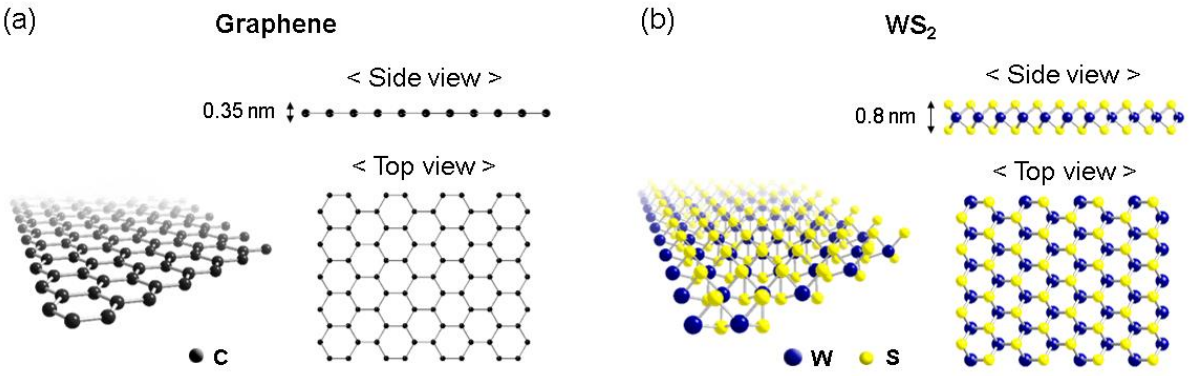

Figure 1.1. Schematics of crystal structures of (a) graphene and (b) tungsten disulfide (WS_2).

many researchers, several methods have been studied to open the band gap in graphene. First, applying top and bottom dual electrical field to AB stacked bilayer (2L) graphene and ABC stacked trilayer (3L) graphene was found to open a tunable band gap (up to 250 meV for bilayer).[4,5] Second, by confining the lateral size of graphene down to 10 ~ 100 nm which is called a nanoribbon, small band gap can be opened (~200 meV at 20 nm width).[6] Third, by inducing lattice strain manually or using epitaxial substrate, such as SiC, the sublattice symmetry of graphene can be broken, opening the band gap (~300 meV under 1% tensile strain[7], ~260 meV on SiC[8]). Also, hydrogenation or chemical substitution doping can be used to break the sublattice symmetry of graphene and open a small band gap.[9–12] Formation of heterostructure with hexagonal boron nitride (h-BN) was also found to open a small band gap by forming superlattice structure.[13,14] Thanks to the huge amount of research for more than a decade, now band gap can be opened in graphene. However, there are still critical limitations of them, because most of the methods need extremely delicate experimental manipulation, and the size of the band gap is too small to be used in semiconducting devices. As a result, research interest was extended from graphene to other atomically thin two-dimensional materials which have an intrinsic semiconducting nature.

1.1.2. Transition metal dichalcogenides (TMDs)

Transition metal dichalcogenides (TMDs) have a MX_2 composition with transition metal (M), such as Mo and W, and chalcogen (X), such as S, Se, and Te. Monolayer TMDs consist of a single layer of transition atom sheet which is sandwiched by single layers of chalcogen sheet (Figure 1.1b). Since the first demonstration of good semiconducting transport property of monolayer MoS_2,[15] TMDs have attracted great attention. Thus, other TMDs, such as WS_2, $MoSe_2$, WSe_2, $MoTe_2$, WTe_2 have also received great attention, and a lot of their interesting physical properties have been reported so far. The biggest distinguishing property of TMDs from the graphene is that they have a sizable band gap.[16] Depending on atomic composition, TMDs have different band gaps, as shown in Figure1.2.[17] Due to this semiconducting property, TMDs can be used for various applications in electronics and optoelectronics, such as switching transistors, logic gates, sensors, energy harvesting, light emitting diode, and so on.[18–20]

Similar to graphene, in the beginning of research, mechanical exfoliation method was widely used to prepare TMD flakes. Using this method, physical properties of various TMD

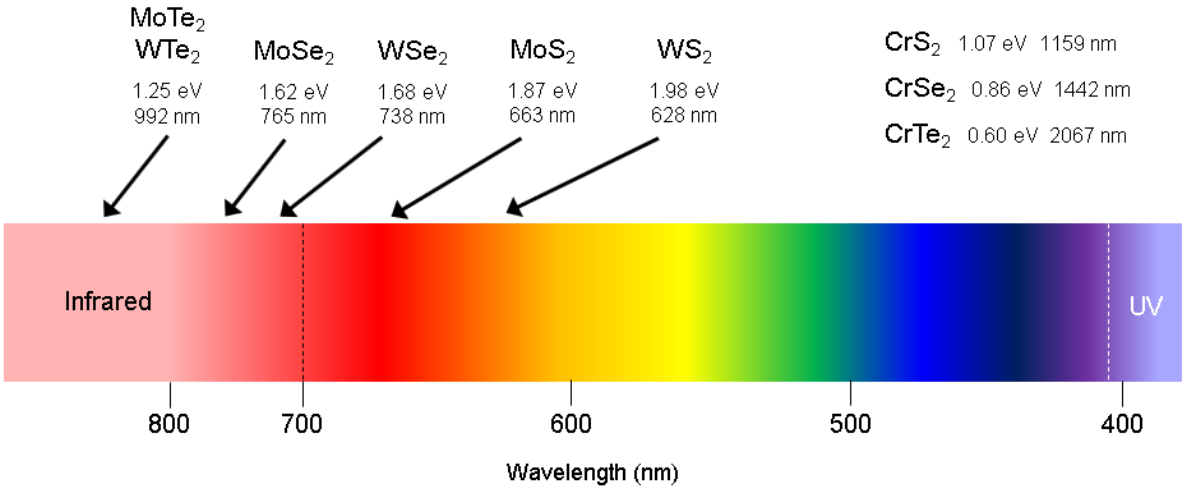

Figure 1.2. Band gap energy and corresponding wavelength of representative semiconducting monolayer transition metal dichalcogenides.

materials were well studied and diverse electronic and optoelectronic devices were fabricated and investigated. As the research advances, however, necessity for large size TMD crystals with uniform thickness became strong, because the exfoliated crystals have a limit in their crystal size and thickness uniformity. Therefore, bottom-up synthesis using chemical vapor deposition (CVD) method was introduced also for TMDs.[21] Using CVD method, it became possible to synthesize various TMD crystals by choosing suitable precursors and substrates. However, it accompanies prolonged effort to successfully grow the desired materials. For example, there are many growth parameters which need to be optimized, such as growth temperature, time, pressure, the balance between amount of each precursor, position of growth substrate, and etc. More details about the CVD method are explained in the following chapter. From devoted works by researchers,[22–27] CVD technology has been dramatically developed and the size of grown crystal has been scaled up to millimeter size.[28,29] Thanks to the CVD technology, TMD research has further advanced, fabrications of wafer scale logic circuits and transistor arrays have been reported recently.[30–33]

Compared with typical three dimensional (3D) semiconducting materials, such as Si, Ge, and InGaAs, TMDs have a notable superiority in their physical properties. In modern society, field-effect transistor (FET) is the basis of the information storage and processing. To increase the storage capacity and processing speed, the channel length of FET device needs to be shortened. However, in case of typical 3D semiconductors, as the channel length becomes shorter, the electrons finds it harder to travel through the channel as the imperfection of crystal structure scatters their flow. In contrast, in case of two dimensional (2D) semiconductors, they have a limited vertical thickness which is decided by the number of layers, and a flat lateral surface allows smooth electron flow with less scattering. Therefore, the advantage of 2D semiconductors against the short channel effect in FET application together with other superior physical properties, make TMDs a promising candidate for post-silicon electronics, although

this research is in an early stage yet.[34]

1.1.3. Heterostructures

For special purposes, more than two different 2D materials are combined in a controlled manner, which is called heterostructure. By stacking different materials one to another, vertical heterostructure can be formed (Figure 1.3a). Thanks to the unique layered structure of 2D materials, each layer can be easily detached and stacked. Vertical stacking is useful when forming material junctions. By stacking p-type or ambipolar layer (WSe_2 or $MoSe_2$) on n-type layer (WS_2 or MoS_2), a p-n junction is easily formed (Figure 1.3b).[35–38] Also, stacking of metallic (graphene) and semiconducting (WS_2) layers simply forms the metal-semiconductor junction.[18] Furthermore, the relative stacking orientation between upper and

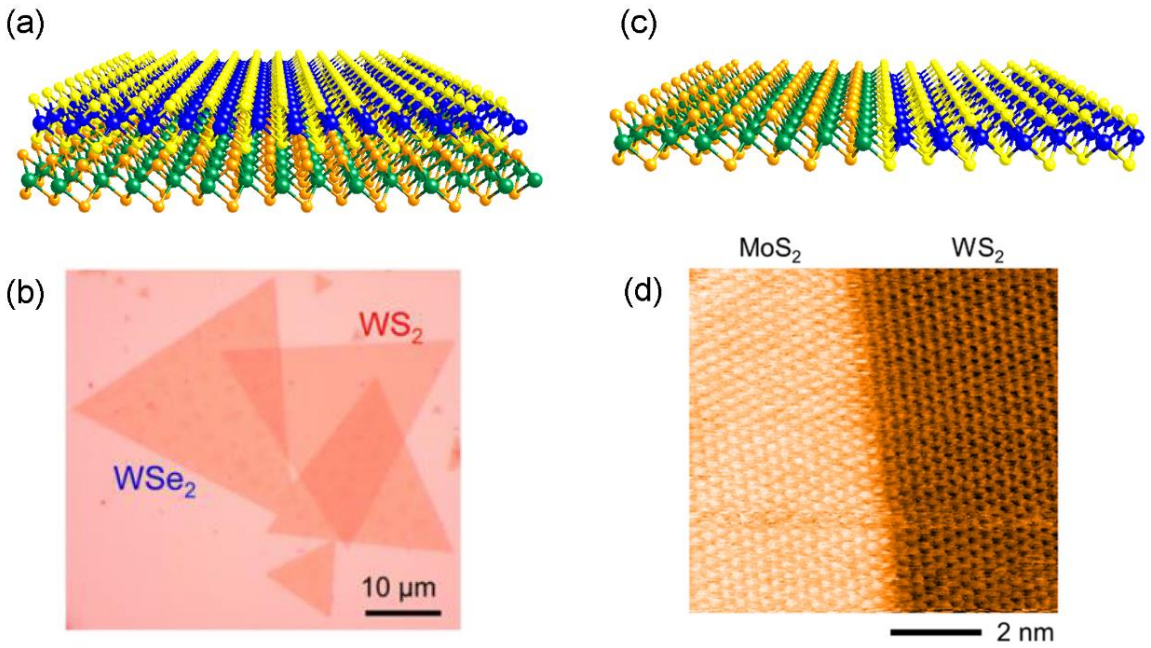

Figure 1.3. (a,c) Illustrations of (a) vertical- and (c) in-plane-heterostructures of TMDs. Blue, green spheres correspond to transition metals and yellow, orange spheres correspond to chalcogen atoms. (b) Optical micrograph of WSe_2/WS_2 stacked heterostructure on SiO_2/Si. (d) Scanning tunneling microscope image of MoS_2/WS_2 in-plane heterostructure. Figure1.3(b) and (d) are reproduced from Ref. 38 and 48, respectively.

lower layers is known to effectively change the interlayer interaction.[38–41] For example, when MoS_2 is stacked on graphene forming MoS_2-graphene heterostructure, the optical property of MoS_2 is strongly affected by the relative orientation with the underlying graphene.[42] More notably, some vertical heterostructures show appearance of new physical property, such as superconductivity or phase change at specific stacking configuration, which disappears when stacking configuration is altered.[43–46] There is also an in-plane heterostructure (Figure 1.3c). In-plane heterostructures can be formed by consecutive growth of different materials. For example, by switching the precursor species from W and S to Mo and S during the growth, it is possible to make WS_2-MoS_2 in-plane heterostructure (Figure 1.3d).[47–49] In a similar way, by performing consecutive growth of graphene and MoS_2, graphene-MoS_2 heterostructure can be formed.[24] Recent development of metal-organic CVD system made it easier to form in-plane TMD heterostructures.[48] Heterostructure itself is a very interesting research topic not only because of their usefulness in forming material junctions, but also because of the appearance of new physics with orientation-dependent tunability.

1.2. Motivation

As described in the previous section, superior physical properties of TMDs have attracted great attention from researchers. As a result, a number of studies have been reported on the characterization and CVD synthesis of TMD materials. With the advance of research, need for uniform and large size TMD crystals became stronger, because the mechanically exfoliated flakes are too small and lack of thickness uniformity. Therefore, CVD growth technique rapidly developed for last several years and now millimeter size of single crystals can be synthesized.[28,29] To fully extract the superior property of TMDs, the crystallinity of materials

must be high enough. However, compared with exfoliated ones, CVD-grown TMD grains contain much higher density of structural defects and, consequently, CVD-grown TMDs show lower device performance compared with exfoliated counterparts.[50–52] Therefore, this crystallinity issue in CVD-grown TMDs needs to be improved. In electronic and optoelectronic applications, wafer-scale TMD films are required to fabricate devices in more systematic manner. For this, CVD method has already proved their capability of growing wafer scale continuous films of various TMDs.[53,54] Although large-scale TMD films could be grown by CVD, still there is a grain boundary issue. During growth, as the grains are nucleated and their lateral size gradually increases, the neighboring grains start to touch each other and finally become merged. When the neighboring grains are merged, their crystal structures are deformed along the boundary, which is called grain boundary (GB). GBs are known to cause severe property variation and degradation.[55,56] Therefore, suppressing the formation of GBs is an important issue in improving the quality of CVD-grown materials, and it can be realized by aligning the crystal orientation of grains on the substrate. In this thesis, by using H_2 gas which has a strong reducing effect on the surface of growth substrate (c-plane sapphire), epitaxial growth was achieved which effectively suppressed GB formation. The smooth stitching between merging grains was found to improve the chemical stability and electrical transport properties on the merged grains. The atomic structures of merged interfaces were studied in detail using scanning transmission electron microscopy (STEM).

To realize the CVD growth of highly crystalline large size single crystal TMD films, extensive effort has been devoted by many researchers. There are many numbers of CVD growth parameters, such as reaction temperature, time, precursor, carrier gas, and substrate. In previous literatures, many parameters have been investigated to understand how they affect and change the resulting TMDs.[57–60] In case of growth substrate, the most widely used ones are c-plane sapphire and silicon oxide. The c-plane sapphire has a hexagonal lattice structure

same as MoS_2 and WS_2,[61] therefore, it is expected that this similarity of lattice structures would influence the growth behavior of TMD crystals on it. However, still there is almost no study about this. Thus, in this thesis, I investigated how the c-plane sapphire influences and changes the growth of WS_2. Due to the similar hexagonal lattice structure of c-plane sapphire and WS_2, more lattice strain was found to be induced in epitaxially grown grains by strong van der Waals interaction. This large strain caused preferential overlayer deposition on the epitaxial WS_2 grains. Low-temperature optical study revealed that photoluminescence (PL) is strongly quenched in epitaxially grown WS_2 grains by interaction with the underlying sapphire.

To realize practical device applications of semiconducting TMDs, such as logic circuits and a p-n junction, both p- and n-type materials are required. However, most of TMDs (MoS_2, WS_2, $MoSe_2$, WSe_2) are known to have n-type or ambipolar transport properties and p-type materials are scarce.[62] Therefore, various methods have been proposed to convert their electrical transport property to p-type, and the representative ones are the chemical doping,[62,63] substitutional doping,[64–66] metal nanoparticle deposition[67], and tuning Schottky barrier by changing metal electrode.[68,69] There are several methods to achieve the substitutional doping, such as post-growth or during-growth processes, however, most of them cause severe degradation of the semiconducting property.[64–66] Deposition of metal nanoparticles was found to be effective to convert the transport polarity to p-type.[67] But the nanoparticles degrade the optical property of underlying TMDs, which is critical for optoelectronic applications. Metals have different Fermi levels so that the use of different metal as an electrode can be employed to tune the electrical transport behavior of TMD channels.[68,69] However, in this case, fabrication process becomes complicated requiring deposition of different metals for each TMD. In contrast, chemical doping does not degrade semiconducting and optical properties, and moreover, its experimental process is relatively simple as compared with other methods. Actually, some exfoliated TMDs were well

converted to p-type by chemical doping.[62] However, when considering the higher density of chalcogen vacancy defects in CVD-grown TMDs compared with exfoliated flakes which causes n-type doping, it is more difficult to convert their carrier transport to p-type. Thus, in this thesis, chemical doping method is used to control the electrical transport polarity of CVD-grown WSe_2. Two different dopant molecules, 4-nitrobenzenediazonium tetrafluoroborate (4-NBD) and diethylenetriamine (DETA), were used for p- and n-type doping, respectively, and it was found that the effective carrier mobilities increase up to three to four orders of magnitude after each doping treatment. Using p- and n-type doped WSe_2, fabrication of a complementary metal-oxide-semiconductor (CMOS) circuit was demonstrated, showing good performance. In addition, by combining our chemical doping and lithography techniques, a p-n junction was fabricated within a single triangle grain of WSe_2, with clear rectification behavior as well as light response.

1.3. Outline of thesis

This thesis covers three main parts, CVD growth of high quality epitaxial WS_2, investigation of influence of c-plane sapphire on growth behavior of WS_2, and chemical doping of CVD-grown WSe_2 for controlling its electrical transport polarity and their device applications. Before discussing the experimental result in the main parts, basic introduction about 2D materials has been given in this Chapter (Chapter 1). For better understanding of experimental result in Chapters 3 to 5, more detailed background about physical properties and preparation methods of TMD materials are described in Chapter 2. Chapter 3 presents the epitaxial growth of high quality WS_2 using H_2 gas. In Chapter 4, influence of c-plane sapphire substrate on the growth behavior of WS_2 is investigated. Chapter 5 describes the chemical

doping of CVD-grown WSe_2 for controlling its electrical transport polarity where significantly improved carrier mobilities as well as fabrication of advanced electronic devices are demonstrated. Finally, this thesis is closed with conclusions and future outlook in Chapter 6.

References

(1) Novoselov, K. S. Electric Field Effect in Atomically Thin Carbon Films. *Science* **2004**, *306*, 666–669.

(2) Bolotin, K. I.; Sikes, K. J.; Jiang, Z.; Klima, M.; Fudenberg, G.; Hone, J.; Kim, P.; Stormer, H. L. Ultrahigh Electron Mobility in Suspended Graphene. *Solid State Commun.* **2008**, *146*, 351–355.

(3) Pop, E.; Varshney, V.; Roy, A. K. Thermal Properties of Graphene: Fundamentals and Applications. *MRS Bull.* **2012**, *37*, 1273–1281.

(4) Zhang, Y.; Tang, T.-T.; Girit, C.; Hao, Z.; Martin, M. C.; Zettl, A.; Crommie, M. F.; Shen, Y. R.; Wang, F. Direct Observation of a Widely Tunable Bandgap in Bilayer Graphene. *Nature* **2009**, *459*, 820–823.

(5) Lui, C. H.; Li, Z.; Mak, K. F.; Cappelluti, E.; Heinz, T. F. Observation of an Electrically Tunable Band Gap in Trilayer Graphene. *Nat. Phys.* **2011**, *7*, 944–947.

(6) Han, M. Y.; Özyilmaz, B.; Zhang, Y.; Kim, P. Energy Band-Gap Engineering of Graphene Nanoribbons. *Phys. Rev. Lett.* **2007**, *98*, 206805.

(7) Ni, Z. H.; Yu, T.; Lu, Y. H.; Wang, Y. Y.; Feng, Y. P.; Shen, Z. X. Uniaxial Strain on Graphene: Raman Spectroscopy Study and Band-Gap Opening. *ACS Nano* **2008**, *2*, 2301–2305.

(8) Zhou, S. Y.; Gweon, G.-H.; Fedorov, A. V.; First, P. N.; de Heer, W. A.; Lee, D.-H.; Guinea, F.; Castro Neto, A. H.; Lanzara, A. Substrate-Induced Bandgap Opening in Epitaxial Graphene. *Nat. Mater.* **2007**, *6*, 770–775.

(9) Jariwala, D.; Srivastava, A.; Ajayan, P. M. Graphene Synthesis and Band Gap Opening. *J. Nanosci. Nanotechnol.* **2011**, *11*, 6621–6641.

(10) Elias, D. C.; Nair, R. R.; Mohiuddin, T. M. G.; Morozov, S. V.; Blake, P.; Halsall, M. P.; Ferrari, A. C.; Boukhvalov, D. W.; Katsnelson, M. I.; Geim, A. K.; Novoselov, K. S. Control of Graphene's Properties by Reversible Hydrogenation: Evidence for Graphane. *Science* **2009**, *323*, 610–613.

(11) Niyogi, S.; Bekyarova, E.; Itkis, M. E.; Zhang, H.; Shepperd, K.; Hicks, J.; Sprinkle, M.; Berger, C.; Lau, C. N.; deHeer, W. A.; Conrad, E. H.; Haddon, R. C. Spectroscopy of Covalently Functionalized Graphene. *Nano Lett.* **2010**, *10*, 4061–4066.

(12) Son, J.; Lee, S.; Kim, S. J.; Park, B. C.; Lee, H.-K.; Kim, S.; Kim, J. H.; Hong, B. H.; Hong, J. Hydrogenated Monolayer Graphene with Reversible and Tunable Wide Band Gap and Its Field-Effect Transistor. *Nat. Commun.* **2016**, *7*, 13261.

(13) Giovannetti, G.; Khomyakov, P. A.; Brocks, G.; Kelly, P. J.; van den Brink, J. Substrate-Induced Band Gap in Graphene on Hexagonal Boron Nitride: *Ab Initio* Density Functional Calculations. *Phys. Rev. B* **2007**, *76*, 073103.

(14) Chen, Z.-G.; Shi, Z.; Yang, W.; Lu, X.; Lai, Y.; Yan, H.; Wang, F.; Zhang, G.; Li, Z. Observation of an Intrinsic Bandgap and Landau Level Renormalization in Graphene/Boron-Nitride Heterostructures. *Nat. Commun.* **2014**, *5*, 4461.

(15) Radisavljevic, B.; Radenovic, A.; Brivio, J.; Giacometti, V.; Kis, A. Single-Layer MoS_2 Transistors. *Nat. Nanotechnol.* **2011**, *6*, 147–150.

(16) Gong, C.; Zhang, H.; Wang, W.; Colombo, L.; Wallace, R. M.; Cho, K. Band Alignment of Two-Dimensional Transition Metal Dichalcogenides: Application in Tunnel Field Effect Transistors. *Appl. Phys. Lett.* **2013**, *103*, 053513.

(17) Ataca, C.; Şahin, H.; Ciraci, S. Stable, Single-Layer MX_2 Transition-Metal Oxides and Dichalcogenides in a Honeycomb-Like Structure. *J. Phys. Chem. C* **2012**, *116*, 8983–8999.

(18) Aji, A. S.; Solís-Fernández, P.; Ji, H. G.; Fukuda, K.; Ago, H. High Mobility WS_2

Transistors Realized by Multilayer Graphene Electrodes and Application to High Responsivity Flexible Photodetectors. *Adv. Funct. Mater.* **2017**, *27*, 1703448.

(19) Ji, H. G.; Solís-Fernández, P.; Yoshimura, D.; Maruyama, M.; Endo, T.; Miyata, Y.; Okada, S.; Ago, H. Chemically Tuned P- and n-Type WSe_2 Monolayers with High Carrier Mobility for Advanced Electronics. *Adv. Mater.* **2019**, *31*, 1903613.

(20) Groenendijk, D. J.; Buscema, M.; Steele, G. A.; Michaelis de Vasconcellos, S.; Bratschitsch, R.; van der Zant, H. S. J.; Castellanos-Gomez, A. Photovoltaic and Photothermoelectric Effect in a Double-Gated WSe_2 Device. *Nano Lett.* **2014**, *14*, 5846–5852.

(21) Zhang, Y.; Yao, Y.; Sendeku, M. G.; Yin, L.; Zhan, X.; Wang, F.; Wang, Z.; He, J. Recent Progress in CVD Growth of 2D Transition Metal Dichalcogenides and Related Heterostructures. *Adv. Mater.* **2019**, *31*, 1901694.

(22) McCreary, K. M.; Hanbicki, A. T.; Jernigan, G. G.; Culbertson, J. C.; Jonker, B. T. Synthesis of Large-Area WS_2 Monolayers with Exceptional Photoluminescence. *Sci. Rep.* **2016**, *6*, 19159.

(23) Dumcenco, D.; Ovchinnikov, D.; Marinov, K.; Lazić, P.; Gibertini, M.; Marzari, N.; Sanchez, O. L.; Kung, Y.-C.; Krasnozhon, D.; Chen, M.-W.; Bertolazzi, S.; Gillet, P.; Fontcuberta i Morral, A.; Radenovic, A.; Kis, A. Large-Area Epitaxial Monolayer MoS_2. *ACS Nano* **2015**, *9*, 4611–4620.

(24) Suenaga, K.; Ji, H. G.; Lin, Y.-C.; Vincent, T.; Maruyama, M.; Aji, A. S.; Shiratsuchi, Y.; Ding, D.; Kawahara, K.; Okada, S.; Panchal, V.; Kazakova, O.; Hibino, H.; Suenaga, K.; Ago, H. Surface-Mediated Aligned Growth of Monolayer MoS_2 and In-Plane Heterostructures with Graphene on Sapphire. *ACS Nano* **2018**, *12*, 10032–10044.

(25) Gao, Y.; Liu, Z.; Sun, D.-M.; Huang, L.; Ma, L.-P.; Yin, L.-C.; Ma, T.; Zhang, Z.; Ma, X.-L.; Peng, L.-M.; Cheng, H.-M.; Ren, W. Large-Area Synthesis of High-Quality and

Uniform Monolayer WS_2 on Reusable Au Foils. *Nat. Commun.* **2015**, *6*, 8569.

(26) Yun, S. J.; Chae, S. H.; Kim, H.; Park, J. C.; Park, J.-H.; Han, G. H.; Lee, J. S.; Kim, S. M.; Oh, H. M.; Seok, J.; Jeong, M. S.; Kim, K. K.; Lee, Y. H. Synthesis of Centimeter-Scale Monolayer Tungsten Disulfide Film on Gold Foils. *ACS Nano* **2015**, *9*, 5510–5519.

(27) Chen, W.; Zhao, J.; Zhang, J.; Gu, L.; Yang, Z.; Li, X.; Yu, H.; Zhu, X.; Yang, R.; Shi, D.; Lin, X.; Guo, J.; Bai, X.; Zhang, G. Oxygen-Assisted Chemical Vapor Deposition Growth of Large Single-Crystal and High-Quality Monolayer MoS_2. *J. Am. Chem. Soc.* **2015**, *137*, 15632–15635.

(28) Gong, Y.; Ye, G.; Lei, S.; Shi, G.; He, Y.; Lin, J.; Zhang, X.; Vajtai, R.; Pantelides, S. T.; Zhou, W.; Li, B.; Ajayan, P. M. Synthesis of Millimeter-Scale Transition Metal Dichalcogenides Single Crystals. *Adv. Funct. Mater.* **2016**, *26*, 2009–2015.

(29) Lan, F.; Yang, R.; Hao, S.; Zhou, B.; Sun, K.; Cheng, H.; Zhang, S.; Li, L.; Jin, L. Controllable Synthesis of Millimeter-Size Single Crystal WS_2. *Appl. Surf. Sci.* **2020**, *504*, 144378.

(30) Wachter, S.; Polyushkin, D. K.; Bethge, O.; Mueller, T. A Microprocessor Based on a Two-Dimensional Semiconductor. *Nat. Commun.* **2017**, *8*, 14948.

(31) Smithe, K. K. H.; Suryavanshi, S. V.; Muñoz Rojo, M.; Tedjarati, A. D.; Pop, E. Low Variability in Synthetic Monolayer MoS_2 Devices. *ACS Nano* **2017**, *11*, 8456–8463.

(32) Pu, J.; Funahashi, K.; Chen, C.-H.; Li, M.-Y.; Li, L.-J.; Takenobu, T. Highly Flexible and High-Performance Complementary Inverters of Large-Area Transition Metal Dichalcogenide Monolayers. *Adv. Mater.* **2016**, *28*, 4111–4119.

(33) Chiu, M.; Tang, H.; Tseng, C.; Han, Y.; Aljarb, A.; Huang, J.; Wan, Y.; Fu, J.; Zhang, X.; Chang, W.; Muller, D. A.; Takenobu, T.; Tung, V.; Li, L. Metal-Guided Selective Growth of 2D Materials: Demonstration of a Bottom-Up CMOS Inverter. *Adv. Mater.* **2019**, *31*, 1900861.

(34) Li, M.-Y.; Su, S.-K.; Wong, H.-S. P.; Li, L.-J. How 2D Semiconductors Could Extend Moore's Law. *Nature* **2019**, *567*, 169–170.

(35) Lee, C.-H.; Lee, G.-H.; van der Zande, A. M.; Chen, W.; Li, Y.; Han, M.; Cui, X.; Arefe, G.; Nuckolls, C.; Heinz, T. F.; Guo, J.; Hone, J.; Kim, P. Atomically Thin p–n Junctions with van Der Waals Heterointerfaces. *Nat. Nanotechnol.* **2014**, *9*, 676–681.

(36) Aji, A. S.; Izumoto, M.; Suenaga, K.; Yamamoto, K.; Nakashima, H.; Ago, H. Two-Step Synthesis and Characterization of Vertically Stacked SnS–WS_2 and SnS–MoS_2 p–n Heterojunctions. *Phys. Chem. Chem. Phys.* **2018**, *20*, 889–897.

(37) Yang, T.; Zheng, B.; Wang, Z.; Xu, T.; Pan, C.; Zou, J.; Zhang, X.; Qi, Z.; Liu, H.; Feng, Y.; Hu, W.; Miao, F.; Sun, L.; Duan, X.; Pan, A. Van Der Waals Epitaxial Growth and Optoelectronics of Large-Scale WSe_2/SnS_2 Vertical Bilayer p–n Junctions. *Nat. Commun.* **2017**, *8*, 1906.

(38) Wang, K.; Huang, B.; Tian, M.; Ceballos, F.; Lin, M.-W.; Mahjouri-Samani, M.; Boulesbaa, A.; Puretzky, A. A.; Rouleau, C. M.; Yoon, M.; Zhao, H.; Xiao, K.; Duscher, G.; Geohegan, D. B. Interlayer Coupling in Twisted WSe_2/WS_2 Bilayer Heterostructures Revealed by Optical Spectroscopy. *ACS Nano* **2016**, *10*, 6612–6622.

(39) Zhang, J.; Wang, J.; Chen, P.; Sun, Y.; Wu, S.; Jia, Z.; Lu, X.; Yu, H.; Chen, W.; Zhu, J.; Xie, G.; Yang, R.; Shi, D.; Xu, X.; Xiang, J.; Liu, K.; Zhang, G. Observation of Strong Interlayer Coupling in MoS_2/WS_2 Heterostructures. *Adv. Mater.* **2016**, *28*, 1950–1956.

(40) Huang, S.; Ling, X.; Liang, L.; Kong, J.; Terrones, H.; Meunier, V.; Dresselhaus, M. S. Probing the Interlayer Coupling of Twisted Bilayer MoS_2 Using Photoluminescence Spectroscopy. *Nano Lett.* **2014**, *14*, 5500–5508.

(41) Pak, S.; Lee, J.; Lee, Y.-W.; Jang, A.-R.; Ahn, S.; Ma, K. Y.; Cho, Y.; Hong, J.; Lee, S.; Jeong, H. Y.; Im, H.; Shin, H. S.; Morris, S. M.; Cha, S.; Sohn, J. I.; Kim, J. M. Strain-Mediated Interlayer Coupling Effects on the Excitonic Behaviors in an Epitaxially

Grown MoS_2/WS_2 van Der Waals Heterobilayer. *Nano Lett.* **2017**, *17*, 5634–5640.

(42) Du, L.; Yu, H.; Liao, M.; Wang, S.; Xie, L.; Lu, X.; Zhu, J.; Li, N.; Shen, C.; Chen, P.; Yang, R.; Shi, D.; Zhang, G. Modulating PL and Electronic Structures of MoS_2/Graphene Heterostructures via Interlayer Twisting Angle. *Appl. Phys. Lett.* **2017**, *111*, 263106.

(43) Chen, G.; Sharpe, A. L.; Gallagher, P.; Rosen, I. T.; Fox, E. J.; Jiang, L.; Lyu, B.; Li, H.; Watanabe, K.; Taniguchi, T.; Jung, J.; Shi, Z.; Goldhaber-Gordon, D.; Zhang, Y.; Wang, F. Signatures of Tunable Superconductivity in a Trilayer Graphene Moiré Superlattice. *Nature* **2019**, *572*, 215–219.

(44) Moriyama, S.; Morita, Y.; Komatsu, K.; Endo, K.; Iwasaki, T.; Nakaharai, S.; Noguchi, Y.; Wakayama, Y.; Tsuya, D.; Watanabe, K.; Taniguchi, T. Observation of Superconductivity in Bilayer Graphene/Hexagonal Boron Nitride Superlattices. https://doi.org/arXiv:1901.09356 [cond-mat.supr-con].

(45) Moon, P.; Koshino, M. Electronic Properties of Graphene/Hexagonal-Boron-Nitride Moiré Superlattice. *Phys. Rev. B* **2014**, *90*, 155406.

(46) Cao, Y.; Fatemi, V.; Fang, S.; Watanabe, K.; Taniguchi, T.; Kaxiras, E.; Jarillo-Herrero, P. Unconventional Superconductivity in Magic-Angle Graphene Superlattices. *Nature* **2018**, *556*, 43–50.

(47) Gong, Y.; Lin, J.; Wang, X.; Shi, G.; Lei, S.; Lin, Z.; Zou, X.; Ye, G.; Vajtai, R.; Yakobson, B. I.; Terrones, H.; Terrones, M.; Tay, B. K.; Lou, J.; Pantelides, S. T.; Liu, Z.; Zhou, W.; Ajayan, P. M. Vertical and In-Plane Heterostructures from WS_2/MoS_2 Monolayers. *Nat. Mater.* **2014**, *13*, 1135–1142.

(48) Kobayashi, Y.; Yoshida, S.; Maruyama, M.; Mogi, H.; Murase, K.; Maniwa, Y.; Takeuchi, O.; Okada, S.; Shigekawa, H.; Miyata, Y. Continuous Heteroepitaxy of Two-Dimensional Heterostructures Based on Layered Chalcogenides. *ACS Nano* **2019**, *13*,

7527–7535.

(49) Novoselov, K. S.; Mishchenko, A.; Carvalho, A.; Neto, A. H. C. 2D Materials and van Der Waals Heterostructures. *Science* **2016**, *353*, aac9439.

(50) Hong, J.; Hu, Z.; Probert, M.; Li, K.; Lv, D.; Yang, X.; Gu, L.; Mao, N.; Feng, Q.; Xie, L.; Zhang, J.; Wu, D.; Zhang, Z.; Jin, C.; Ji, W.; Zhang, X.; Yuan, J.; Zhang, Z. Exploring Atomic Defects in Molybdenum Disulphide Monolayers. *Nat. Commun.* **2015**, *6*, 6293.

(51) Zhou, W.; Zou, X.; Najmaei, S.; Liu, Z.; Shi, Y.; Kong, J.; Lou, J.; Ajayan, P. M.; Yakobson, B. I.; Idrobo, J.-C. Intrinsic Structural Defects in Monolayer Molybdenum Disulfide. *Nano Lett.* **2013**, *13*, 2615–2622.

(52) Lin Yung-Chang; Li Shisheng; Komsa Hannu-Pekka; Chang Li-Jen; Krasheninnikov Arkady V.; Eda Goki; Suenaga Kazu. Revealing the Atomic Defects of WS_2 Governing Its Distinct Optical Emissions. *Adv. Funct. Mater.* **2017**, *28*, 1704210.

(53) Kang, K.; Xie, S.; Huang, L.; Han, Y.; Huang, P. Y.; Mak, K. F.; Kim, C.-J.; Muller, D.; Park, J. High-Mobility Three-Atom-Thick Semiconducting Films with Wafer-Scale Homogeneity. *Nature* **2015**, *520*, 656–660.

(54) Yu, H.; Liao, M.; Zhao, W.; Liu, G.; Zhou, X. J.; Wei, Z.; Xu, X.; Liu, K.; Hu, Z.; Deng, K.; Zhou, S.; Shi, J.-A.; Gu, L.; Shen, C.; Zhang, T.; Du, L.; Xie, L.; Zhu, J.; Chen, W.; Yang, R.; Shi, D.; Zhang, G. Wafer-Scale Growth and Transfer of Highly-Oriented Monolayer MoS_2 Continuous Films. *ACS Nano* **2017**, *11*, 12001–12007.

(55) van der Zande, A. M.; Huang, P. Y.; Chenet, D. A.; Berkelbach, T. C.; You, Y.; Lee, G.-H.; Heinz, T. F.; Reichman, D. R.; Muller, D. A.; Hone, J. C. Grains and Grain Boundaries in Highly Crystalline Monolayer Molybdenum Disulphide. *Nat. Mater.* **2013**, *12*, 554–561.

(56) Ly, T. H.; Perello, D. J.; Zhao, J.; Deng, Q.; Kim, H.; Han, G. H.; Chae, S. H.; Jeong, H. Y.; Lee, Y. H. Misorientation-Angle-Dependent Electrical Transport across

Molybdenum Disulfide Grain Boundaries. *Nat. Commun.* **2016**, *7*, 10426.

(57) Kang, K. N.; Godin, K.; Yang, E.-H. The Growth Scale and Kinetics of WS_2 Monolayers under Varying H_2 Concentration. *Sci. Rep.* **2015**, *5*, 13205.

(58) Gao, Y.; Hong, Y.-L.; Yin, L.-C.; Wu, Z.; Yang, Z.; Chen, M.-L.; Liu, Z.; Ma, T.; Sun, D.-M.; Ni, Z.; Ma, X.-L.; Cheng, H.-M.; Ren, W. Ultrafast Growth of High-Quality Monolayer WSe_2 on Au. *Adv. Mater.* **2017**, *29*, 1700990.

(59) Godin, K.; Kang, K.; Fu, S.; Yang, E.-H. Increased Monolayer Domain Size and Patterned Growth of Tungsten Disulfide through Controlling Surface Energy of Substrates. *J. Phys.D : Appl. Phys.* **2016**, *49*, 325304.

(60) Rong, Y.; Fan, Y.; Leen Koh, A.; Robertson, A. W.; He, K.; Wang, S.; Tan, H.; Sinclair, R.; Warner, J. H. Controlling Sulphur Precursor Addition for Large Single Crystal Domains of WS_2. *Nanoscale* **2014**, *6*, 12096–12103.

(61) Dobrovinskaya, E. R.; Lytvynov, L. A.; Pishchik, V. Properties of Sapphire. In *Sapphire*; Micro- and Opto-Electronic Materials, Structures, and Systems; Springer US, 2009; pp 55–176.

(62) Zhang, S.; Hill, H. M.; Moudgil, K.; Richter, C. A.; Walker, A. R. H.; Barlow, S.; Marder, S. R.; Hacker, C. A.; Pookpanratana, S. J. Controllable, Wide-Ranging n-Doping and p-Doping of Monolayer Group 6 Transition-Metal Disulfides and Diselenides. *Adv. Mater.* **2018**, *30*, 1806345.

(63) Yang, L.; Majumdar, K.; Liu, H.; Du, Y.; Wu, H.; Hatzistergos, M.; Hung, P. Y.; Tieckelmann, R.; Tsai, W.; Hobbs, C.; Ye, P. D. Chloride Molecular Doping Technique on 2D Materials: WS_2 and MoS_2. *Nano Lett.* **2014**, *14*, 6275–6280.

(64) Tang, B.; Yu, Z. G.; Huang, L.; Chai, J.; Wong, S. L.; Deng, J.; Yang, W.; Gong, H.; Wang, S.; Ang, K.-W.; Zhang, Y.-W.; Chi, D. Direct N- to p-Type Channel Conversion in Monolayer/Few-Layer WS_2 Field-Effect Transistors by Atomic Nitrogen Treatment.

ACS Nano **2018**, *12*, 2506–2513.

(65) Suh, J.; Park, T.-E.; Lin, D.-Y.; Fu, D.; Park, J.; Jung, H. J.; Chen, Y.; Ko, C.; Jang, C.; Sun, Y.; Sinclair, R.; Chang, J.; Tongay, S.; Wu, J. Doping against the Native Propensity of MoS_2: Degenerate Hole Doping by Cation Substitution. *Nano Lett.* **2014**, *14*, 6976–6982.

(66) Qin, Z.; Loh, L.; Wang, J.; Xu, X.; Zhang, Q.; Haas, B.; Alvarez, C.; Okuno, H.; Yong, J. Z.; Schultz, T.; Koch, N.; Dan, J.; Pennycook, S. J.; Zeng, D.; Bosman, M.; Eda, G. Growth of Nb-Doped Monolayer WS_2 from Liquid-Phase Precursor Mixing. *ACS Nano* **2019**, *13*, 10768–10775.

(67) Chen, C.-H.; Wu, C.-L.; Pu, J.; Chiu, M.-H.; Kumar, P.; Takenobu, T.; Li, L.-J. Hole Mobility Enhancement and p-Doping in Monolayer WSe_2 by Gold Decoration. *2D Mater.* **2014**, *1*, 034001.

(68) Liu, X.; Qu, D.; Ryu, J.; Ahmed, F.; Yang, Z.; Lee, D.; Yoo, W. J. P-Type Polar Transition of Chemically Doped Multilayer MoS_2 Transistor. *Adv. Mater.* **2016**, *28*, 2345–2351.

(69) Jariwala, D.; Sangwan, V. K.; Lauhon, L. J.; Marks, T. J.; Hersam, M. C. Emerging Device Applications for Semiconducting Two-Dimensional Transition Metal Dichalcogenides. *ACS Nano* **2014**, *8*, 1102–1120.

Chapter 2

Property and Preparation of TMD Materials

2.1. Crystal structures and physical properties of TMDs

2.1.1. Crystal structures

Transition metal dichalcogenides, such as WS_2, MoS_2, and WSe_2, have atomically thin two-dimensional structures composed of single layer atomic sheet of transition metal (W, Mo) which is sandwiched by two layers of chalcogen atom (S, Se, Te) layers, having three fold symmetry (see Figure 1.1b). They exist as polytype phases with different crystal and electronic band structures. As shown in Figure 2.1, for example, the TMDs with the 2H phase have a semiconducting property, while those with the 1T phase have a metallic property.[1–3] In nature, semiconducting 2H phase is energetically more favorable, and artificial treatments, such as lithium intercalation shown in Figure 2.2, are necessary to obtain metallic property by conversion to 1T phase.[4–6] Thus, all TMDs dealt with in this thesis belong to 2H phase with semiconducting property.

Depending on atomic composition of each TMD, they have slightly different lattice constants. Lattice parameters a (= b), c (indicated in Figure 2.3) of WS_2 is 3.15, 12.32 Å, MoS_2 is 3.15, 12.3 Å, and WSe_2 is 3.28, 12.95 Å, respectively.[7,8] TMDs have strong in-plane ionic-covalent bonds among constituent atoms, while there is no chemical bond between adjacent layers. Between layers, there is weak van der Waals interaction which holds adjacent layers bound and

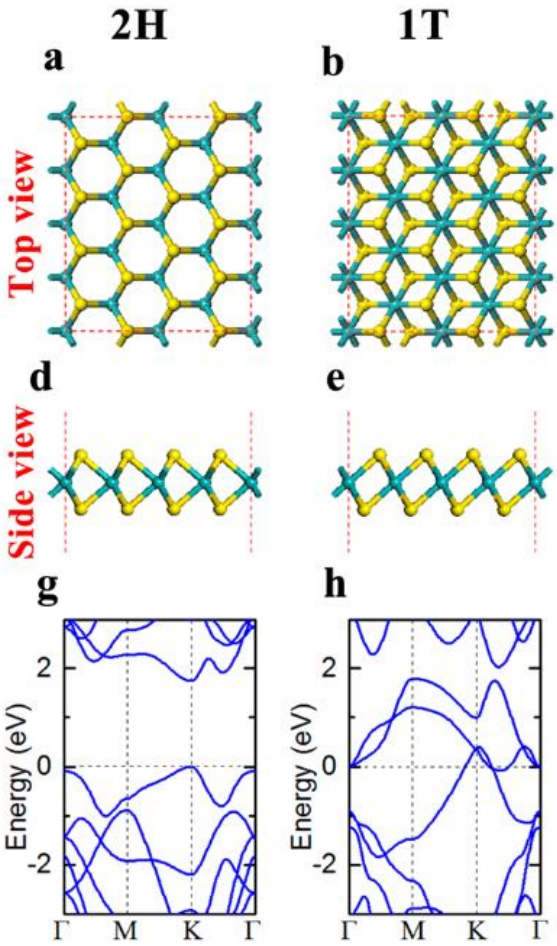

Figure 2.1. Top and side view of 2H and 1T MoS_2, and their band structures. Cyan and yellow atoms correspond to Mo and S, respectively. Reproduced from Ref. 3.

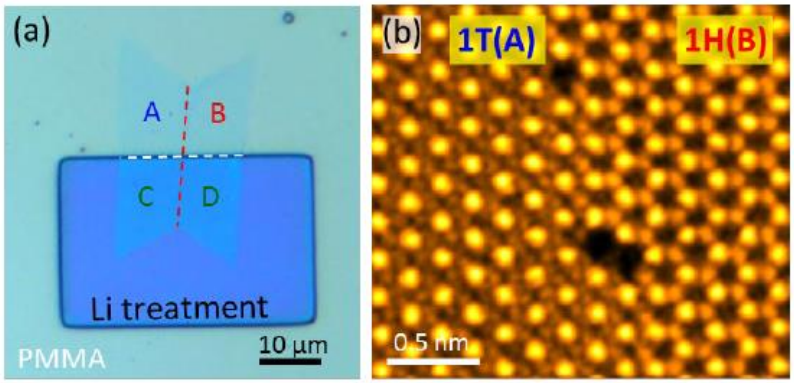

Figure 2.2. (a) An optical image of a monolayer WS_2 butterfly transferred on a 300 nm SiO_2/Si substrate. Red dash line indicates the boundary between the left and right wings. The surface was spin coated with PMMA (polymethyl methacrylate) and an e-beam lithographical window was opened in the lower half of the WS_2 butterfly. White dash line indicates the unmasked edge on the WS_2 butterfly. Four quadrants: A, B, C, and D are assigned to the parts of WS_2 butterfly. (b) An annular dark field STEM image of the WS_2 butterfly taken at the A/B domain boundary in (a), where the quadrant-A shows 1T phase, while the quadrant-B shows 1H phase. Reproduced from Ref. 6.

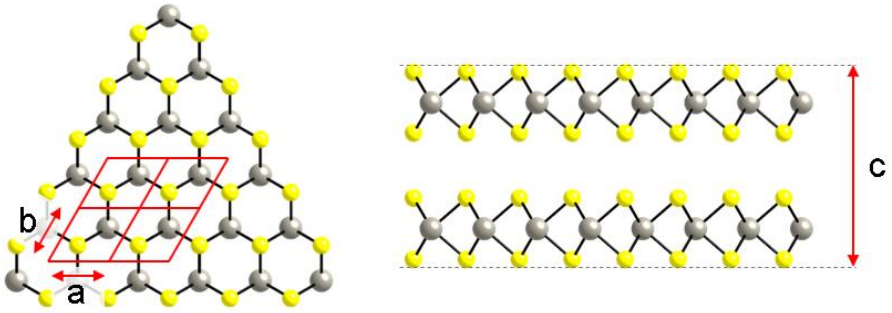

Figure 2.3. Lattice parameters *a*, *b*, and *c* of transition metal dichalcogenides. Grey and yellow spheres correspond to transition metal and chalcogen atoms, respectively.

makes a layered structure. Due to this unique 2D structure, TMDs show layer number-dependent changes in their physical properties, which is sometimes called as the layer number degree of freedom. More details are explained in the following chapters.

2.1.2. Physical properties

2.1.2.1. Phonon modes

TMDs have distinct Raman scattering not only depending on their atomic composition, but also on the number of layers. Having different atomic mass, interatomic interaction, and lattice parameters depending on atomic composition, each TMD has different phonon modes with distinctive vibrational energies (see Figure 2.4). In addition, it also changes depending on the number of layers. With unique atomically thin layered structure, phonons in monolayer TMD is strongly affected when additional layers are attached on it. Consequently, the layer number-dependent phonon scattering property becomes one of the strongest tools to distinguish the number of layers (thickness) of TMDs. Figure 2.5 shows layer number- and excitation energy-dependent Raman spectra and peak frequencies of WS_2.[9] For example, both WS_2 and MoS_2 have E^1_{2g} and A_{1g} phonon modes that correspond to in-plane and out-of-plane vibration,

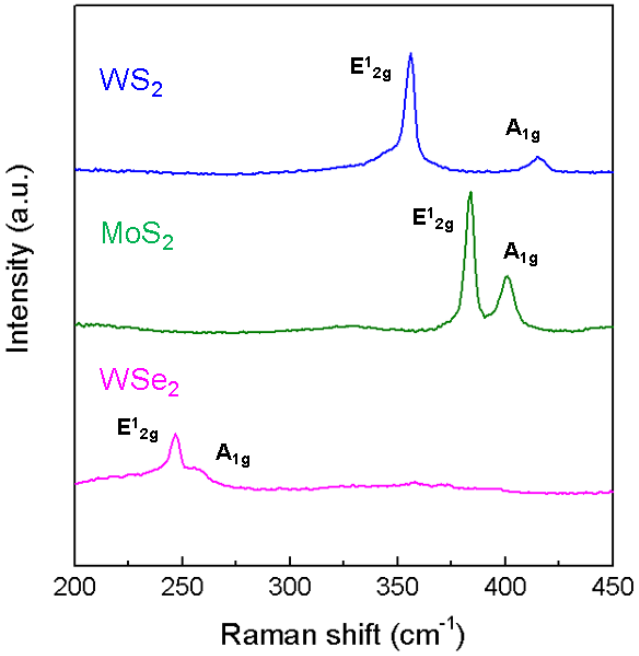

Figure 2.4. Raman spectra of monolayer WS_2, MoS_2, and WSe_2 measured using 473 nm excitation.

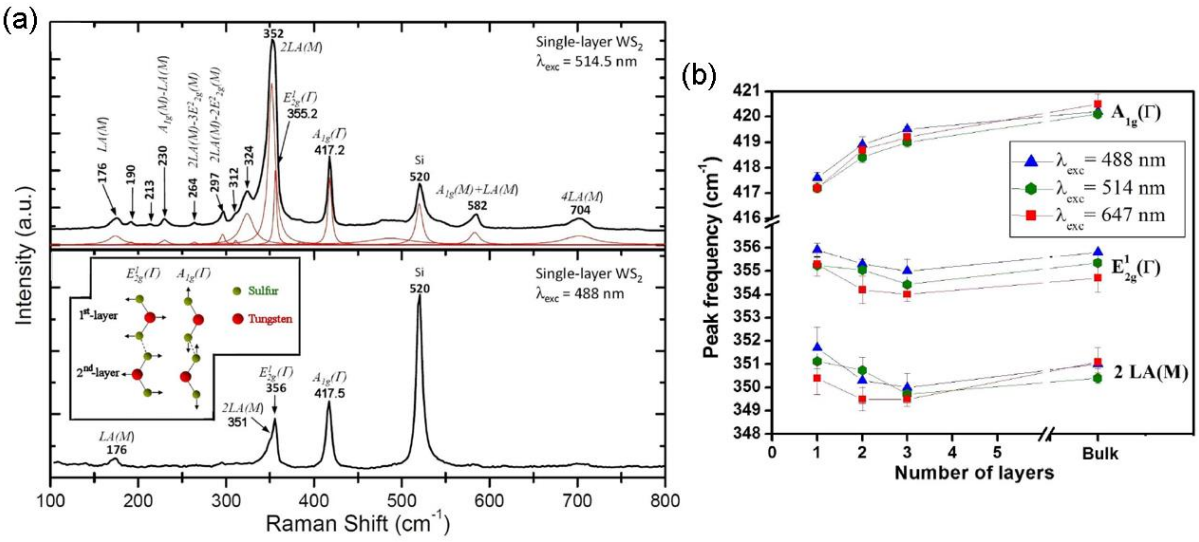

Figure 2.5. (a) Representative Raman spectra of monolayer WS_2 excited using 514.5 nm and 488 nm laser. (b) The layer number-dependent shift of A_{1g}, E^1_{2g}, and 2LA peaks of WS_2. Reproduced from Ref. 9.

respectively, and the separation between those mode of around ~60 and ~20 cm^{-1} are known to correspond to single layers.[10] Additionally, use of different excitation energy is known to cause appearance of additional vibrational modes.[9] Therefore, Raman spectroscopy using

suitable excitation energy becomes very quick and efficient way to identify the TMDs and distinguish the thickness of TMD materials.

2.1.2.2. Electronic band structure

As aforementioned, TMDs exist as polytype phases. The distinctive electronic band structures of 2H MoS_2 with sizable band gap at *K* valley and 1T MoS_2 without band gap are shown in Figure 2.1.[3] Also, the calculated layer number-dependent electronic band structures and thickness-dependent band gap change of representative TMDs are shown in Figure 2.6.[11] Monolayer TMDs have the largest band gap at *K* valley with direct transition from conduction to valence band. As they become thicker than monolayer, however, the band gap is gradually reduced and the transition changes to be indirect followed by the change of the global band extrema depending on the number of layer.[12] Thus, the monolayer TMDs with a broad choice of band gap size and direct transition become a good base to study optics and optoelectronics of 2D materials.

2.1.2.3. Spin degree of freedom

Different from graphene which consists only of carbon, TMDs have diatomic structures composed of transition metal and chalcogen atoms, thus, the in-plane inversion symmetry is broken in monolayer TMDs (Figure 1.1). The outer layers of electronic state of TMDs consist of d-orbital of transition metal atoms so that this together with the broken inversion symmetry makes electrons in monolayer TMDs experience the asymmetrical potential gradient. Owing to the asymmetrical in-plane electric field together with the resultant out-of-plane Zeeman-like effective magnetic field, spin-orbit coupling-induced spin-orbit splitting occurs in conduction

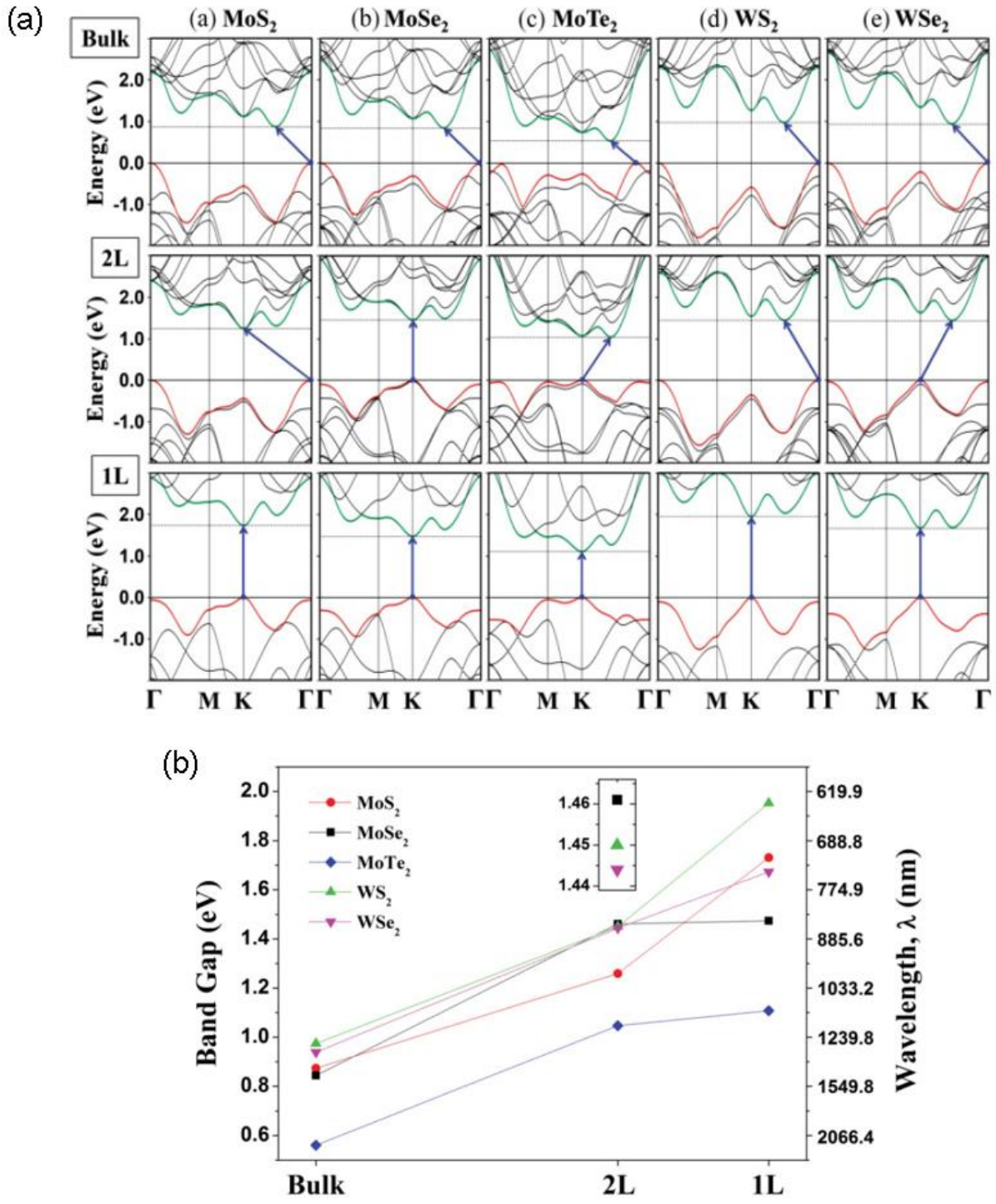

Figure 2.6. (a) Calculated electronic band structures of representative TMDs with different thicknesses. 1L and 2L mean mono- and bi-layer. (b) Thickness-dependent band gap change of representative TMDs. Reproduced from Ref. 11.

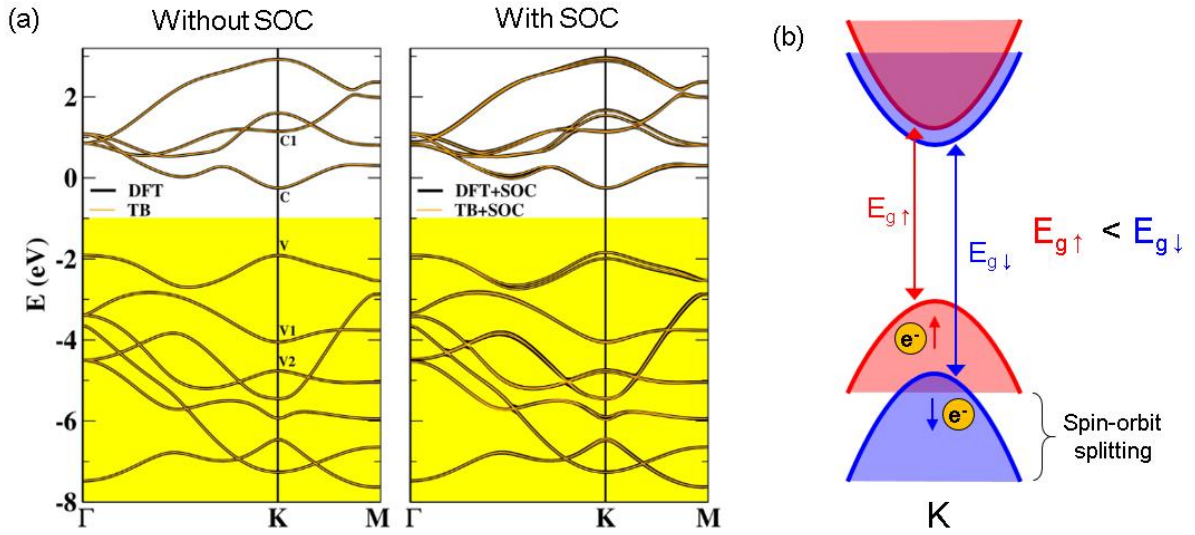

Figure 2.7. (a) Calculated electronic band structures of monolayer MoS_2 with and without spin orbit coupling (SOC). (b) Band diagram at *K* valley with spin-orbit splitting in conduction and valence bands. Electron with spin-up state has slightly smaller transition energy (E_g) compared with electron with spin-down state. Figure 2.7a is reproduced from Ref. 13.

and valence bands.[13–15] Figure 2.7a shows the calculated electronic band structure of monolayer MoS_2 with and without spin-orbit coupling and the band splitting at *K* point can be seen when spin-orbit coupling is induced.[14] The split energy states at *K* and *K*' valleys have sizable separation, especially in valence band (~ 400 meV in WS_2).[13] The electron residing in each split state has an opposite spin state, consequently, the spin of electrons can be controlled by choosing the excitation energy (see Figure 2.7b). This spin controllability of electrons (additional spin degree of freedom) in TMDs allows additional data storage in electrons.

2.1.2.4. Valley degree of freedom

Due to the diatomic composition and broken inversion symmetry in monolayer TMDs, spin-orbit splitting occurs in conduction and valence bands. Also, due to the broken inversion

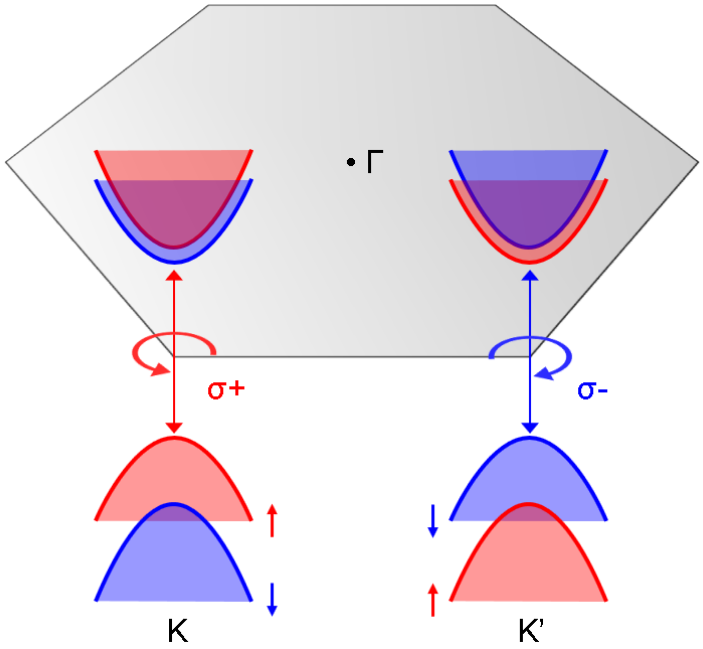

Figure 2.8. Electronic band dispersions of monolayer TMDs near *K* and *K*' valleys of Brillouin zone. The interband transition in each valley has opposite helicity and optical selection rule.

symmetry in monolayer TMDs, degenerate inequivalent *K* valleys (*K* and *K*') exist in 2D hexagonal Brillouin zone, as shown in Figure 2.8.[16] Electrons at respective *K* and *K*' valleys experience the same size but oppositely directed out-of-plane Zeeman-like efficient magnetic field. Therefore, electrons at *K* and *K*' valleys are oppositely spin polarized and have different optical selectivity, electrons at *K* (*K*') valley interacting with right- (left-) circular polarized light, respectively.[13,14,17] This valley-dependent spin polarization together with the opposite optical selectivity of electrons allow additional degree of freedom, which can be used for additional information storage in carriers.

2.1.2.5. Optical property

2.1.2.5.1. Direct and indirect transition

The band gap of TMDs shows interesting change in their transition mechanism from direct (monolayer) to indirect as get thicker (see Figure 2.6). Also, the size of band gap gradually decreases as the number of layers increases. When thicker than monolayer, the indirect transition of electrons from conduction to valence band accompanies phonon-assisted momentum change which dissipates electrons' energy as heat. As a result, the optical efficiency is highest in monolayer (*K*-*K* direct transition) and exponentially deteriorates with increasing the thickness. Regarding the PL efficiency of TMDs, up to 60 % of PL quantum yield was reported for CVD-grown WS_2.[18] The broad range of band gap energy (0.95 ~ 2.02 eV) of various TMD materials offers flexible choice of active material in optoelectronic engineering depending on the purpose, and it makes TMDs promising materials for optoelectronics.[19]

2.1.2.5.2. Spin-valley polarization

As described in previous sections, monolayers of TMDs possess inequivalent degenerate *K* and *K*' valleys in momentum space with global extrema located on it. Having oppositely spin-polarized electrons, each *K* valley has different optical selectivity. Therefore, by using right- or left-circular polarized excitation laser, it is possible to selectively shine the desired valley and obtain the spin-valley polarized excitons.[20–25] Originating in the large exciton binding energy (~ hundreds of meV) and long exciton lifetime by large spin-orbit splitting, high efficiency of spin-valley polarization has been reported even at room temperature.[26]

2.1.2.5.3. Interlayer exciton

Strong quantum confinement effect in monolayer TMDs results in various interesting optical properties. Stacking two layers of TMDs offers a new opportunity to obtain exotic physical properties. Once two different TMD monolayers are stacked with type II band alignment as shown in Figure 2.9, excitons can be formed between the layers which is called interlayer exciton.[27,27–29] Formation of interlayer exciton relies not only on the band alignment, but also on the lattice mismatch and electronic band structures.[30] Once interlayer excitons are formed, their energy is determined by the electronic band structures of substituent monolayers. Therefore, by choosing suitable combinations of substituent monolayers, the energy of interlayer excitons can be engineered.[31]

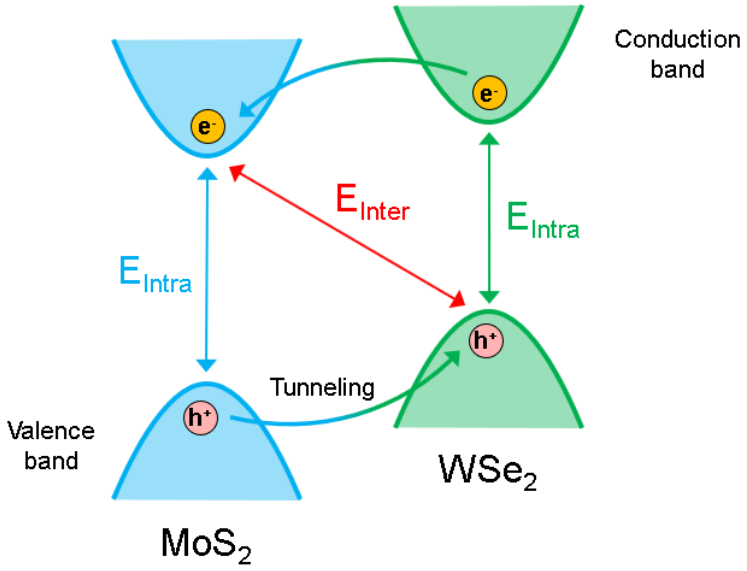

Figure 2.9. Type II band alignment between MoS_2 and WSe_2. Blue and green arrows represent intralayer transitions within MoS_2 and WSe_2, respectively. Red arrow indicates interlayer transition which accompanies tunneling of carriers between layers.

2.1.2.5.4. Exciton control

Due to the large exciton binding energy and spin-valley degree of freedoms in electron, TMD materials become an interesting platform to study the spin-valley optics. In TMD heterostructures, interlayer excitons can be formed by spatially separated electron and hole pair staying at respective layers. Different from the intralayer excitons, the interlayer excitons have vertical dipole moment which causes Stark effect. Therefore, by inducing vertical electric field to the heterostructure with interlayer excitons, it is possible to further control the energy of interlayer excitons.[32,33] Figure 2.10 represents the energy change of interlayer exciton in $MoSe_2$-WSe_2 heterostructure depending on the applied vertical electric field. In addition, spatial separation of electron and hole pair of interlayer exciton results in much longer

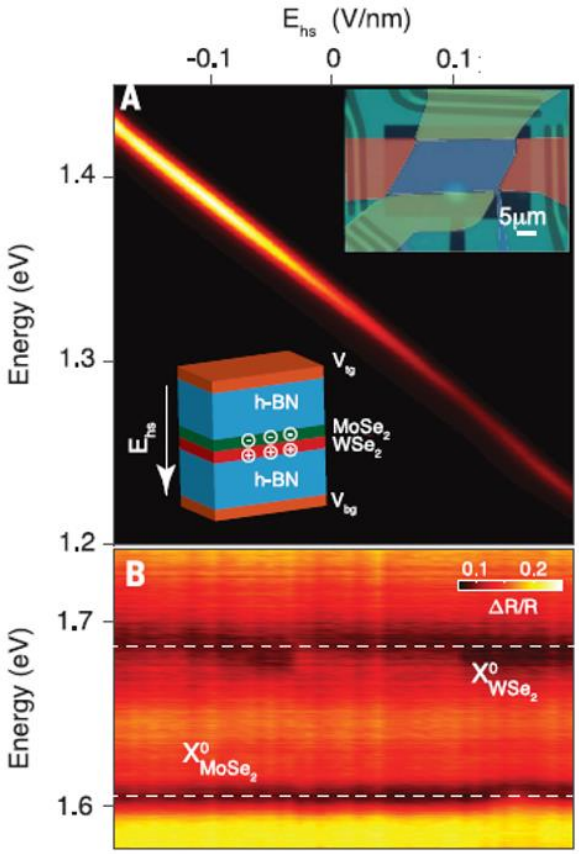

Figure 2.10. The energy of interlayer (up) and intralayer (down) excitons versus electric field applied to $MoSe_2$-WSe_2 heterostructure. The top inset is an optical image of a representative device. The bottom inset is schematic of the heterostructure cross section. The white arrow represents positive direction of electric field. Reproduced from Ref. 33.

exciton lifetime compared with intralayer one. This long lifetime allows microscale lateral diffusion of excitons even at room temperature, in which the diffusion direction can be further controlled by electrical manipulation.[33,34] Moreover, the flow of valley-polarized excitons excited by circularly polarized laser could be controlled by inducing electrical potential.[35] The operation of exciton transistor devices made of bulk semiconductors-based coupled quantum wells were already reported.[36,37] However, they require low temperature operation, which is not suitable for practical applications. In contrast, long lifetime of interlayer excitons in TMD heterostructures makes it feasible to realize room-temperature operating TMD-based exciton transistors. Therefore, TMDs are promising optoelectronic materials although more studies and investigations are necessary.

2.1.2.6. Electrical transport

2.1.2.6.1. Field-effect transistor

Having sizable band gaps, TMDs can be used for switching transistors. Since the first demonstration of single layer MoS_2 transistor that showed impressive performance (carrier mobility (μ) ~ 217 $cm^2V^{-1}s^{-1}$),[38] the electrical transport of TMD materials has been actively investigated. For evaluating the electrical transport properties, usually bottom- or top-gated FETs are fabricated followed by 2- or 4-probe measurement. Figure 2.11 depicts three typical device structures used for TMD FETs. The carrier mobility is extracted using the following equation.

$$\mu = \frac{g_{\mathrm{m}}}{\mathrm{C_{ox}} V_{\mathrm{d}}} \frac{L}{W} \tag{2.1}$$

where $g_m = dI_d/dV_g$ is the transconductance obtained from the transfer curve; C_{ox} is the capacitance per unit area of insulator; V_d is the applied drain voltage; L and W represent the

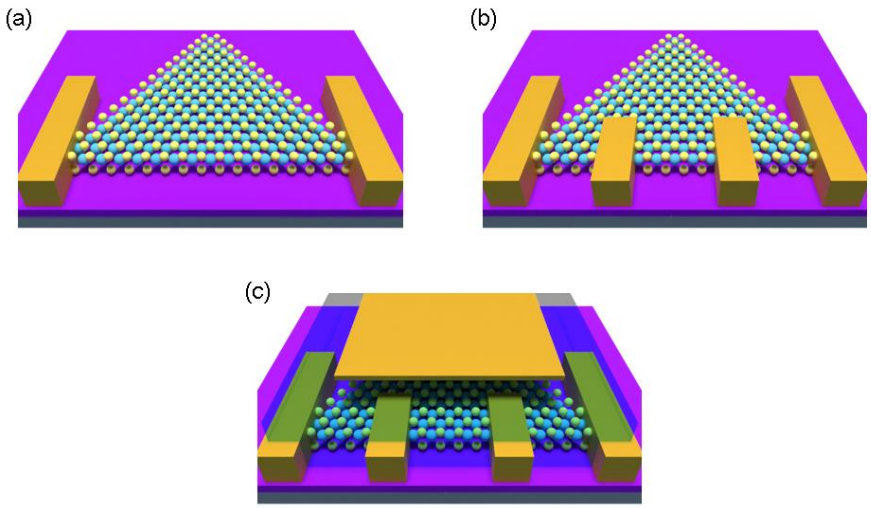

Figure 2.11. Schematics of (a,b) bottom-gated FETs on SiO_2/Si substrate with 2 and 4 electrodes. (c) Top-gated structure with additional insulating layer and top electrode deposited on the channel.

effective length and width of the channel.

Generally, mechanically exfoliated flakes show better transport and switching performance compared with CVD-grown samples. This is because the native crystal defects exist in CVD-grown materials, which consist of sulfur defect, broken structure, undesired extrinsic substitutional doping, or grain boundary, trap and scatter the carriers hindering their flow.[39–46] Many theoretical calculations expected promising electrical transport properties for WS_2, MoS_2, and WSe_2.[47,48] However, still the experimental demonstration, especially when using CVD-grown materials, cannot keep up with the theoretical values and there are several reasons need to be noted. First, as already mentioned, the crystal quality needs to be high enough to suppress the defect-induced phonon scattering. Second, for efficient carrier injection from electrode to channel, the electrode contact needs to form a good Ohmic contact without Schottky barrier.[49,50] Third, due to the atomically thin structure of 2D materials, they are vulnerable to surrounding dielectric environment. Any undesired charge impurities around the channel can strongly affect the device performance. Therefore, removing the charge

impurities in the oxide (insulating) layer of transistor device or protecting TMD channels with highly dielectric, covalent bonding-free h-BN will help extract the intrinsic properties of TMDs.[51–53]

Depending on atomic composition, each monolayer TMD has different electrical transport polarity. For example, MoS_2 and WS_2 typically show n-type transport, while WSe_2 and $MoSe_2$ show ambipolar transport behavior although the polarity of majority carriers changes depending on measurement environment. Figure 2.12 indicates the transfer characteristics of various exfoliated TMDs and their polarity change by chemical doping.[54] The transport polarity is important when fabricating electronic devices, such as p-n junction and logic circuits. For these applications, both of n- and p-type channels are necessary. However, there is almost no p-type TMDs and few of them are toxic or air-unstable. As a result, several methods have

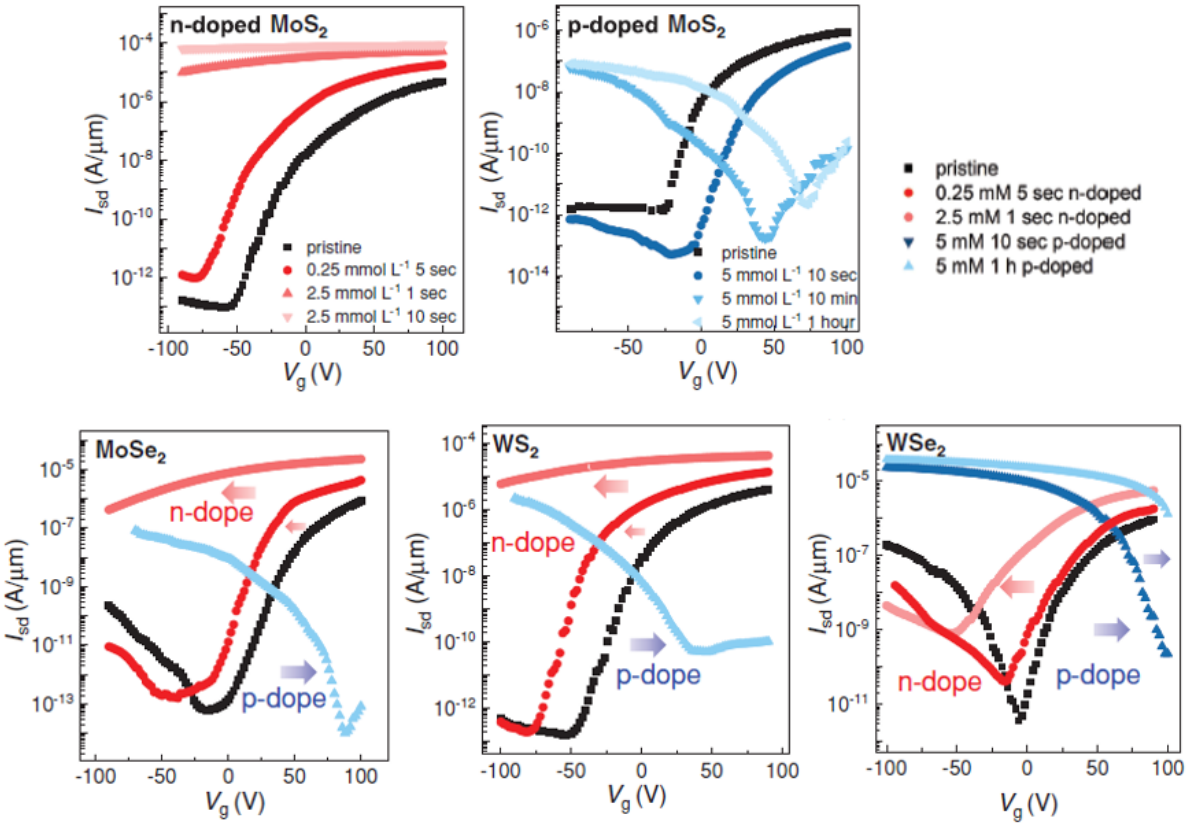

Figure 2.12. Representative transfer characteristics of a pristine MoS_2, WS_2, $MoSe_2$, and WSe_2 FETs before and after doping using n-type dopant ($C_{30}H_{40}Rh_2$ (RhCp*Cp)$_2$) or p-type dopant ([N(C_6H_4-*p*-Br)$_3$]$SbCl_6$) of various concentration and exposure time. Reproduced from Ref. 54.

been reported to control the electrical transport polarity of TMD sheets, such as substitutional doping, [55–57] chemical doping (see Figure 2.12)[54,58] and tuning the Schottky barrier by changing the electrode metals.[59,60]

2.1.2.6.2. Logic circuits

Based on good transport and switching performance, logic circuits become one of the most promising applications of TMD materials. The importance of fabricating high-performance logic gates, such as CMOS, NOT, OR, AND is needless to be emphasized. As shown in Figure 2.13, various logic gates have been fabricated using exfoliated MoS_2, WSe_2, and $MoTe_2$, which showed good performance.[61–65] Also, CVD-grown WSe_2 and MoS_2 were used to fabricate a flexible CMOS inverter on a polyimide film as shown in Figure 2.14a, which showed high voltage gain of ~30 (Figure 2.14b).[66] When fabricating logic circuits, use of pure p-type channel together with typical n-channel is beneficial for improving the device performance, as compared with when ambipolar channel is used as p-channel or both channels are n-type.[66] Therefore, asymmetric chemical doping was introduced to achieve CMOS operation by forming p- and n-doped MoS_2 channels. In similar tactics, chemical doping of WSe_2[67,68] and defect-engineered p-doping of MoS_2 were reported.[69] Thus, TMD materials have bright promise not only in applications of typical logic gates but also in flexible and transparent electronics.

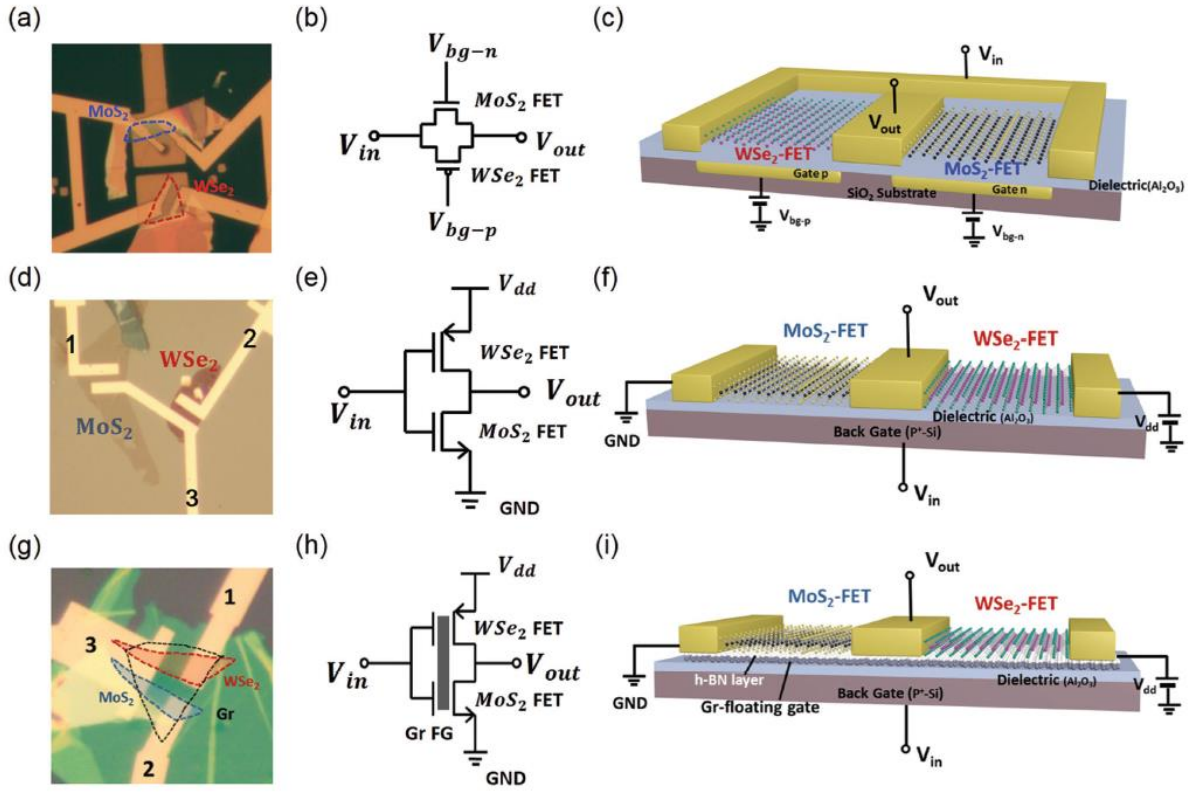

Figure 2.13. Three kinds of fundamental logic units based on different configuration of MoS_2 and WSe_2. Optical images, logic circuit diagrams, and schematic diagrams of (a, b, and c) complementary logic transmission gate, (d, e, and f) inverter, and (g, h, and i) Schmidt-like flip-flop. Reproduced from Ref. 62.

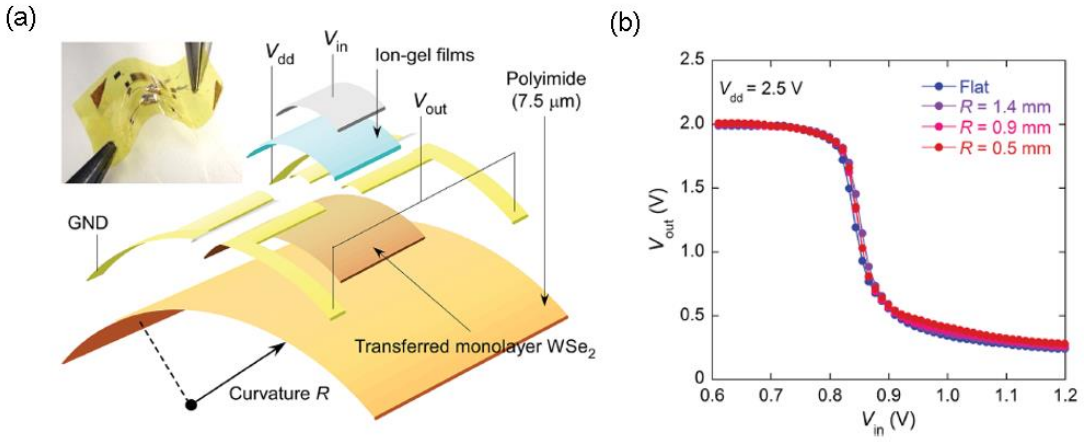

Figure 2.14. (a) Schematic illustration and optical image of high-gain quasi-CMOS inverter made of WSe_2 monolayer film on a flexible polyimide substrate. (b) V_{in}-V_{out} transfer characteristics of WSe_2 inverter at different values of curvature radius R. Reproduced from Ref. 66.

2.1.2.6.3. Valley Hall effect

As mentioned in the previous section, one of the greatest interesting physical properties of monolayer TMDs is the additional spin-valley degree of freedoms of electrons. The existence of spin and valley degree of freedoms together with electric charge in electrons results in valley Hall effect (VHE).[70] When circularly polarized laser is illuminated on the monolayer TMD which has a broken inversion symmetry, valley-dependent (*K* and *K*') oppositely spin-polarized electrons are excited. Once the channel is biased, electrons at each *K* valley experience oppositely directed Lorentz-like force, thus, move to the opposite directions perpendicular to the drift current in the channel.[70] Figure 2.15 illustrates the circularly polarized laser-induced valley Hall effect. In 2014, observation of the VHE from monolayer MoS_2 was reported.[71] In case of bilayer MoS_2, however, VHE was not observed reflecting the preserved inversion symmetry. More recently, VHE of interlayer exciton was observed from MoS_2-WSe_2 heterostructure, even at room temperature.[72] The VHE in TMD materials implies their promise to be used in valleytronic applications for information storage and processing.

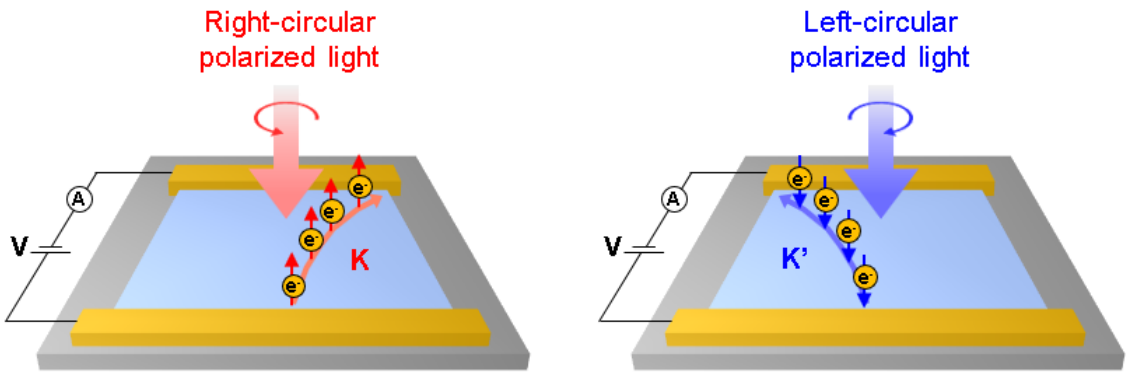

Figure 2.15. Illustration of circularly polarized excitation-induced valley Hall effect. Oppositely circular polarized lasers induce selective excitation in *K* or *K*' valley. By opposite spin polarization of electrons in each valley, opposite Hall voltage is induced and electrons move to opposite direction on the channel perpendicular to the drift current.

2.1.2.7. Twistronics

Since the observation of magic angle-induced superconductivity in bilayer graphene,[73] a new field of research (called Twistronics) has emerged, which investigates the stacking of layered materials with controlled configuration and investigating their physical properties. Figure 2.16 indicates an example of this kind of study, where the rotation angle-dependent change of Raman 2D peak of graphene-hBN heterostructure was investigated.[74] As other 2D materials, vertical stacking of different TMD layers is known to form unique superlattices together with other interesting physical properties that are sensitively affected by tiny change of twist angle. For example, $MoSe_2$-WSe_2 and WSe_2-WS_2 heterostructures showed stacking angle-dependent valley exciton trapping in Moiré superlattice potential.[75,76] Also, Mott insulating phases were observed in WSe_2-WS_2 heterostructure at a specific stacking angle.[77] In case of MoS_2-WS_2

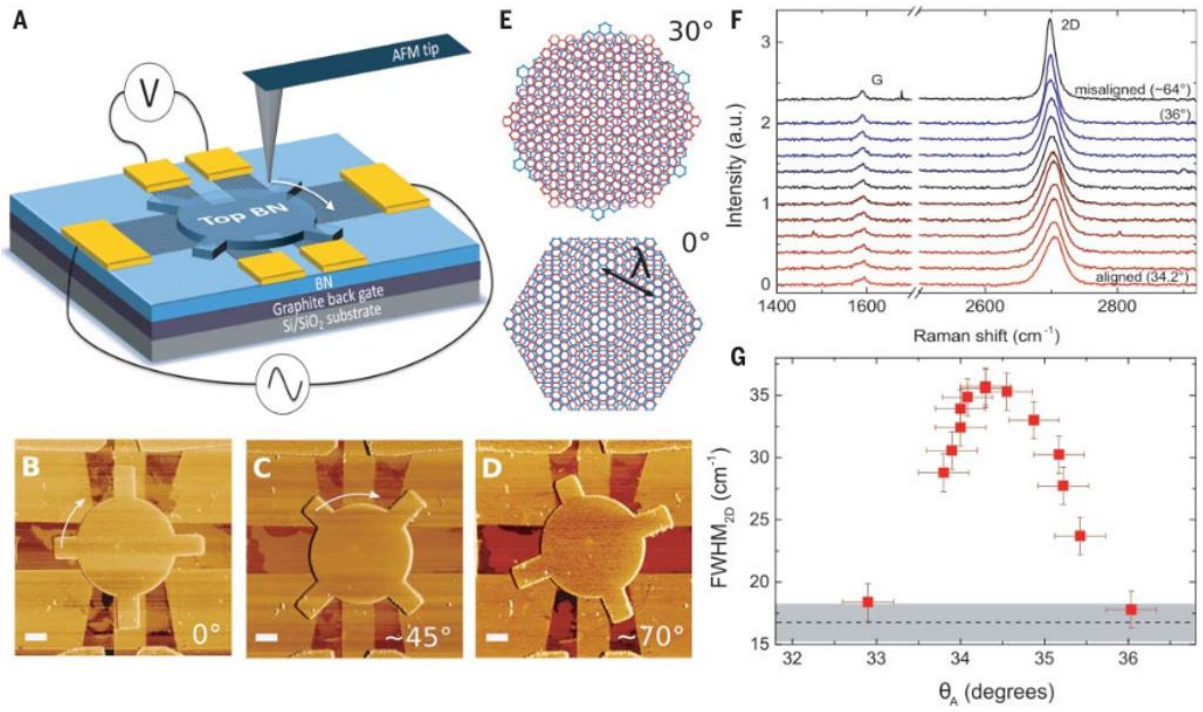

Figure 2.16. (a) Schematic of device structure and experimental technique using rotatable hexagonal boron nitride (BN) on graphene. (b-d) AFM image of a fabricated device showing three different orientations of top BN. Scale bar is 1 μm. (e) Schematic illustration of Moiré superlattice arising between graphene (red) and BN (blue) at 0° and 30°. (f) Raman spectrum of orientation-variable heterostructure shown in (b-d). (g) FWHM of Raman 2D peak as a function of stacking orientation angle. Reproduced from Ref. 74.

and $MoSe_2$-WSe_2, atomic reconstruction and corresponding change in electronic band structures were observed at small stacking angles (< 2°).[78,79] Therefore, combination of materials together with controlling their stacking configuration open a new world of physics. Here, the materials are not limited to semiconducting TMDs. The heterostructure of ABC-trilayer graphene and h-BN was found to form a special Moiré superlattice and showed tunable phase change between Mott-insulator and superconductor depending on temperature and electromagnetic environment.[80] Therefore, combining TMDs with graphene, h-BN, or other 2D materials is also expected to be an interesting research topic.[81–85]

2.2. Preparation of TMD materials

2.2.1. Mechanical exfoliation

In the beginning of graphene research, an adhesive tape was used to detach thin pieces of layered flakes from the bulk crystal. A similar method has been applied to the TMD research as well.[86] By detaching layered crystals repeatedly using the adhesive tape, thin flakes with a thickness of ~ nm can be obtained and easily transferred on target substrates such as SiO_2.[86] Figure 2.17 shows a schematic of mechanical exfoliation and successive transfer. This simplicity is one of the advantages of the mechanical exfoliation method. Another advantage is the high crystal quality of obtained flakes which is determined by the crystal quality of the bulk. Using this method, fundamental properties of various 2D materials including TMDs could have been investigated in details and various types of devices have been fabricated and studied. However, there exist several critical limitations in this mechanical exfoliation method. First, the size of the exfoliated flakes is very limited up to tens of μm, which does

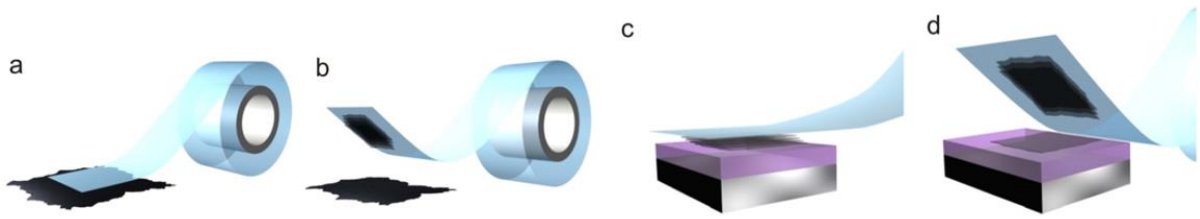

Figure 2.17. Mechanical exfoliation of 2D crystals. (a) Adhesive tape is pressed against a 2D crystal so that the top few layers are attached to the tape (b). (c) The tape with detached layered crystals is pressed against a target substrate. (d)Upon peeling off, the bottom layer is left on the substrate. Reproduced from Ref. 86.

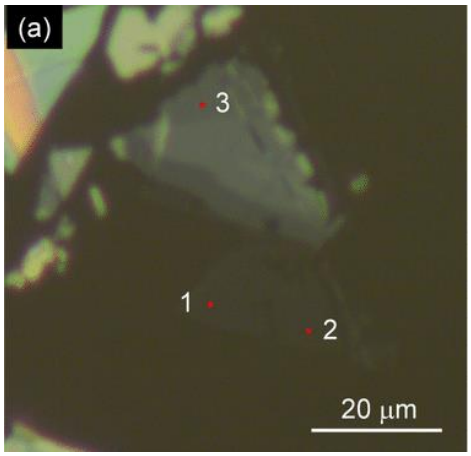

Figure 2.18. Optical image of exfoliated WS_2 flakes. Points 1, 2 and point 3 correspond to monolayer and multilayer areas, respectively. Reproduced from Ref. 87.

not fit to wafer scale device fabrication or commercialization of TMDs. Second, the thickness uniformity of obtained flakes is very poor in spite that uniform thickness film is required for systematic characterization or device fabrication. Figure 2.18 displays an optical image of WS_2 flakes prepared by mechanical exfoliation.[87] The flake thickness is ununiform and the size in only 20 μm. Therefore, as the research becomes more and more advanced, need for large size TMD films with uniform thickness became stronger. Thus, researchers began to study the bottom-to-up synthesis of TMD films using CVD method.

2.2.2. Chemical vapor deposition (CVD)

2.2.2.1. Conventional CVD

CVD is a bottom-up material synthesis method. By reacting precursors in the optimized condition, desired materials can be synthesized in a controlled manner. For conventional CVD growth of TMDs, typically a tubular furnace is used to heat precursors and growth substrate under the flow of carrier gas. Figure 2.19 shows typical CVD set up used for TMD synthesis, in which metal oxide and chalcogen powers are used as feedstocks. As a transport carrier, inert gases, such as Ar and N_2, are widely used, and mixture with H_2 or O_2 also can be used for special purposes.[88–90] Depending on target materials, low-pressure or plasma-

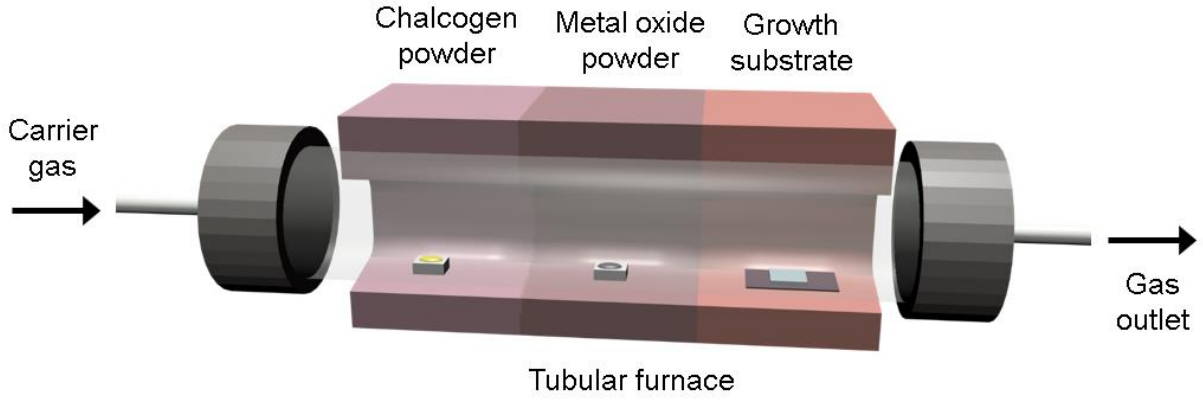

Figure 2.19. Illustration representing a typical thermal CVD set up where a tubular furnace is used for heating the precursors and growth substrate. During growth reaction, an inert carrier gas is flowed.

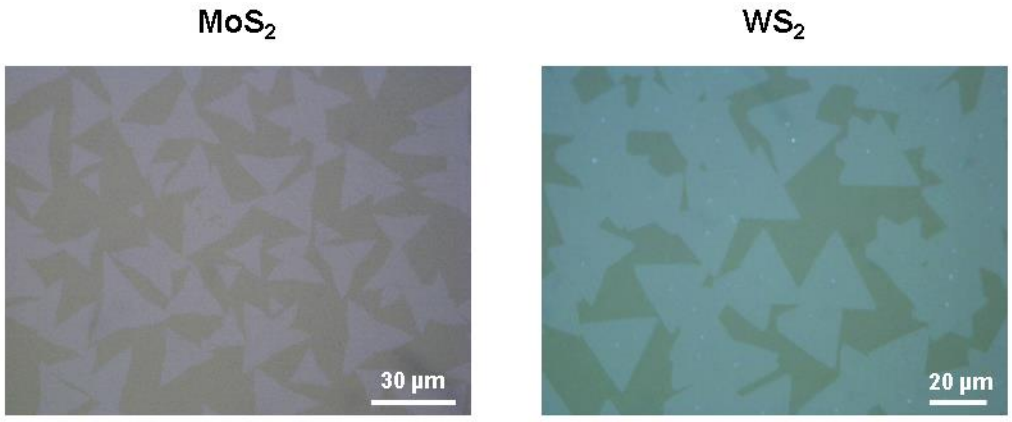

Figure 2.20. Optical images of CVD-grown MoS_2 and WS_2.

enhanced low temperature reactions are employed as well.[91,92] As precursor materials for typical TMD CVD, metal oxides (WO_3, MoO_3) and chalcogen (S, Se, Te) powders are widely used. Optimization of the amount of each precursor, reaction temperature, reaction time, gas flow rate, positions of precursors, and growth substrate, is performed to obtain TMDs with desired thickness and grain size. One big advantage of the CVD method compared with mechanical exfoliation is the capability of synthesizing large size TMD flakes (films) with much better thickness controllability. For specific purposes, wafer-scale TMD flakes and films with precisely controlled thickness are needed, thus, extensive effort has been devoted by the CVD method.[93–95] However, several problems and limitations were found in conventional CVD method where the powder type precursors are used. First, high reaction temperature which is required for lateral growth of grains causes excessive density of grain nucleation which hinders the large size growth, making a number of GBs. Figure 2.20 shows the optical images of CVD-grown MoS_2 and WS_2 on c-plane sapphire. Second, as the reaction time is increased for large size growth, the surface of metal oxide precursor is thermally reduced and stiffened, and it causes gradual reduction of supply of metal species to the growth reaction. Consequently, there is a limitation in growth reaction time which results in the size limit of the grains.

2.2.2.2. Alkali halide-assisted CVD

To reduce the high reaction temperature-induced high nucleation density and also to increase the lateral size of grown crystal, use of growth promoters was introduced.[96] As promoters, alkali-metal halides (MX where M = Na, or K and X = Cl, Br, or I) are used, and they are placed inside of the reaction chamber together with a metal oxide precursor. Figure 2.21 shows the schematic of CVD set up where the alkali halide powders are mixed with metal

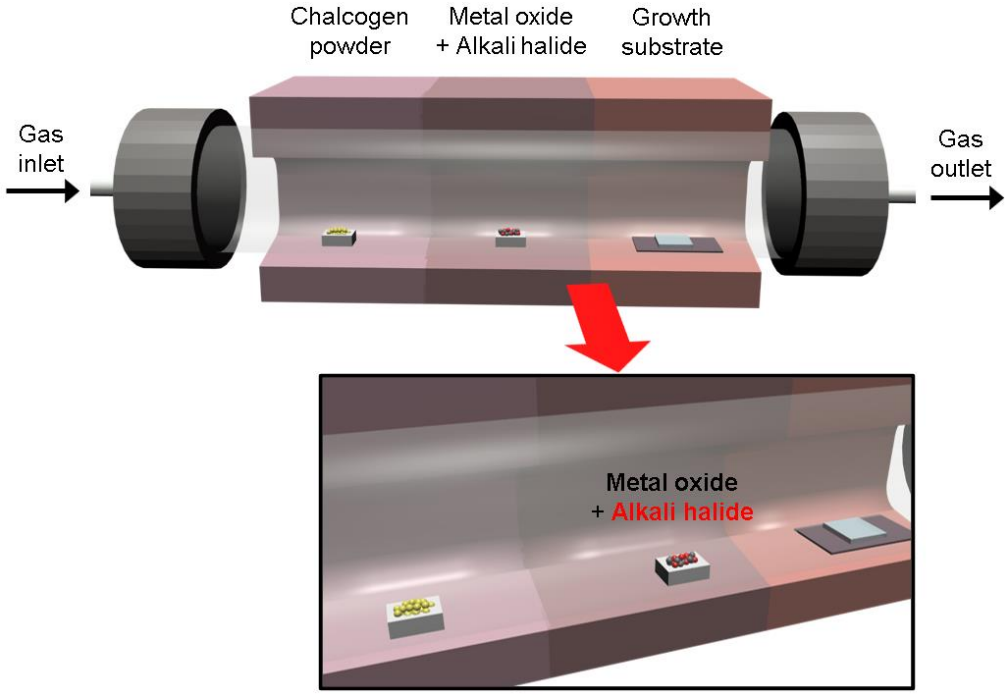

Figure 2.21. Illustration representing the alkali-halide-assisted CVD set up where alkali-halide powder is placed together with metal oxide precursor.

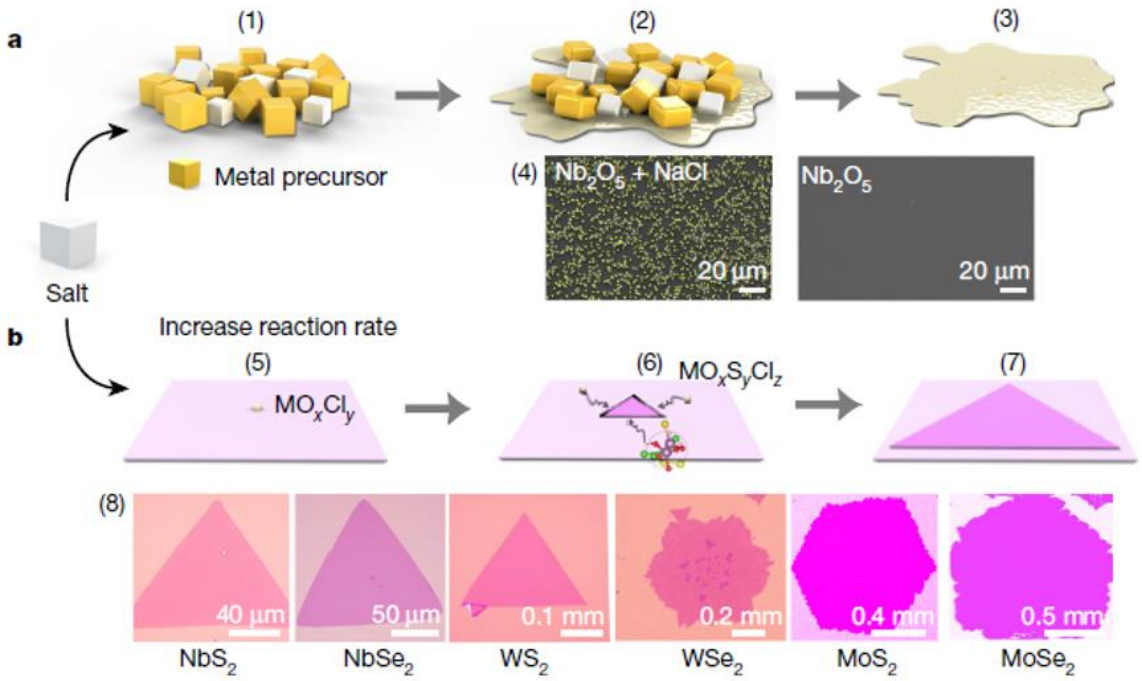

Figure 2.22. (a,b) Schematic of alkali-halide-assisted growth reaction. Metal oxychlorides are formed, and these promote the reactions. Chalcogens are not shown here. (1)-(3) The proposed process of the added salt decreasing the melting point of the precursors. (4) Scanning electron microscopic images of Nb nucleus with (left) and without (right) added to salt. (b) (5)-(7) The growth process of 2D atomic layer, with intermediate products. (8) Different single-crystalline monolayers with large size of monolayer and growth time of less than 3 min. Reproduced from Ref. 97.

oxide precursor. The alkali halide modifies the reaction between metal oxide and chalcogen atoms by forming intermediate volatile transition metal-based halide species.[96,97] Due to the lower activation energy of intermediate species formation, it is possible to nucleate and supply the enough amount of precursor flux to the growth substrate at lower temperature, which can reduce the nucleation density. Therefore, the reduced nucleation density together with enough supply of precursors further assist the lateral growth, which is beneficial for achieving growth of large single crystals and reducing the GBs. Figure 2.22 shows the example of using alkali halides to grow large single crystals of TMDs with decreased nucleation density.[97] Regarding the use growth promoters, there is a concern about possible substitutional doping and deterioration of crystal quality. However, microscopic, optical, and device studies revealed the high crystal quality free from substitutional doping together with high electrical mobility.[18,96,98]

2.2.2.3. Metal-organic CVD (MOCVD)

To solve the issue of thermal reduction-induced stiffening of metal precursor which results in limitation of growth reaction time, use of metal-organic type precursors was introduced.[99] Different from the conventional CVD, in which powder type precursors are used, in this system, metal-organic and organic chalcogen vapors are used as precursors. Figure 2.23 shows a typical CVD set up using metal-organic precursors. By bubbling the metal-organic and organic-chalcogen liquids, we can achieve constant supplies of metal and chalcogen feedstocks. Thus, uniform thickness of continuous TMD films could be obtained.[99] Due to this size-unlimited growth capability of metal organic CVD (MOCVD) system, recently, it is regarded as the most promising synthesis method for large-scale production of TMDs. Furthermore, there is an additional advantage of MOCVD system which is the tunability of precursor species

during the growth. By connecting multiple precursor source lines to the furnace and switching the precursors during the reaction, it is possible to fabricate heterostructures.[100,101] By using MOCVD method, various kinds of single-layer TMDs and their heterostructures were fabricated and their physical properties were studied.[98–101]

Thanks to the significant development of CVD technology, the controllability of grown materials has improved a lot. However, there is still an argument in CVD research regarding the low crystal quality of CVD grown TMDs. For this, several solutions have been reported to increase the crystallinity by finding better composition of carrier gas or using new types of metal-organic precursors.[89,90]

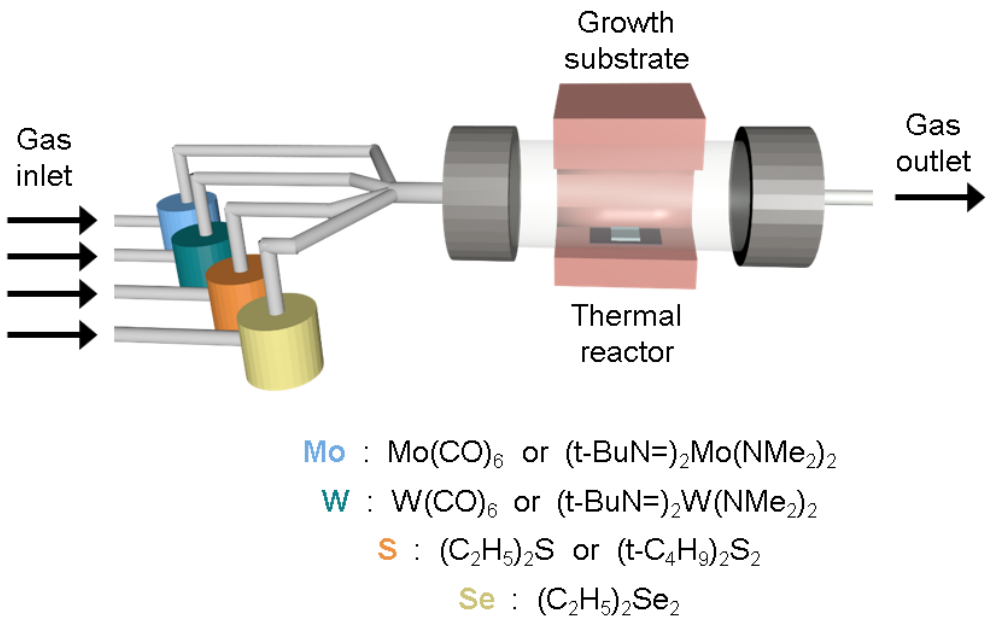

Figure 2.23. Schematic of MOCVD set up where metal-organic and chalcogen-organic gases are used as precursors. Each precursor is connected to growth chamber with separate line

References

(1) Pan, R.; Fan, X.-L.; Zhang, H.; Yang, Y. First-Principles Investigation on the Interface of Transition Metal Dichalcogenide MX_2 (*M* = Mo, *W*; X = S, Se) Monolayer on Al_2O_3(0001). *Comput. Mater. Sci.* **2016**, *122*, 118–125.

(2) Li, Y.; Duerloo, K.-A. N.; Wauson, K.; Reed, E. J. Structural Semiconductor-to-Semimetal Phase Transition in Two-Dimensional Materials Induced by Electrostatic Gating. *Nat. Commun.* **2016**, *7*, 10671.

(3) Gao, G.; Jiao, Y.; Ma, F.; Jiao, Y.; Waclawik, E.; Du, A. Charge Mediated Semiconducting-to-Metallic Phase Transition in Molybdenum Disulfide Monolayer and Hydrogen Evolution Reaction in New 1T′ Phase. *J. Phys. Chem. C* **2015**, *119*, 13124–13128.

(4) Eda, G.; Fujita, T.; Yamaguchi, H.; Voiry, D.; Chen, M.; Chhowalla, M. Coherent Atomic and Electronic Heterostructures of Single-Layer MoS_2. *ACS Nano* **2012**, *6*, 7311–7317.

(5) Amara, K. K.; Chen, Y.; Lin, Y.-C.; Kumar, R.; Okunishi, E.; Suenaga, K.; Quek, S. Y.; Eda, G. Dynamic Structural Evolution of Metal–Metal Bonding Network in Monolayer WS_2. *Chem. Mater.* **2016**, *28*, 2308–2314.

(6) Lin, Y.-C.; Nakajima, H.; Tseng, C.-W.; Li, S.; Liu, Z.; Chiu, P.-W.; Suenaga, K. Does the Metallic 1T Phase WS_2 Really Exist? arXiv:1907.11398 [cond-mat.mtrl-sci].

(7) Voß, D.; Krüger, P.; Mazur, A.; Pollmann, J. Atomic and Electronic Structure of WSe_2 from *ab initio* Theory: Bulk Crystal and Thin Film Systems. *Phys. Rev. B* **1999**, *60*, 14311–14317.

(8) Molina-Sánchez, A.; Wirtz, L. Phonons in Single and Few-Layer MoS_2 and WS_2. *Phys. Rev. B* **2011**, *84*, 155413.

(9) Berkdemir, A.; Gutiérrez, H. R.; Botello-Méndez, A. R.; Perea-López, N.; Elías, A. L.; Chia, C.-I.; Wang, B.; Crespi, V. H.; López-Urías, F.; Charlier, J.-C.; Terrones, H.; Terrones, M. Identification of Individual and Few Layers of WS_2 Using Raman Spectroscopy. *Sci. Rep.* **2013**, *3*, 1755.

(10) Liang, L.; Meunier, V. First-Principles Raman Spectra of MoS_2, WS_2 and Their Heterostructures. *Nanoscale* **2014**, *6*, 5394.

(11) Yun, W. S.; Han, S. W.; Hong, S. C.; Kim, I. G.; Lee, J. D. Thickness and Strain Effects on Electronic Structures of Transition Metal Dichalcogenides: 2H-MX_2 Semiconductors (M = Mo, W; X = S, Se, Te). *Phys. Rev. B* **2012**, *85*, 033305.

(12) Liu, G.-B.; Xiao, D.; Yao, Y.; Xu, X.; Yao, W. Electronic Structures and Theoretical Modelling of Two-Dimensional Group-VIB Transition Metal Dichalcogenides. *Chem. Soc. Rev.* **2015**, *44*, 2643–2663.

(13) Zhu, Z. Y.; Cheng, Y. C.; Schwingenschlögl, U. Giant Spin-Orbit-Induced Spin Splitting in Two-Dimensional Transition-Metal Dichalcogenide Semiconductors. *Phys. Rev. B* **2011**, *84*, 153402.

(14) Kośmider, K.; González, J. W.; Fernández-Rossier, J. Large Spin Splitting in the Conduction Band of Transition Metal Dichalcogenide Monolayers. *Phys. Rev. B* **2013**, *88*, 245436.

(15) Lu, J. M.; Zheliuk, O.; Leermakers, I.; Yuan, N. F. Q.; Zeitler, U.; Law, K. T.; Ye, J. T. Evidence for Two-Dimensional Ising Superconductivity in Gated MoS_2. *Science* **2015**, *350*, 1353–1357.

(16) Schaibley, J. R.; Yu, H.; Clark, G.; Rivera, P.; Ross, J. S.; Seyler, K. L.; Yao, W.; Xu, X. Valleytronics in 2D Materials. *Nat. Rev. Mater.* **2016**, *1*, 16055.

(17) Wakatsuki, R.; Saito, Y.; Hoshino, S.; Itahashi, Y. M.; Ideue, T.; Ezawa, M.; Iwasa, Y.; Nagaosa, N. Nonreciprocal Charge Transport in Noncentrosymmetric Superconductors.

Sci. Adv. **2017**, *3*, e1602390.

(18) Kim, H.; Ahn, G. H.; Cho, J.; Amani, M.; Mastandrea, J. P.; Groschner, C. K.; Lien, D.-H.; Zhao, Y.; Ager, J. W.; Scott, M. C.; Chrzan, D. C.; Javey, A. Synthetic WSe_2 Monolayers with High Photoluminescence Quantum Yield. *Sci. Adv.* **2019**, *5*, eaau4728.

(19) Kang, J.; Tongay, S.; Zhou, J.; Li, J.; Wu, J. Band Offsets and Heterostructures of Two-Dimensional Semiconductors. *Appl. Phys. Lett.* **2013**, *102*, 012111.

(20) Zeng, H.; Dai, J.; Yao, W.; Xiao, D.; Cui, X. Valley Polarization in MoS_2 Monolayers by Optical Pumping. *Nat. Nanotechnol.* **2012**, *7*, 490–493.

(21) Wu, S.; Huang, C.; Aivazian, G.; Ross, J. S.; Cobden, D. H.; Xu, X. Vapor–Solid Growth of High Optical Quality MoS_2 Monolayers with Near-Unity Valley Polarization. *ACS Nano* **2013**, *7*, 2768–2772.

(22) Lin, W.-H.; Tseng, W.-S.; Went, C. M.; Teague, M. L.; Rossman, George. R.; Atwater, H. A.; Yeh, N.-C. Nearly 90% Circularly Polarized Emission in Monolayer WS_2 Single Crystals by Chemical Vapor Deposition. *ACS Nano* **2020**, *14*, 1350-1359.

(23) Kioseoglou, G.; Hanbicki, A. T.; Currie, M.; Friedman, A. L.; Gunlycke, D.; Jonker, B. T. Valley Polarization and Intervalley Scattering in Monolayer MoS_2. *Appl. Phys. Lett.* **2012**, *101*, 221907.

(24) Mak, K. F.; He, K.; Shan, J.; Heinz, T. F. Control of Valley Polarization in Monolayer MoS_2 by Optical Helicity. *Nat. Nanotechnol.* **2012**, *7*, 494–498.

(25) Kioseoglou, G.; Hanbicki, A. T.; Currie, M.; Friedman, A. L.; Jonker, B. T. Optical Polarization and Intervalley Scattering in Single Layers of MoS_2 and $MoSe_2$. *Sci. Rep.* **2016**, *6*, 25041.

(26) Hanbicki, A. T.; Kioseoglou, G.; Currie, M.; Hellberg, C. S.; McCreary, K. M.; Friedman, A. L.; Jonker, B. T. Anomalous Temperature-Dependent Spin-Valley Polarization in Monolayer WS_2. *Sci. Rep.* **2016**, *6*, 18885.

(27) Nayak, P. K.; Horbatenko, Y.; Ahn, S.; Kim, G.; Lee, J.-U.; Ma, K. Y.; Jang, A.-R.; Lim, H.; Kim, D.; Ryu, S.; Cheong, H.; Park, N.; Shin, H. S. Probing Evolution of Twist-Angle-Dependent Interlayer Excitons in $MoSe_2/WSe_2$ van der Waals Heterostructures. *ACS Nano* **2017**, *11*, 4041–4050.

(28) Kunstmann, J.; Mooshammer, F.; Nagler, P.; Chaves, A.; Stein, F.; Paradiso, N.; Plechinger, G.; Strunk, C.; Schüller, C.; Seifert, G.; Reichman, D. R.; Korn, T. Momentum-Space Indirect Interlayer Excitons in Transition-Metal Dichalcogenide van der Waals Heterostructures. *Nat. Phys.* **2018**, *14*, 801–805.

(29) Hanbicki, A. T.; Chuang, H.-J.; Rosenberger, M. R.; Hellberg, C. S.; Sivaram, S. V.; McCreary, K. M.; Mazin, I. I.; Jonker, B. T. Double Indirect Interlayer Exciton in a $MoSe_2/WSe_2$ van der Waals Heterostructure. *ACS Nano* **2018**, *12*, 4719–4726.

(30) Rivera, P.; Yu, H.; Seyler, K. L.; Wilson, N. P.; Yao, W.; Xu, X. Interlayer Valley Excitons in Heterobilayers of Transition Metal Dichalcogenides. *Nat. Nanotechnol.* **2018**, *13*, 1004–1015.

(31) Karni, O.; Barré, E.; Lau, S. C.; Gillen, R.; Ma, E. Y.; Kim, B.; Watanabe, K.; Taniguchi, T.; Maultzsch, J.; Barmak, K.; Page, R. H.; Heinz, T. F. Infrared Interlayer Exciton Emission in MoS_2 / WSe_2 Heterostructures. *Phys. Rev. Lett.* **2019**, *123*, 247402.

(32) Scuri, G.; Andersen, T. I.; Zhou, Y.; Wild, D. S.; Sung, J.; Gelly, R. J.; Bérubé, D.; Heo, H.; Shao, L.; Joe, A. Y.; Mier Valdivia, A. M.; Taniguchi, T.; Watanabe, K.; Lončar, M.; Kim, P.; Lukin, M. D.; Park, H. Electrically Tunable Valley Dynamics in Twisted WSe_2 / WSe_2 Bilayers. *Phys. Rev. Lett.* **2020**, *124*, 217403.

(33) Jauregui, L. A.; Joe, A. Y.; Pistunova, K.; Wild, D. S.; High, A. A.; Zhou, Y.; Scuri, G.; Greve, K. D.; Sushko, A.; Yu, C.-H.; Taniguchi, T.; Watanabe, K.; Needleman, D. J.; Lukin, M. D.; Park, H.; Kim, P. Electrical Control of Interlayer Exciton Dynamics in Atomically Thin Heterostructures. *Science* **2019**, *366*, 870–875.

(34) Unuchek, D.; Ciarrocchi, A.; Avsar, A.; Watanabe, K.; Taniguchi, T.; Kis, A. Room-Temperature Electrical Control of Exciton Flux in a van der Waals Heterostructure. *Nature* **2018**, *560*, 340–344.

(35) Unuchek, D.; Ciarrocchi, A.; Avsar, A.; Sun, Z.; Watanabe, K.; Taniguchi, T.; Kis, A. Valley-Polarized Exciton Currents in a van der Waals Heterostructure. *Nat. Nanotechnol.* **2019**, *14*, 1104–1109.

(36) High, A. A.; Novitskaya, E. E.; Butov, L. V.; Hanson, M.; Gossard, A. C. Control of Exciton Fluxes in an Excitonic Integrated Circuit. *Science* **2008**, *321*, 229–231.

(37) Grosso, G.; Graves, J.; Hammack, A. T.; High, A. A.; Butov, L. V.; Hanson, M.; Gossard, A. C. Excitonic Switches Operating at around 100 K. *Nat. Photonics* **2009**, *3*, 577–580.

(38) Radisavljevic, B.; Radenovic, A.; Brivio, J.; Giacometti, V.; Kis, A. Single-Layer MoS_2 Transistors. *Nat. Nanotechnol.* **2011**, *6*, 147–150.

(39) Qiu, H.; Xu, T.; Wang, Z.; Ren, W.; Nan, H.; Ni, Z.; Chen, Q.; Yuan, S.; Miao, F.; Song, F.; Long, G.; Shi, Y.; Sun, L.; Wang, J.; Wang, X. Hopping Transport through Defect-Induced Localized States in Molybdenum Disulphide. *Nat. Commun.* **2013**, *4*, 2642.

(40) McDonnell, S.; Addou, R.; Buie, C.; Wallace, R. M.; Hinkle, C. L. Defect-Dominated Doping and Contact Resistance in MoS_2. *ACS Nano* **2014**, *8*, 2880–2888.

(41) Hong, J.; Hu, Z.; Probert, M.; Li, K.; Lv, D.; Yang, X.; Gu, L.; Mao, N.; Feng, Q.; Xie, L.; Zhang, J.; Wu, D.; Zhang, Z.; Jin, C.; Ji, W.; Zhang, X.; Yuan, J.; Zhang, Z. Exploring Atomic Defects in Molybdenum Disulphide Monolayers. *Nat. Commun.* **2015**, *6*, 6293.

(42) Barja, S.; Refaely-Abramson, S.; Schuler, B.; Qiu, D. Y.; Pulkin, A.; Wickenburg, S.; Ryu, H.; Ugeda, M. M.; Kastl, C.; Chen, C.; Hwang, C.; Schwartzberg, A.; Aloni, S.; Mo, S.-K.; Frank Ogletree, D.; Crommie, M. F.; Yazyev, O. V.; Louie, S. G.; Neaton, J. B.; Weber-Bargioni, A. Identifying Substitutional Oxygen as a Prolific Point Defect in Monolayer Transition Metal Dichalcogenides. *Nat. Commun.* **2019**, *10*, 3382.

(43) Li, L.; Carter, E. A. Defect-Mediated Charge-Carrier Trapping and Nonradiative Recombination in WSe_2 Monolayers. *J. Am. Chem. Soc.* **2019**, *141*, 10451–10461.

(44) Zhang, C.; Wang, C.; Yang, F.; Huang, J.-K.; Li, L.-J.; Yao, W.; Ji, W.; Shih, C.-K. Engineering Point-Defect States in Monolayer WSe_2. *ACS Nano* **2019**, *13*, 1595–1602.

(45) van der Zande, A. M.; Huang, P. Y.; Chenet, D. A.; Berkelbach, T. C.; You, Y.; Lee, G.-H.; Heinz, T. F.; Reichman, D. R.; Muller, D. A.; Hone, J. C. Grains and Grain Boundaries in Highly Crystalline Monolayer Molybdenum Disulphide. *Nat. Mater.* **2013**, *12*, 554–561.

(46) Ly, T. H.; Perello, D. J.; Zhao, J.; Deng, Q.; Kim, H.; Han, G. H.; Chae, S. H.; Jeong, H. Y.; Lee, Y. H. Misorientation-Angle-Dependent Electrical Transport across Molybdenum Disulfide Grain Boundaries. *Nat. Commun.* **2016**, *7*, 10426.

(47) Peelaers, H.; Van de Walle, C. G. Effects of Strain on Band Structure and Effective Masses in MoS_2. *Phys. Rev. B* **2012**, *86*, 241401.

(48) Jin, Z.; Li, X.; Mullen, J. T.; Kim, K. W. Intrinsic Transport Properties of Electrons and Holes in Monolayer Transition-Metal Dichalcogenides. *Phys. Rev. B* **2014**, *90*, 045422.

(49) Wang, J.; Yao, Q.; Huang, C.-W.; Zou, X.; Liao, L.; Chen, S.; Fan, Z.; Zhang, K.; Wu, W.; Xiao, X.; Jiang, C.; Wu, W.-W. High Mobility MoS_2 Transistor with Low Schottky Barrier Contact by Using Atomic Thick H-BN as a Tunneling Layer. *Adv. Mater.* **2016**, *28*, 8302–8308.

(50) Liu, Y.; Guo, J.; Zhu, E.; Liao, L.; Lee, S.-J.; Ding, M.; Shakir, I.; Gambin, V.; Huang, Y.; Duan, X. Approaching the Schottky–Mott Limit in van der Waals Metal–Semiconductor Junctions. *Nature* **2018**, *557*, 696.

(51) Cadiz, F.; Courtade, E.; Robert, C.; Wang, G.; Shen, Y.; Cai, H.; Taniguchi, T.; Watanabe, K.; Carrere, H.; Lagarde, D.; Manca, M.; Amand, T.; Renucci, P.; Tongay, S.; Marie, X.; Urbaszek, B. Excitonic Linewidth Approaching the Homogeneous Limit in MoS_2-Based

van der Waals Heterostructures. *Phys. Rev. X* **2017**, *7*, 021026.

(52) Uchida, Y.; Nakandakari, S.; Kawahara, K.; Yamasaki, S.; Mitsuhara, M.; Ago, H. Controlled Growth of Large-Area Uniform Multilayer Hexagonal Boron Nitride as an Effective 2D Substrate. *ACS Nano* **2018**, *12*, 6236–6244.

(53) Liu, S.; Yuan, K.; Xu, X.; Yin, R.; Lin, D.-Y.; Li, Y.; Watanabe, K.; Taniguchi, T.; Meng, Y.; Dai, L.; Ye, Y. Hysteresis-Free Hexagonal Boron Nitride Encapsulated 2D Semiconductor Transistors, NMOS and CMOS Inverters. *Adv. Electron. Mater.* **2018**, *5*, 1800419.

(54) Zhang, S.; Hill, H. M.; Moudgil, K.; Richter, C. A.; Walker, A. R. H.; Barlow, S.; Marder, S. R.; Hacker, C. A.; Pookpanratana, S. J. Controllable, Wide-Ranging n-Doping and p-Doping of Monolayer Group 6 Transition-Metal Disulfides and Diselenides. *Adv. Mater.* **2018**, *30*, 1806345.

(55) Tang, B.; Yu, Z. G.; Huang, L.; Chai, J.; Wong, S. L.; Deng, J.; Yang, W.; Gong, H.; Wang, S.; Ang, K.-W.; Zhang, Y.-W.; Chi, D. Direct N- to p-Type Channel Conversion in Monolayer/Few-Layer WS_2 Field-Effect Transistors by Atomic Nitrogen Treatment. *ACS Nano* **2018**, *12*, 2506–2513.

(56) Suh, J.; Park, T.-E.; Lin, D.-Y.; Fu, D.; Park, J.; Jung, H. J.; Chen, Y.; Ko, C.; Jang, C.; Sun, Y.; Sinclair, R.; Chang, J.; Tongay, S.; Wu, J. Doping against the Native Propensity of MoS_2: Degenerate Hole Doping by Cation Substitution. *Nano Lett.* **2014**, *14*, 6976–6982.

(57) Qin, Z.; Loh, L.; Wang, J.; Xu, X.; Zhang, Q.; Haas, B.; Alvarez, C.; Okuno, H.; Yong, J. Z.; Schultz, T.; Koch, N.; Dan, J.; Pennycook, S. J.; Zeng, D.; Bosman, M.; Eda, G. Growth of Nb-Doped Monolayer WS_2 from Liquid-Phase Precursor Mixing. *ACS Nano* **2019**, *13*, 10768–10775.

(58) Yang, L.; Majumdar, K.; Liu, H.; Du, Y.; Wu, H.; Hatzistergos, M.; Hung, P. Y.;

Tieckelmann, R.; Tsai, W.; Hobbs, C.; Ye, P. D. Chloride Molecular Doping Technique on 2D Materials: WS_2 and MoS_2. *Nano Lett.* **2014**, *14*, 6275–6280.

(59) Liu, X.; Qu, D.; Ryu, J.; Ahmed, F.; Yang, Z.; Lee, D.; Yoo, W. J. P-Type Polar Transition of Chemically Doped Multilayer MoS_2 Transistor. *Adv. Mater.* **2016**, *28*, 2345–2351.

(60) Jariwala, D.; Sangwan, V. K.; Lauhon, L. J.; Marks, T. J.; Hersam, M. C. Emerging Device Applications for Semiconducting Two-Dimensional Transition Metal Dichalcogenides. *ACS Nano* **2014**, *8*, 1102–1120.

(61) Jeon, P. J.; Kim, J. S.; Lim, J. Y.; Cho, Y.; Pezeshki, A.; Lee, H. S.; Yu, S.; Min, S.-W.; Im, S. Low Power Consumption Complementary Inverters with n-MoS_2 and p-WSe_2 Dichalcogenide Nanosheets on Glass for Logic and Light-Emitting Diode Circuits. *ACS Appl. Mater. Interfaces* **2015**, *7*, 22333–22340.

(62) Zhang, H.; Li, C.; Wang, J.; Hu, W.; Zhang, D. W.; Zhou, P. Complementary Logic with Voltage Zero-Loss and Nano-Watt Power via Configurable MoS_2/WSe_2 Gate. *Adv. Funct. Mater.* **2018**, *28*, 1805171.

(63) Pezeshki, A.; Hosseini Shokouh, S. H.; Jeon, P. J.; Shackery, I.; Kim, J. S.; Oh, I.-K.; Jun, S. C.; Kim, H.; Im, S. Static and Dynamic Performance of Complementary Inverters Based on Nanosheet α-$MoTe_2$ p-Channel and MoS_2 n-Channel Transistors. *ACS Nano* **2016**, *10*, 1118–1125.

(64) Resta, G. V.; Balaji, Y.; Lin, D.; Radu, I. P.; Catthoor, F.; Gaillardon, P.-E.; De Micheli, G. Doping-Free Complementary Logic Gates Enabled by Two-Dimensional Polarity-Controllable Transistors. *ACS Nano* **2018**, *12*, 7039–7047.

(65) Cho, A.-J.; Park, K. C.; Kwon, J.-Y. A High-Performance Complementary Inverter Based on Transition Metal Dichalcogenide Field-Effect Transistors. *Nanoscale Res. Lett.* **2015**, *10*, 115.

(66) Pu, J.; Funahashi, K.; Chen, C.-H.; Li, M.-Y.; Li, L.-J.; Takenobu, T. Highly Flexible

and High-Performance Complementary Inverters of Large-Area Transition Metal Dichalcogenide Monolayers. *Adv. Mater.* **2016**, *28*, 4111–4119.

(67) Tosun, M.; Chuang, S.; Fang, H.; Sachid, A. B.; Hettick, M.; Lin, Y.; Zeng, Y.; Javey, A. High-Gain Inverters Based on WSe_2 Complementary Field-Effect Transistors. *ACS Nano* **2014**, *8*, 4948–4953.

(68) Ji, H. G.; Solís-Fernández, P.; Yoshimura, D.; Maruyama, M.; Endo, T.; Miyata, Y.; Okada, S.; Ago, H. Chemically Tuned P- and n-Type WSe_2 Monolayers with High Carrier Mobility for Advanced Electronics. *Adv. Mater.* **2019**, *31*, 1903613.

(69) Gao, L.; Liao, Q.; Zhang, X.; Liu, X.; Gu, L.; Liu, B.; Du, J.; Ou, Y.; Xiao, J.; Kang, Z.; Zhang, Z.; Zhang, Y. Defect-Engineered Atomically Thin MoS_2 Homogeneous Electronics for Logic Inverters. *Adv. Mater.* **2020**, *32*, 1906646.

(70) Xiao, D.; Liu, G.-B.; Feng, W.; Xu, X.; Yao, W. Coupled Spin and Valley Physics in Monolayers of MoS_2 and Other Group-VI Dichalcogenides. *Phys. Rev. Lett.* **2012**, *108*, 196802.

(71) Mak, K. F.; McGill, K. L.; Park, J.; McEuen, P. L. The Valley Hall Effect in MoS_2 Transistors. *Science* **2014**, *344*, 1489–1492.

(72) Huang, Z.; Liu, Y.; Dini, K.; Tan, Q.; Liu, Z.; Fang, H.; Liu, J.; Liew, T.; Gao, W. Robust Room Temperature Valley Hall Effect of Interlayer Excitons. *Nano Lett.* **2020**, *20*, 1345–1351.

(73) Cao, Y.; Fatemi, V.; Fang, S.; Watanabe, K.; Taniguchi, T.; Kaxiras, E.; Jarillo-Herrero, P. Unconventional Superconductivity in Magic-Angle Graphene Superlattices. *Nature* **2018**, *556*, 43–50.

(74) Ribeiro-Palau, R.; Zhang, C.; Watanabe, K.; Taniguchi, T.; Hone, J.; Dean, C. R. Twistable Electronics with Dynamically Rotatable Heterostructures. *Science* **2018**, *361*, 690–693.

(75) Seyler, K. L.; Rivera, P.; Yu, H.; Wilson, N. P.; Ray, E. L.; Mandrus, D. G.; Yan, J.; Yao, W.; Xu, X. Signatures of Moiré-Trapped Valley Excitons in $MoSe_2/WSe_2$ Heterobilayers. *Nature* **2019**, *567*, 66–70.

(76) Jin, C.; Regan, E. C.; Yan, A.; Iqbal Bakti Utama, M.; Wang, D.; Zhao, S.; Qin, Y.; Yang, S.; Zheng, Z.; Shi, S.; Watanabe, K.; Taniguchi, T.; Tongay, S.; Zettl, A.; Wang, F. Observation of Moiré Excitons in WSe_2/WS_2 Heterostructure Superlattices. *Nature* **2019**, *567*, 76–80.

(77) Regan, E. C.; Wang, D.; Jin, C.; Bakti Utama, M. I.; Gao, B.; Wei, X.; Zhao, S.; Zhao, W.; Zhang, Z.; Yumigeta, K.; Blei, M.; Carlström, J. D.; Watanabe, K.; Taniguchi, T.; Tongay, S.; Crommie, M.; Zettl, A.; Wang, F. Mott and Generalized Wigner Crystal States in WSe_2/WS_2 Moiré Superlattices. *Nature* **2020**, *579*, 359–363.

(78) Weston, A.; Zou, Y.; Enaldiev, V.; Summerfield, A.; Clark, N.; Zólyomi, V.; Graham, A.; Yelgel, C.; Magorrian, S.; Zhou, M.; Zultak, J.; Hopkinson, D.; Barinov, A.; Bointon, T. H.; Kretinin, A.; Wilson, N. R.; Beton, P. H.; Fal'ko, V. I.; Haigh, S. J.; Gorbachev, R. Atomic Reconstruction in Twisted Bilayers of Transition Metal Dichalcogenides. *Nat. Nanotechnol.* https://doi.org/10.1038/s41565-020-0682-9.

(79) Rosenberger, M. R.; Chuang, H.-J.; Phillips, M.; Oleshko, V. P.; McCreary, K. M.; Sivaram, S. V.; Hellberg, C. S.; Jonker, B. T. Twist Angle-Dependent Atomic Reconstruction and Moiré Patterns in Transition Metal Dichalcogenide Heterostructures. *ACS Nano* **2020**, *14*, 4550-4558.

(80) Chen, G.; Sharpe, A. L.; Gallagher, P.; Rosen, I. T.; Fox, E. J.; Jiang, L.; Lyu, B.; Li, H.; Watanabe, K.; Taniguchi, T.; Jung, J.; Shi, Z.; Goldhaber-Gordon, D.; Zhang, Y.; Wang, F. Signatures of Tunable Superconductivity in a Trilayer Graphene Moiré Superlattice. *Nature* **2019**, *572*, 215–219.

(81) Geim, A. K.; Grigorieva, I. V. Van der Waals Heterostructures. *Nature* **2013**, *499*, 419–

425.

(82) Li, Y.; Stolte, N.; Li, B.; Li, H.; Cheng, G.; Pan, D.; Wang, J. Interface Charge-Transfer Induced Intralayer Excited-State Biexcitons in Graphene/WS_2 van der Waals Heterostructures. *Nanoscale* **2019**, *11*, 13552–13557.

(83) Du, L.; Yu, H.; Liao, M.; Wang, S.; Xie, L.; Lu, X.; Zhu, J.; Li, N.; Shen, C.; Chen, P.; Yang, R.; Shi, D.; Zhang, G. Modulating PL and Electronic Structures of MoS_2/Graphene Heterostructures via Interlayer Twisting Angle. *Appl. Phys. Lett.* **2017**, *111*, 263106.

(84) Liao, M.; Wu, Z.-W.; Du, L.; Zhang, T.; Wei, Z.; Zhu, J.; Yu, H.; Tang, J.; Gu, L.; Xing, Y.; Yang, R.; Shi, D.; Yao, Y.; Zhang, G. Twist Angle-Dependent Conductivities across MoS_2 /Graphene Heterojunctions. *Nat. Commun.* **2018**, *9*, 4068.

(85) Yan, X.; Liu, C.; Li, C.; Bao, W.; Ding, S.; Zhang, D. W.; Zhou, P. Tunable $SnSe_2$/WSe_2 Heterostructure Tunneling Field Effect Transistor. *Small* **2017**, *13*, 1701478.

(86) Novoselov, K. S.; Castro Neto, A. H. Two-Dimensional Crystals-Based Heterostructures: Materials with Tailored Properties. *Phys. Scr.* **2012**, *T146*, 014006.

(87) Wang, F.; Kinloch, I. A.; Wolverson, D.; Tenne, R.; Zak, A.; O'Connell, E.; Bangert, U.; Young, R. J. Strain-Induced Phonon Shifts in Tungsten Disulfide Nanoplatelets and Nanotubes. *2D Mater.* **2017**, *4*, 015007.

(88) Sheng, Y.; Tan, H.; Wang, X.; Warner, J. H. Hydrogen Addition for Centimeter-Sized Monolayer Tungsten Disulfide Continuous Films by Ambient Pressure Chemical Vapor Deposition. *Chem. Mater.* **2017**, *29*, 4904–4911.

(89) Ji, H. G.; Lin, Y.-C.; Nagashio, K.; Maruyama, M.; Solís-Fernández, P.; Sukma Aji, A.; Panchal, V.; Okada, S.; Suenaga, K.; Ago, H. Hydrogen-Assisted Epitaxial Growth of Monolayer Tungsten Disulfide and Seamless Grain Stitching. *Chem. Mater.* **2018**, *30*, 403–411.

(90) Chen, W.; Zhao, J.; Zhang, J.; Gu, L.; Yang, Z.; Li, X.; Yu, H.; Zhu, X.; Yang, R.; Shi, D.; Lin, X.; Guo, J.; Bai, X.; Zhang, G. Oxygen-Assisted Chemical Vapor Deposition Growth of Large Single-Crystal and High-Quality Monolayer MoS_2. *J. Am. Chem. Soc.* **2015**, *137*, 15632–15635.

(91) Zhang, Y.; Yao, Y.; Sendeku, M. G.; Yin, L.; Zhan, X.; Wang, F.; Wang, Z.; He, J. Recent Progress in CVD Growth of 2D Transition Metal Dichalcogenides and Related Heterostructures. *Adv. Mater.* **2019**, *31*, 1901694.

(92) Cai, Z.; Liu, B.; Zou, X.; Cheng, H.-M. Chemical Vapor Deposition Growth and Applications of Two-Dimensional Materials and Their Heterostructures. *Chem. Rev.* **2018**, *118*, 6091–6133.

(93) Liao, M.; Wei, Z.; Du, L.; Wang, Q.; Tang, J.; Yu, H.; Wu, F.; Zhao, J.; Xu, X.; Han, B.; Liu, K.; Gao, P.; Polcar, T.; Sun, Z.; Shi, D.; Yang, R.; Zhang, G. Precise Control of the Interlayer Twist Angle in Large Scale MoS_2 Homostructures. *Nat. Commun.* **2020**, *11*, 2153.

(94) Lan, C.; Kang, X.; Wei, R.; Meng, Y.; Yip, S.; Zhang, H.; Ho, J. C. Utilizing a NaOH Promoter to Achieve Large Single-Domain Monolayer WS_2 Films via Modified Chemical Vapor Deposition. *ACS Appl. Mater. Interfaces* **2019**, 11, 35238-35246.

(95) Yu, H.; Liao, M.; Zhao, W.; Liu, G.; Zhou, X. J.; Wei, Z.; Xu, X.; Liu, K.; Hu, Z.; Deng, K.; Zhou, S.; Shi, J.-A.; Gu, L.; Shen, C.; Zhang, T.; Du, L.; Xie, L.; Zhu, J.; Chen, W.; Yang, R.; Shi, D.; Zhang, G. Wafer-Scale Growth and Transfer of Highly-Oriented Monolayer MoS_2 Continuous Films. *ACS Nano* **2017**, *11*, 12001–12007.

(96) Li, S.; Wang, S.; Tang, D.-M.; Zhao, W.; Xu, H.; Chu, L.; Bando, Y.; Golberg, D.; Eda, G. Halide-Assisted Atmospheric Pressure Growth of Large WSe_2 and WS_2 Monolayer Crystals. *Appl. Mater. Today* **2015**, *1*, 60–66.

(97) Zhou, J.; Lin, J.; Huang, X.; Zhou, Y.; Chen, Y.; Xia, J.; Wang, H.; Xie, Y.; Yu, H.; Lei,

J.; Wu, D.; Liu, F.; Fu, Q.; Zeng, Q.; Hsu, C.-H.; Yang, C.; Lu, L.; Yu, T.; Shen, Z.; Lin, H.; Yakobson, B. I.; Liu, Q.; Suenaga, K.; Liu, G.; Liu, Z. A Library of Atomically Thin Metal Chalcogenides. *Nature* **2018**, *556*, 355–359.

(98) Kim, H.; Ovchinnikov, D.; Deiana, D.; Unuchek, D.; Kis, A. Suppressing Nucleation in Metal–Organic Chemical Vapor Deposition of MoS_2 Monolayers by Alkali Metal Halides. *Nano Lett.* **2017**, *17*, 5056-5063.

(99) Kang, K.; Xie, S.; Huang, L.; Han, Y.; Huang, P. Y.; Mak, K. F.; Kim, C.-J.; Muller, D.; Park, J. High-Mobility Three-Atom-Thick Semiconducting Films with Wafer-Scale Homogeneity. *Nature* **2015**, *520*, 656–660.

(100) Xie, S.; Tu, L.; Han, Y.; Huang, L.; Kang, K.; Lao, K. U.; Poddar, P.; Park, C.; Muller, D. A.; DiStasio, R. A.; Park, J. Coherent, Atomically Thin Transition-Metal Dichalcogenide Superlattices with Engineered Strain. *Science* **2018**, *359*, 1131–1136.

(101) Kobayashi, Y.; Yoshida, S.; Maruyama, M.; Mogi, H.; Murase, K.; Maniwa, Y.; Takeuchi, O.; Okada, S.; Shigekawa, H.; Miyata, Y. Continuous Heteroepitaxy of Two-Dimensional Heterostructures Based on Layered Chalcogenides. *ACS Nano* **2019**, *13*, 7527–7535.

Chapter 3

Hydrogen-Assisted Epitaxial Growth of Monolayer Tungsten Disulfide and Seamless Grain Stitching

Abstract

Recently, research on TMDs has been accelerated by the development of large-scale synthesis based on CVD. However, in most cases, CVD-grown TMD sheets are composed of randomly oriented grains, and thus contain many distorted GBs which deteriorate the physical properties of the TMD. In this chapter, the epitaxial growth of monolayer tungsten disulfide (WS_2) on sapphire is demonstrate by introducing a high concentration of hydrogen during the CVD process. As opposed to the randomly oriented grains obtained in conventional growth, the presence of H_2 resulted in the formation of triangular WS_2 grains with the well-defined orientation determined by the underlying sapphire substrate. Photoluminescence of the aligned WS_2 grains was significantly suppressed compared to that of the randomly oriented grains, indicating a hydrogen-induced strong coupling between WS_2 and the sapphire surface that has been confirmed by density functional theory (DFT) calculations. Scanning transmission electron microscope observations revealed that the epitaxially grown WS_2 has less structural defects and impurities. Furthermore, sparsely distributed unique dislocations were observed between merging aligned grains, indicating an effective stitching of the merged grains. This contrasts with the GBs that are observed between randomly oriented grains, which include series of 8-, 7-, and alternating 7/5-membered rings along the GB. The GB structures were

also found to have a strong impact on the chemical stability and carrier transport of merged WS_2 grains. This chapter demonstrates a novel method to grow high-quality TMD sheets with much less structural defects, contributing to the future development of TMD-based electronic and photonic applications.

3.1. Introduction

Monolayers of TMDs have been attracting an intensive interest as one of the representative families of 2D materials. In contrast to the gapless nature of monolayer graphene, monolayers of TMDs, such as molybdenum disulfide (MoS_2) and tungsten disulfide (WS_2), have direct band gaps of 1~2 eV. Thus, these materials show strong PL in the visible range and also allow excellent semiconductor device operation with high on/off ratios.[1,2] Large-scale synthesis of TMD monolayers is essential to develop electronic and optoelectronic applications. While recent development of the CVD methods has enabled the wafer-scale production of TMD monolayers,[3–10] there still exist several issues that degrade the device performance of the CVD-grown TMD sheets. First, the TMD growth is not based on surface self-limiting mechanism so that the growth occurs not only on the substrate surface but also on the surface of the TMD itself. This makes difficult to synthesize highly uniform monolayer films, as multilayer spots are frequently observed at the center of monolayer grains.[3–6] Accordingly, many multilayer grains are formed when the TMD growth is continued to fully cover the substrate.[6,7] Second, the lattice orientation of each TMD grain is not controlled, which results in the formation of polycrystalline TMD sheets having many GBs with a wide range of misorientation angles.[11–15] Although the pre-annealing process of sapphire substrates in air was reported to result in aligned growth of MoS_2,[16] this method has not been successfully applied to other TMD

monolayers, such as WS_2. Graphene and h-BN act as good templates to obtain aligned TMD grains due to interlayer van der Waals interaction, but the TMD grain size is limited, typically less than 1 μm,[17–20] and the use of other 2D materials complicates the process and increases the costs.

Among the various existing TMDs, WS_2 possesses promising properties, such as strong photo- and electroluminescence, the spin-valley coupling phenomenon, non-toxicity of the source materials, and a lower effective mass of electrons compared with MoS_2 and $MoSe_2$.[21–24] These properties make monolayer WS_2 a promising candidate for electronics, photonics, and valleytronics. In most of the CVD studies, WS_2 is grown from tungsten oxide (WO_3) and sulfur (S) precursors in the flow of an inert gas, mainly Ar.[8,14,25] Recently, the addition of hydrogen has been found to improve the quality of TMDs.[26–29] The added H_2 gas, usually at concentrations below 10%, can produce defined grain edges,[26] increase the photoluminescence intensity,[27] promote reduction of a metal oxide source,[28] and suppress the multilayer growth.[29] In this chapter, high concentrations of H_2 gas (> 40%) during the CVD growth in shown to assist the alignment of triangular WS_2 grains along the c-plane sapphire substrate. Compared with the case of the randomly oriented grains obtained for pure Ar, the PL and Raman signals from the aligned WS_2 grains were strongly suppressed. This suggests enhancement of the WS_2-sapphire interaction that ultimately assists the WS_2 alignment. DFT calculations were also performed to explain the enhanced WS_2-sapphire interaction induced by the H_2 supply. STEM observations revealed the presence of unique and defined dislocations between connected aligned grains. On the contrary, randomly oriented WS_2 grains have various distorted GBs which are consisting of arrays of 8-, 7-, and alternating 7/5-membered rings. This study also indicates that the merged aligned WS_2 grains show higher chemical stability and improved transport properties compared with the randomly oriented WS_2 grains. The results of this

work offers a new tactic for the large-scale growth of highly crystalline TMD sheets by minimizing the effects of GBs, enhancing the potential applications of 2D materials.

3.2. Experimental method

3.2.1. CVD growth of WS_2

WS_2 was synthesized using WO_3 (99.998%) and sulfur powder (99.999%) on c-plane sapphire substrate using a tubular furnace with a heating belt. The CVD setup is illustrated in Figure 3.1. The inner diameter of the quartz tube is 26 mm. Pure Ar gas (99.999%) and mixture with H_2 gas (99.99999%) were flown during the CVD process, while keeping a total flow rate of 100 ccm. The temperatures of the WO_3 precursor (with the sapphire substrate on top) and sulfur were set at 825 °C and 210 °C, respectively. The growth time was 30 minutes. When H_2 gas is used in addition to Ar, caution is required not to inhale H_2S gas by venting the out-line gas after neutralization.

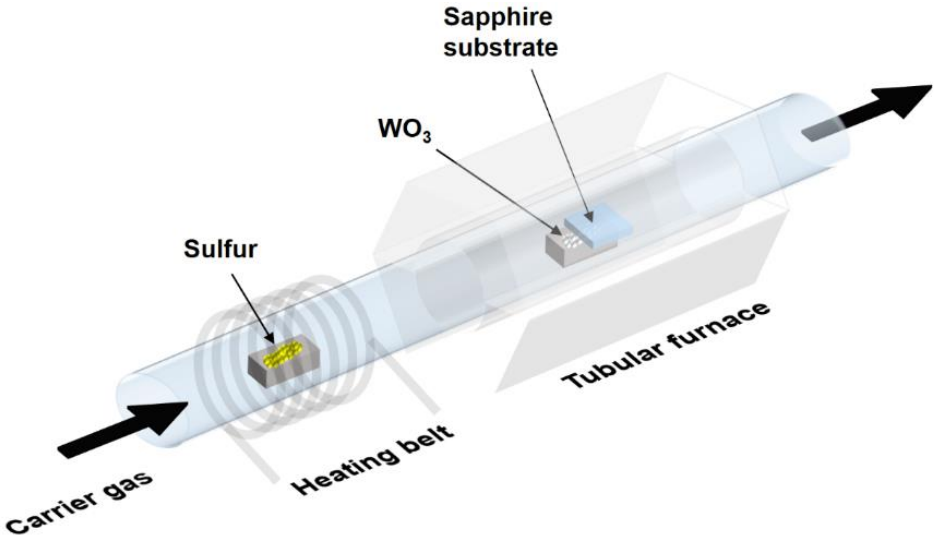

Figure 3.1. CVD setup used for the growth of monolayer WS_2. A sapphire substrate was placed on top of the WO_3 boat.

3.2.2. Characterization methods

Scanning electron microscope (SEM) images were measured with a HITACHI S-4800 with 1 kV acceleration voltage. Atomic force microscope (AFM) images were measured with a Bruker Nanoscope V. PL and Raman spectra were measured with a Tokyo Instruments, Nanofinder 30 using a 473 nm laser beam with low power (100 μW and 600 μW for PL and Raman, respectively). Annular dark-field STEM (ADF-STEM) images were measured by using JEOL 2100F equipped with double delta correctors operating at the acceleration voltage of 60 kV. The probe current was about 25 pA. The convergence angle and the inner acquisition angle were 35 mrad and 79 mrad. The electron energy-loss spectroscopy (EELS) spectra were taken by using a Gatan low-voltage quantum spectrometer.

3.2.3. DFT calculations

Theoretical calculations were performed using DFT with the generalized gradient approximation (GGA-PBE)[30] and van der Waals (vdW) corrections (vdW-DF2-C09)[31,32] implemented in the STATE package.[33] Vanderbilt ultrasoft pseudopotentials were used to describe electron-ion interactions.[34] Valence wave function and deficit charge density were expanded in terms of plane-wave basis with cutoff energy of 25 and 225 Ry, respectively. Surfaces of Al_2O_3 were simulated by a repeated slab model of α-Al_2O_3 thin films with 8 atomic layers. Al- and H-terminated Al_2O_3 surfaces were used to model H_2-WS_2 and Ar-WS_2 growth, respectively. To calculate the adsorption energy of a WS_2 grain on the Al_2O_3 slab, the 4 × 4 lateral cell was adopted to exclude the interaction with the periodic images of WS_2 grain. The triangular WS_2 grain with lateral length of 1.2 nm was constructed using 15 W and 36 S atoms. To avoid an unphysical dipole interaction with periodic images normal to the α-Al_2O_3 slab arising from the polar (111)/($\bar{1}\bar{1}\bar{1}$) surfaces, the effective screening medium (ESM) method

was adopted.[35] The geometric structures were optimized until the force acting on atoms was less than 0.01 Ry/Å under the fixed lattice parameter.

3.2.4. Device fabrication and measurement

SiO_2(90 nm)/n^+-Si substrate was cleaned with acetone and isopropyl alcohol (IPA) by sonication for 10 minutes each. WS_2 flakes were transferred onto prepared SiO_2/Si substrates using the polystyrene-assisted transfer technique.[36] Transferred WS_2 was spin coated by polymethyl methacrylate (PMMA) and patterned using electron beam (EB) lithography, followed by thermal evaporation of Ti/Au electrodes in vacuum and lift-off. Device measurement was conducted at room temperature in vacuum at 10^{-3} Pa with a bias voltage of 1 V.

3.3. Results and discussion

3.3.1. Hydrogen-assisted epitaxial growth of WS_2

Figure 3.2a,b shows SEM images of WS_2 grains synthesized by ambient-pressure CVD using H_2-Ar mixed gas (H_2: 50%) and pure Ar gas, which are denoted hereafter as H_2-WS_2 and Ar-WS_2, respectively. For the WS_2 synthesis, WO_3 and sulfur powders were used as precursor with the c-plane sapphire substrate placed on top of the WO_3 boat without any nucleation seeds. Most of the CVD parameters, such as total gas flow rate, growth time, and substrate temperature were set to the same values for both H_2-WS_2 and Ar-WS_2, except for the gas composition and the amount of sulfur powder (a larger amount of sulfur was necessary for the H_2-WS_2 growth, as the formation of H_2S leads to higher consumption of sulfur).

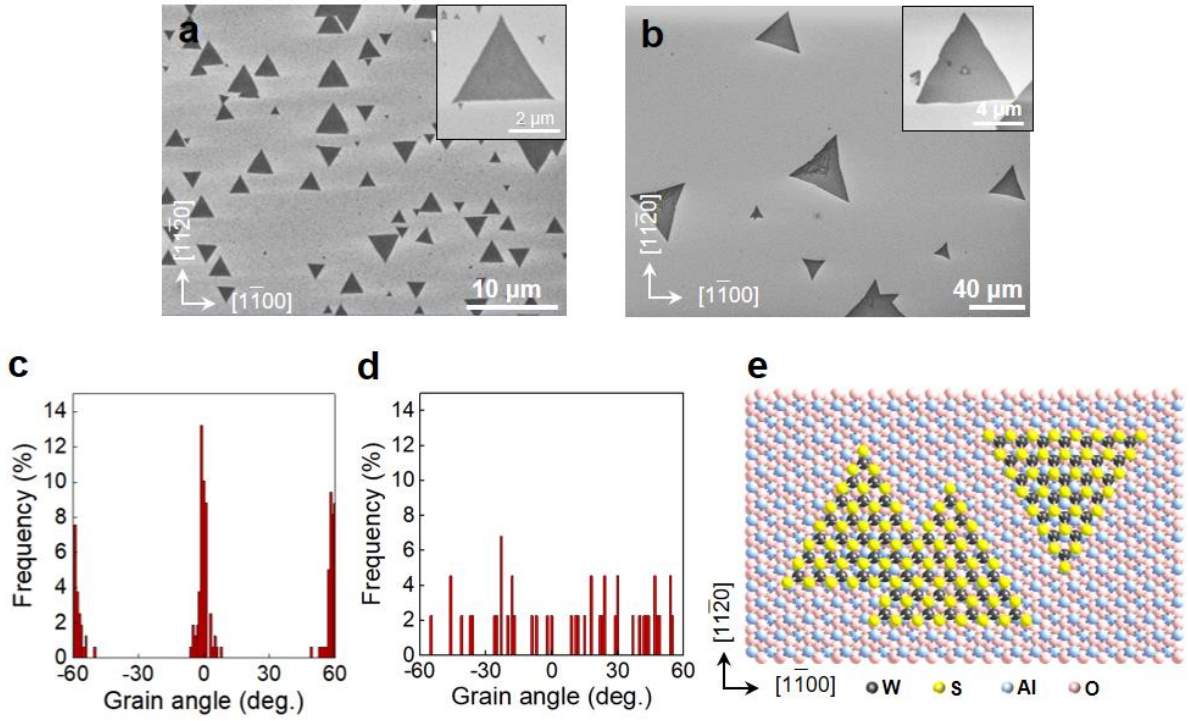

Figure 3.2. SEM images and angle distributions of the as-grown H_2-WS_2 (a,c) and Ar-WS_2 (b,d) grains. Arrows in (a) and (b) show the crystal orientations of the c-sapphire substrate. (e) Atomic structure of WS_2 grains oriented on c-plane sapphire observed for H_2-WS_2 samples.

In the case of Ar-WS_2, triangular grains are randomly oriented on the sapphire substrate (Figure 3.2b), as reported in the previous literatures.[5,9,26,37] In contrast, most of the H_2-WS_2 grains are oriented along only two directions (Figure 3.2a). One side of these oriented WS_2 grains is aligned parallel to the [1$\bar{1}$00] direction of the underlying sapphire substrate, as seen in Figure 3.2a. This result suggests an epitaxial growth of WS_2 grains assisted by the H_2. Figure 3.2c,d shows the angle distribution of WS_2 grains. In the presence of H_2 gas, 94% of the WS_2 grains are aligned to the [1$\bar{1}$00] direction within ±5° dispersion, signifying the orientation of WS_2 is determined by the sapphire surface. The CVD results obtained with other H_2 concentrations are shown in Figure 3.3. Relatively high H_2 concentrations over 40% were found to improve the WS_2 alignment (see Figure 3.4). Figure 3.2e depicts the

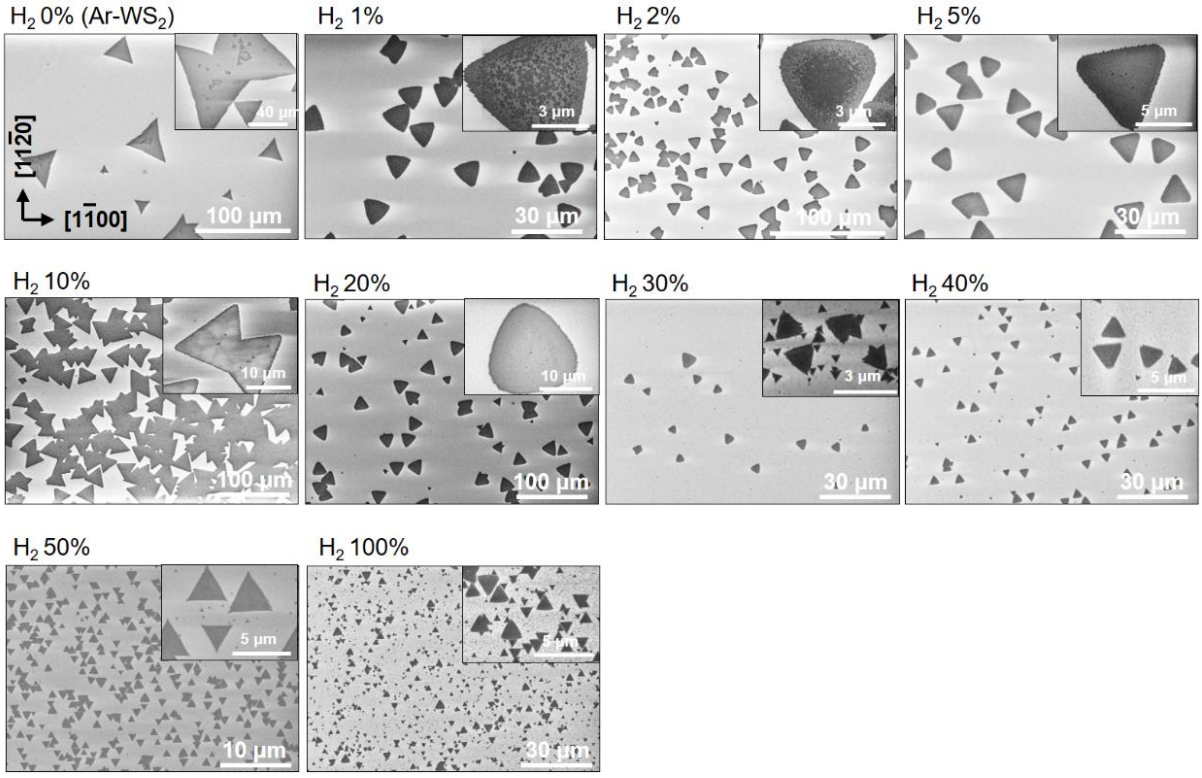

Figure 3.3. SEM images of WS_2 grains grown under different H_2 concentrations. Total flow rate was fixed to be 100 sccm. All the samples are set in the same direction designated in H_2 0% image.

orientation of WS_2 grains with respect to the underlying sapphire lattice. Although the lattice mismatch between WS_2 (0.315 nm) and c-plane sapphire (0.476 nm) is large (34.4%),[38,39] van der Waals epitaxy allows the alignment of the H_2-WS_2 grains on sapphire. The aligned growth can lead to perfect connection of the neighboring WS_2 grains having the same orientation without any GBs, as illustrated in the left part of Figure 3.2e, which will be discussed later.

AFM images of H_2-WS_2 and Ar-WS_2 grains are shown in Figures 3.5a,b, respectively. The height of the H_2-WS_2 grains was ~0.8 nm, suggesting the formation of monolayer WS_2.[26] It can be seen that the H_2-WS_2 grains are almost free from multilayer areas at their centers (Figure 3.5a). In contrast, the Ar-WS_2 grains contain thick overgrown multilayers at the center of monolayer grains (bright triangles in Figure 3.5b). The height of the multilayer grains is

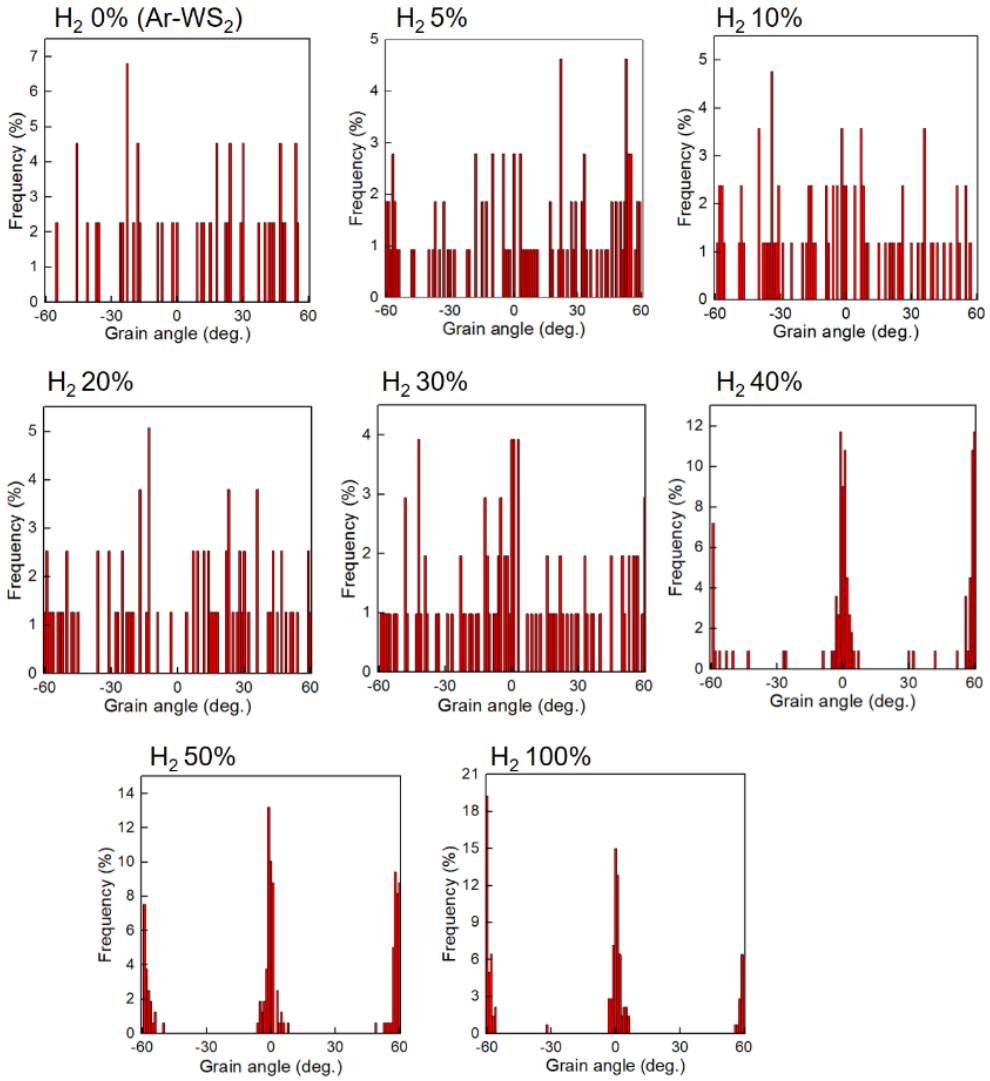

Figure 3.4. Histograms of grain orientation distribution corresponding to the samples shown in Figure 3.3. The [$1\bar{1}00$] direction of the sapphire substrate is set as 0˚. Grains of WS_2 show the preferential alignment under the hydrogen concentration higher than 40%.

generally higher than 100 nm. These multilayer grains are widely observed in samples of different TMDs grown by CVD, and it becomes more severe when the growth time is extended to fully cover the sapphire surface, because the coverage of the overgrown multilayers increases with the growth time.[3–7] It is speculated that H_2 gas introduced during the WS_2 growth process etches multilayer nuclei when they appear on the monolayer WS_2, thus suppressing the

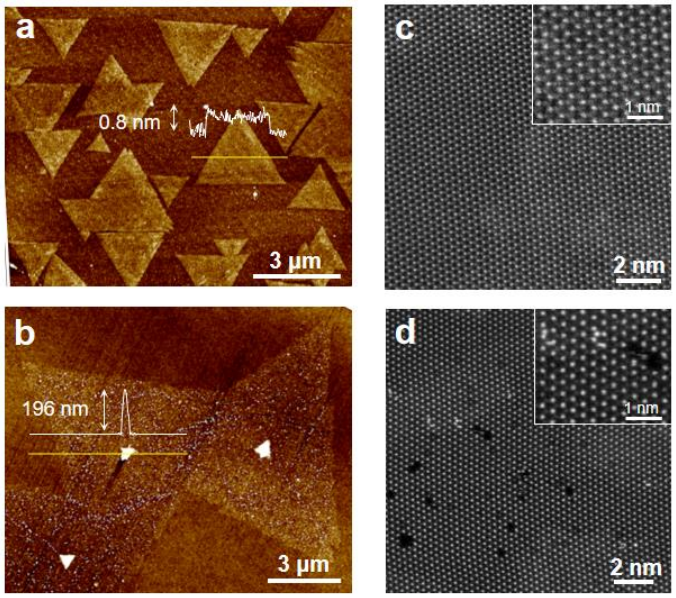

Figure 3.5. AFM and ADF-STEM images the H_2-WS_2 (a,c) and Ar-WS_2 (b,d) grains.

formation of multilayer WS_2 growth. This is consistent with the recent literature reporting that the addition of H_2 in low concentrations (5%) suppresses the formation of multilayer WS_2.[29] The H_2-assisted etching, at the same time, reduces the growth rate of H_2-WS_2, resulting in smaller grains compared with the Ar-WS_2 grains (see Figure 3.2a,b).

To evaluate the crystallinity of the WS_2 grains, ADF-STEM was measured for both H_2-WS_2 and Ar-WS_2 samples, as shown in Figures 3.5c,d. Bright and dark spots in the images correspond to W and S atoms, respectively. The Ar-WS_2 grain contains several point defects (Figure 3.5d), which include vacancies and impurities. Metal impurities are assigned to Mo from the EELS analysis (see Figure 3.6). Although the origin of these metal impurities is not clear, contamination due to impurities in the feedstock and/or from sources used for MoS_2 growth in our laboratory (even though different setup is used for each TMD) may occur, because TMD monolayers are highly susceptible to the unintentional substitutional doping.[40] However, as seen in Figure 3.6a, the number of defects and impurities was much smaller for

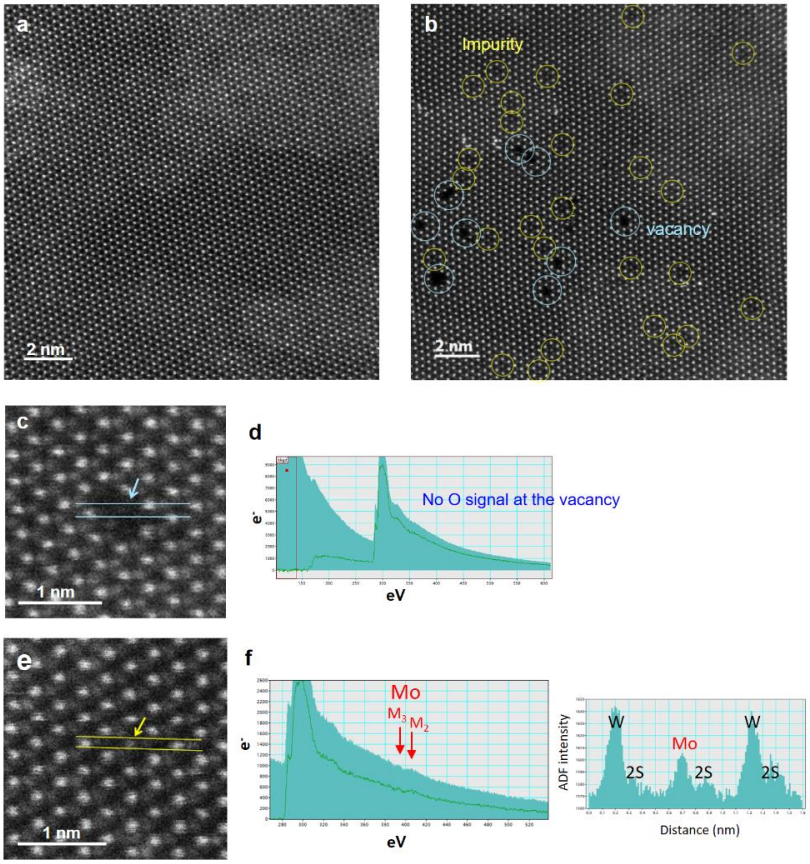

Figure 3.6. ADF-STEM images of H_2-WS_2 (a) and Ar-WS_2 (b) grains. The Ar-WS_2 grain has a higher amount of impurities and vacancies as compared with H_2-WS_2. (c-f) ADF-STEM images and EELS data of vacancy (c,d) and impurity (e,f). The right panel of (f) shows the ADF intensity, suggesting the presence of a Mo atom in the lattice.

the H_2-WS_2 grains. There are two possible reasons for this lack of defects when using H_2. First, H_2 can reduce precursors more effectively, converting WO_3 and S to WO_{3-x} and H_2S, respectively, which helps to improve the crystallinity by reducing structural defects caused by oxygen included in WO_3 source.[27] This was confirmed by the X-ray photoelectron spectroscopy (XPS) measurements, as shown in Figure 3.7. The H_2-WS_2 sample shows the preferential formation of WS_2, while the Ar-WS_2 shows the presence of WO_3 and/or WO_xS_y species on the sapphire surface in addition to WS_2. The second reason for the suppression of

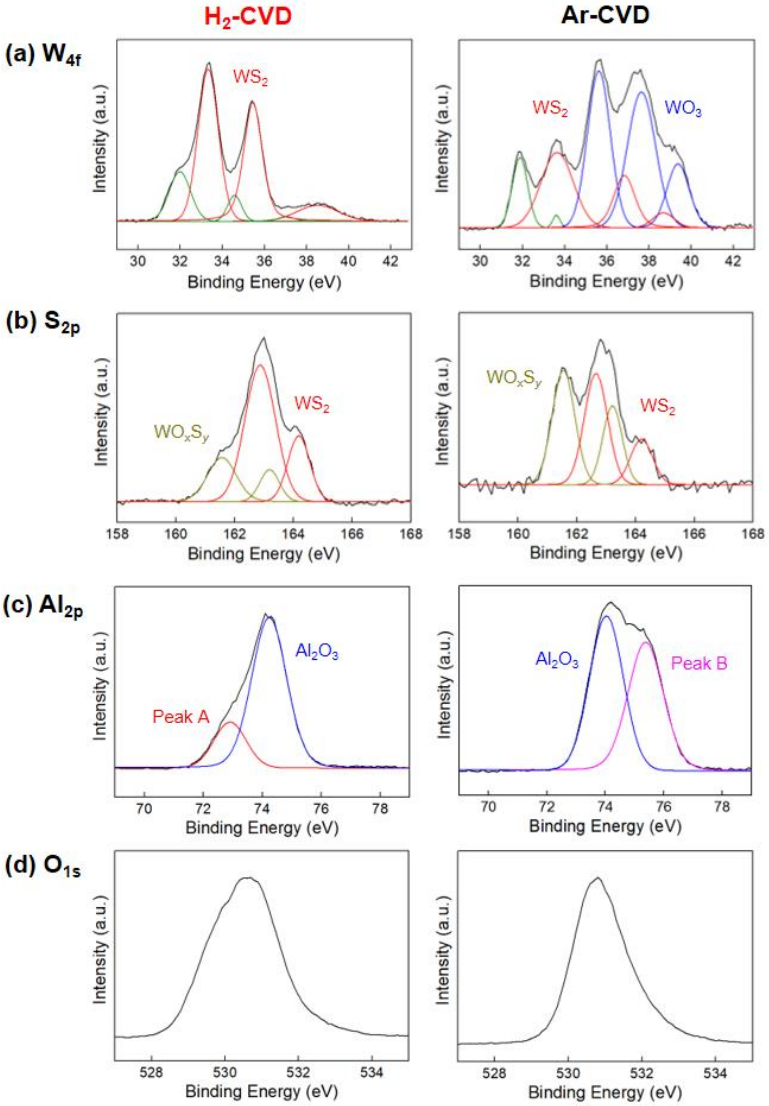

Figure 3.7. XPS spectra of sapphire surfaces after WS_2 growth with and without H_2 gas. The surface coverage of WS_2 is around 10%.

defects in the H_2-WS_2 grains is that H_2 may be able to heal the defects formed within the WS_2 lattices. Since defects are more energetically unstable, they can be easily eliminated by H_2 during the growth, which allows to reconstruct the WS_2 crystalline lattice. This phenomenon is related to the observed suppression of overgrown multilayer WS_2 by removing the multilayer nuclei from monolayer grains. As shown earlier, the use of H_2 during the CVD assists the

epitaxial growth of aligned WS_2 grains with almost no structural defects. Therefore, physical properties of TMD monolayers grown with the aid of H_2 are expected to be improved, as will be discussed later.

It has been reported that MoS_2 grains can be aligned on sapphire in pure Ar flow (i.e. without H_2 gas).[16,41] We have also observed the grain alignment of MoS_2 on sapphire in the absence of H_2.[42] In contrast, for WS_2 grains, I have not observed the grain alignment when no H_2 is supplied regardless of the substrate position (either above the WO_3 precursor or downstream of it) and the growth condition (different temperatures and Ar flow rates). Also, there has been no previous reports of the WS_2 alignment as far as I know. Thus, the aligned growth of WS_2 is much more difficult to achieve than that of MoS_2, which may be related to the surface condition of the sapphire substrate. As the H_2 gas can clean the sapphire surface and gives the WS_2 alignment, it is expected that H_2-assisted CVD method can be applied to other TMDs, such as WSe_2.

3.3.2. Optical properties of WS_2 grains

To understand the optical properties of the WS_2 grains, PL spectra from WS_2 grains grown with and without H_2 gas during the CVD process were measured. Figure 3.8a shows the PL intensity map of an as-grown Ar-WS_2 grain on sapphire substrate. While the PL intensity is weak at the center due to the presence of multilayer grain,[10,21,43] most of the area shows strong emission. On the other hand, the PL from the as-grown H_2-WS_2 was strongly suppressed at the central parts of the grains, although the edges show clear PL emission (Figures 3.8b and Figure 3.9). There are two possible reasons for the observed reduction of the PL intensity of the H_2-WS_2 grains; structural defects in the grains[44,45] or a strong coupling (or charge transfer)) with the underlying sapphire.[17,46,47] As shown in Figures 3.8c and Figure 3.9, the PL became

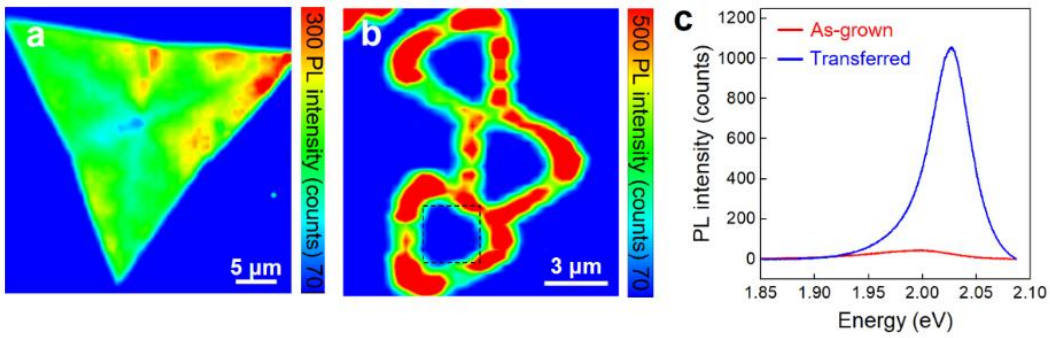

Figure 3.8. (a) PL intensity maps of as-grown Ar-WS_2 (a) and H_2-WS_2 (b) on sapphire. (c) PL spectra collected from the H_2-WS_2 grain shown in (b) before and after the transfer to SiO_2/Si substrate. The averaged PL spectra collected from the square indicated in (b) of the identical WS_2 grain are compared.

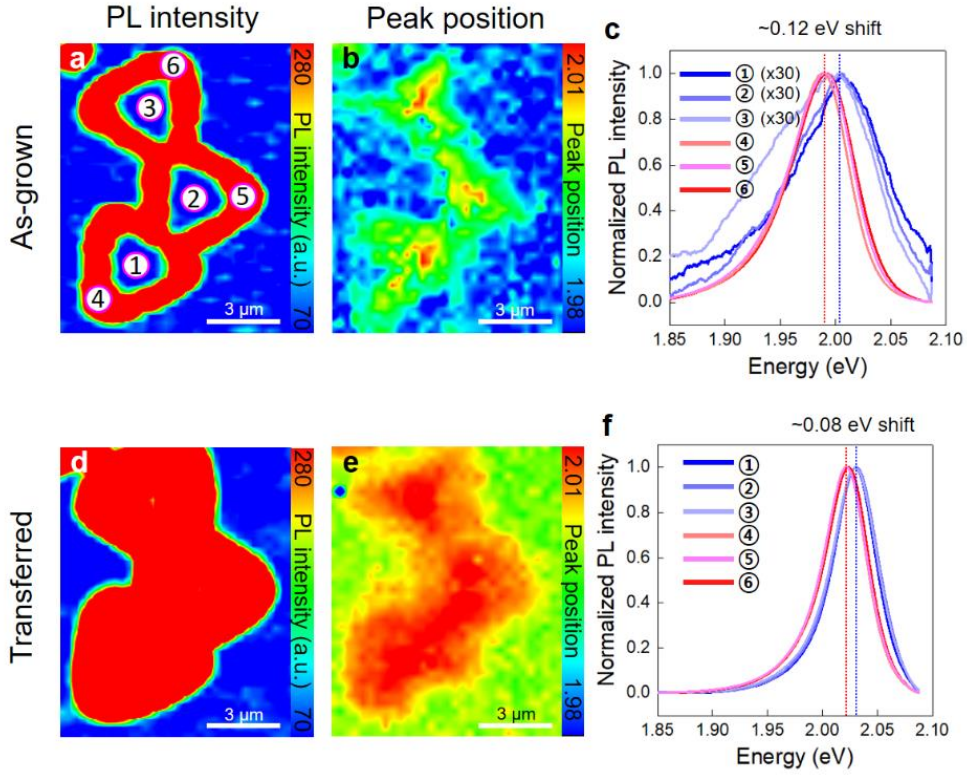

Figure 3.9. PL analysis of (a-c) as-grown and (d-f) transferred H_2-WS_2. (a,d) PL intensity. (b,e) PL peak position. Normalized PL spectra (c,f) were measured from the marked points in (a). (c) and (f) show slight red-shift of the PL peak with increasing intensity from the center to the edge of the H_2-WS_2 grains, suggesting doping at the grain edges by gaseous molecules in ambient air.

much stronger after transferring the H_2-WS_2 grains onto a SiO_2/Si substrate. If the PL quenching in the as-grown sample (Figure 3.8b) would be related to structural defects, then the PL should remain weak after the transfer. However, given that the transferred H_2-WS_2 grains

show PL from the whole grains, the PL quenching in the as-grown H_2-WS_2 grains seems to originate from the interaction between the WS_2 and the sapphire surface. It is noted that the light reflection by the underlying SiO_2 substrate also contributes to the enhanced PL from the transferred H_2-WS_2 grains. The PL intensity from the Ar-WS_2 grains also increased after the transfer. However, the suppression of the PL mainly at the central part of the H_2-WS_2 grains is quite different from the Ar-WS_2, signifying the substantial influence of sapphire to the H_2-WS_2 grains.

It is speculated that the emission from the edges of H_2-WS_2 grains reflects the reduction of the WS_2-sapphire interaction induced by the intercalation of gaseous molecules in ambient air and/or the successive p-type doping from the molecules (see Figure 3.9), which may occur gradually in air.[48] After the transfer, the PL peak shifted from 2.00 eV to 2.03 eV (see Figure 3.8c). It is likely that tensile strain, arising during the cooling down process due to the different thermal expansion coefficients of WS_2 and sapphire, is relaxed during the transfer process.[49]

I also investigated the influence of gas environment by switching from pure Ar to a H_2-Ar gas mixture during the WS_2 growth period. The result is shown in Figure 3.10. Two different kinds of WS_2 grains were observed on the sapphire surface after the CVD; large misaligned grains nucleated during the Ar period at the beginning, and small aligned grains grown during the H_2-Ar period. The latter showed a reduced PL, while the former gave the intense PL emission. These results confirm the strong influence of H_2 gas on the characteristics of WS_2 grains.

Figure 3.11a shows the Raman spectra of the as-grown Ar-WS_2 (black) and H_2-WS_2 (red) grains measured using a 473 nm laser excitation. Both samples showed clear E^1_{2g} and A_{1g} peaks with a peak separation of 62 cm^{-1}, evidencing the formation of monolayer WS_2.[49] The Raman intensity of the H_2-grown sample was found to be weaker, less than half of that of the

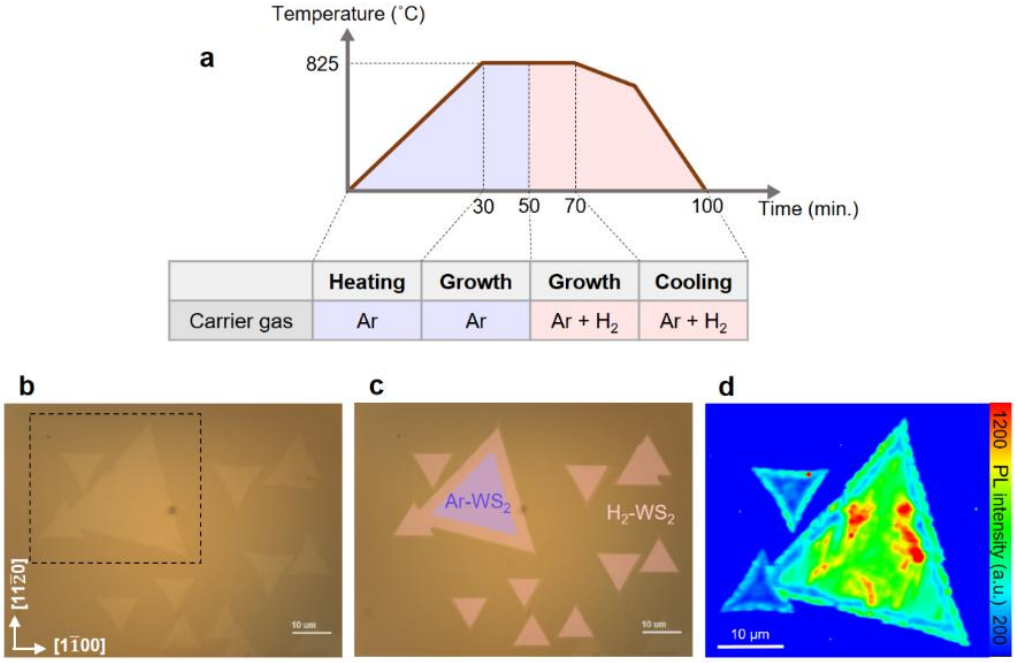

Figure 3.10. CVD growth of WS_2 by switching pure Ar to H_2-Ar mixed gas during the CVD growth. (a) CVD profile and the corresponding carrier gas composition. (b) Optical micrograph of the WS_2 grains on sapphire. (c) The same image with (b) highlight of the growth periods. (d) PL intensity map taken at the dashed square shown in (b). It is clearly seen the WS_2 grains that grow during flowing H_2-Ar are aligned and show weaker PL, while the grain formed during Ar flow is misoriented and exhibits stronger PL.

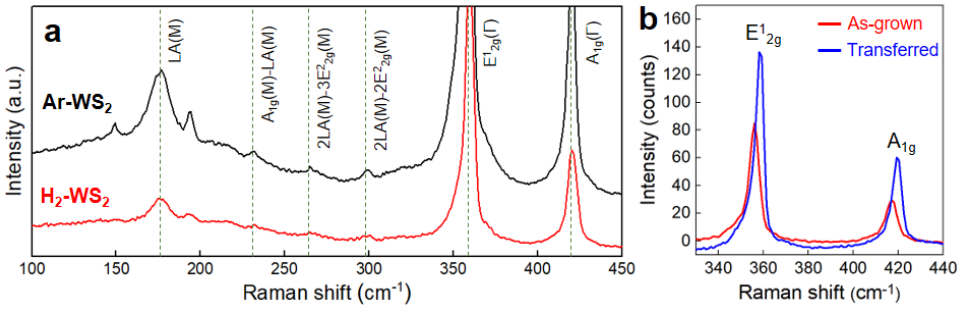

Figure 3.11. (a) Raman spectra of the as-grown samples. (b) Raman spectra of the identical H_2-WS_2 grain taken before and after the transfer.

Ar-grown sample measured under the same condition. This lowering of the Raman intensity seen for the H_2-WS_2 also can be attributed to the effective WS_2-sapphire coupling, considering the fewer structural defects and higher purity compared to Ar-WS_2 grains (see Figure 3.5c,d). The enhancement of the Raman intensity after the transfer process, shown in Figure 3.11b, also

supports this conclusion. While the suppression of the PL from the H_2-WS_2 is ascribed to the strong orbital interaction between WS_2 and sapphire, the reduced Raman intensity can be explained by modulation of phonon modes of the H_2-WS_2 due to strong interaction between WS_2 and Al-terminated sapphire surface. This is supported by the DFT calculations, as mentioned later. In addition, the release of strain can be seen from the Raman shift after the transfer.[49]

3.3.3. Analyses of sapphire surfaces

Considering the previous literature that reports the desorption of surface oxygen from sapphire surface by heating in hydrogen at 823 °C,[50] it is highly likely that hydrogen supplied during the CVD removes the surface oxygen at elevated temperature. This is expected to result in oxygen-deficient, Al-rich sapphire surface. Thus, the chemical states of sapphire surfaces were measured by XPS (see Figure 3.7c,d). In the H_2-assisted CVD, the main Al_{2p} peak associated with α-Al_2O_3 (74.2 eV) and a small peak are observed at lower binding energy (peak A (72.7 eV) in Figure 3.7). The low binding energy indicates that some of Al is less positively charged than that of α-Al_2O_3, being consistent with the expected oxygen-deficient surface state. On the other hand, the sapphire after the CVD with pure Ar showed an additional Al_{2p} peak at a higher binding energy (peak B in Figure 3.7c). This can be assigned to oxygen-rich sapphire, presumably suggesting the presence of OH-terminated sapphire

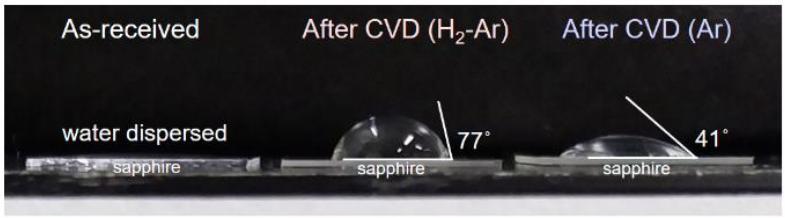

Figure 3.12. Water contact angle measurements for the pristine sapphire and the sapphire after the CVD with H_2-Ar and pure Ar flows.

surface. The oxygen concentration ([O]/([Al]+[O])) of the sapphire surface submitted to the H_2-assisted CVD (47.1%) was lower than that of sapphire submitted to standard Ar CVD (48.1%). As the sapphire substrates were exposed to air during the transport to the XPS chamber after the CVD process, which inevitably causes surface adsorption of oxygen and water molecules, the difference of the measured oxygen concentrations may have become smaller. The deviation from the stoichiometry of α-Al_2O_3 (60%) can be also due to the heat-induced desorption of surface oxygen.[51]

For macroscopic inspection of the sapphire surface, the water contact angle was measured. As shown in Figure 3.12, the sapphire surface after the H_2-WS_2 growth showed a much higher contact angle than that after the Ar-WS_2 growth. This is consistent with the XPS results; the sapphire reacted with H_2 has less surface oxygen, making the sapphire surface more hydrophobic. It is considered that the Al-rich, active sapphire surface, formed by H_2, induces the strong interaction with the growing WS_2 grains, guiding their lattice orientation to align along the sapphire's surface potential.

I also investigated the CVD growth in pure Ar flow using a sapphire substrate which was annealed in H_2 flow (100%) prior to the CVD. Figure 3.13 shows the SEM image and PL spectrum. Although the WS_2 grain shape is not highly defined, a partial alignment was observed, with the WS_2 grains elongated along a crystal direction of the sapphire. Also, the PL was weaker than that of grains grown on non-annealed sapphire substrate. Thus, the high temperature treatment in H_2 gas influences the chemical structure of the sapphire surface, highly likely assisting the WS_2 alignment. It was reported that the step edges of c-plane sapphire substrates can guide the growth of aligned TMDs.[52,53] However, although step/terrace structures on the sapphire surfaces after the CVD with H_2-Ar gas (Figure 3.14), the WS_2 orientation did not follow the step edge direction. This proves that the WS_2 alignment in our H_2-assisted CVD is based on the atomic lattice of c-plane sapphire surface.

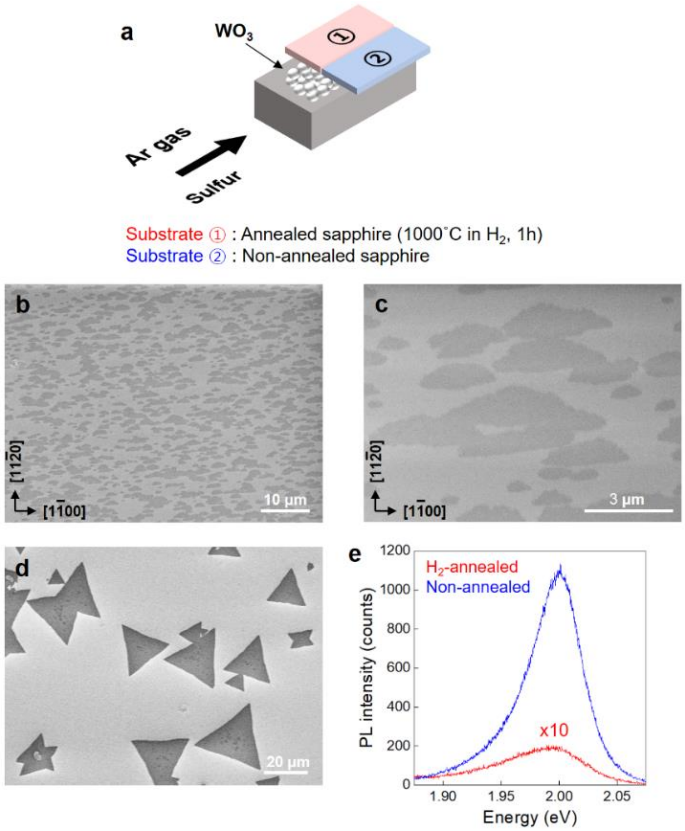

Figure 3.13. Effect of the H_2 pre-annealing of sapphire prior to the CVD growth with pure Ar gas. (a) Experimental procedure. SEM images of the sapphire surface pre-annealed in H_2 (b,c) and that without pre-annealing (d). (d) corresponds to the standard Ar-WS_2 grains. (e) PL spectra of WS_2 grains.

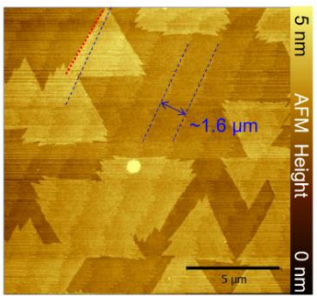

Figure 3.14. AFM images of the sapphire surface after the H_2-assisted CVD growth. The WS_2 grains are oriented in two directions, but not aligned along the step/terrace direction.

For further understanding of the influence of H_2-induced WS_2 alignment, DFT calculations were performed using the slab models shown in Figure 3.15. Here, triangular WS_2 grains with 1.2 nm lateral size are adsorbed on α-Al_2O_3 slabs whose surfaces are terminated with Al

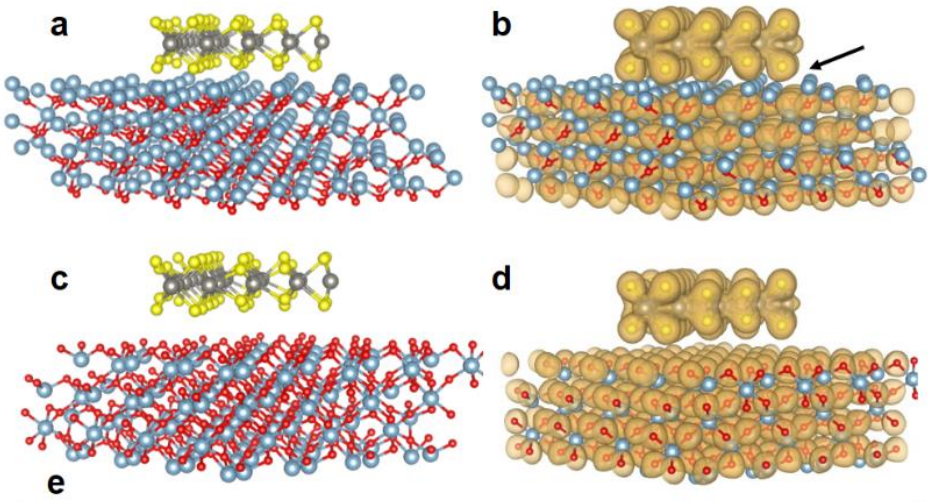

Sapphire surface	WS_2-sapphire distance	Adsorption energy*
Al-terminated	0.15 nm	- 24.93 eV
O-terminated	0.29 nm	- 11.96 eV

* Adsorption energy per one triangular WS_2 grain consisting of 51 atoms

Figure 3.15. DFT calculation results of triangular WS_2 grains adsorbed on Al-terminated (a,b) and O-terminated (c,d) sapphire surfaces. (a,c) Atomic structures after geometry optimization. Other structural images can be found in Figure 3.16. (b,d) Spatial distribution of valence electrons. Yellow: S, gray: W, blue: Al, red: O atoms. The arrow in (b) indicates the distorted S $2p_z$ orbital due to strong interaction with the atomic orbitals of Al atoms of sapphire surface. (e) Comparison of WS_2-sapphire distances and adsorption energies.

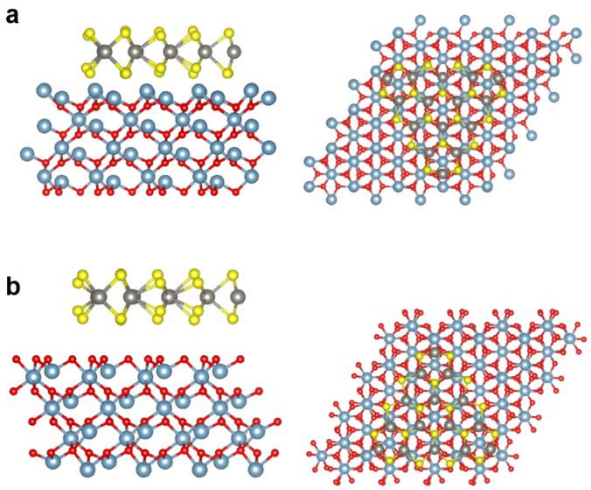

Figure 3.16. Atomic structures of WS_2 grains adsorbed on Al- (a) and O-terminated (b) sapphire. Left and right images show the side and top view images, respectively. These structures are identical to those shown in Figure 3.15. It is clearly seen that the WS_2-sapphire distance after geometry optimization is shorter for the Al-terminated surface (a) than the O-terminated one, indicating the stronger interaction between WS_2 and the Al-terminated sapphire.

atoms (Figure 3.15a) and O atoms (Figure 3.15c). As discussed above, the Al- and O-terminated surfaces correspond to the H_2-WS_2 and Ar-WS_2 cases, respectively. It was found that after geometry optimization, the WS_2-sapphire distance is shorter for the Al-terminated surface (see Figure 3.15a, 0.15 nm) than for the O-terminated one (Figure 3.15c, 0.29 nm). In addition, in the valence electron distribution shown in Figure 3.15b, the S 2p orbital is extended to the sapphire surface, suggesting the orbital hybridization of WS_2 and the Al-terminated sapphire surface. Reflecting this strong coupling, the measured adsorption energy was much higher for the Al-terminated than the O-terminated surfaces (Figure 3.15e). Thus, the PL quenching and the reduced Raman intensity observed in the H_2-WS_2 can be ascribed to this strong WS_2-sapphire coupling.

3.3.4. Observation of WS_2 grain boundaries

The hydrogen-assisted epitaxy found in this work motivated us to measure the atomic structures of the interfaces between merged WS_2 grains, as misorientation angles greatly influence the GB structures and transport properties.[15] In this study, we analyzed the interface between aligned WS_2 grains merged with a low misorientation angle realized by our H_2-assisted CVD growth technique, in addition to the GBs of rotated grains with large misorientation angles (Ar-WS_2). Figure 3.17a shows the low magnification STEM image of a GB with a low misorientation angle of ~4°. In the SEM and AFM images shown in Figures 3.2a and 3.5a, the triangular WS_2 grains look highly aligned, but there may be slight misalignment between neighboring grains due to the tapered or round triangular structures as well as thermal fluctuation during the CVD growth.

Interestingly, as shown in Figure 3.17a, there was no linear defect (or GB) along the interface between the two merged H_2-WS_2 grains, which is widely observed in the merged TMD

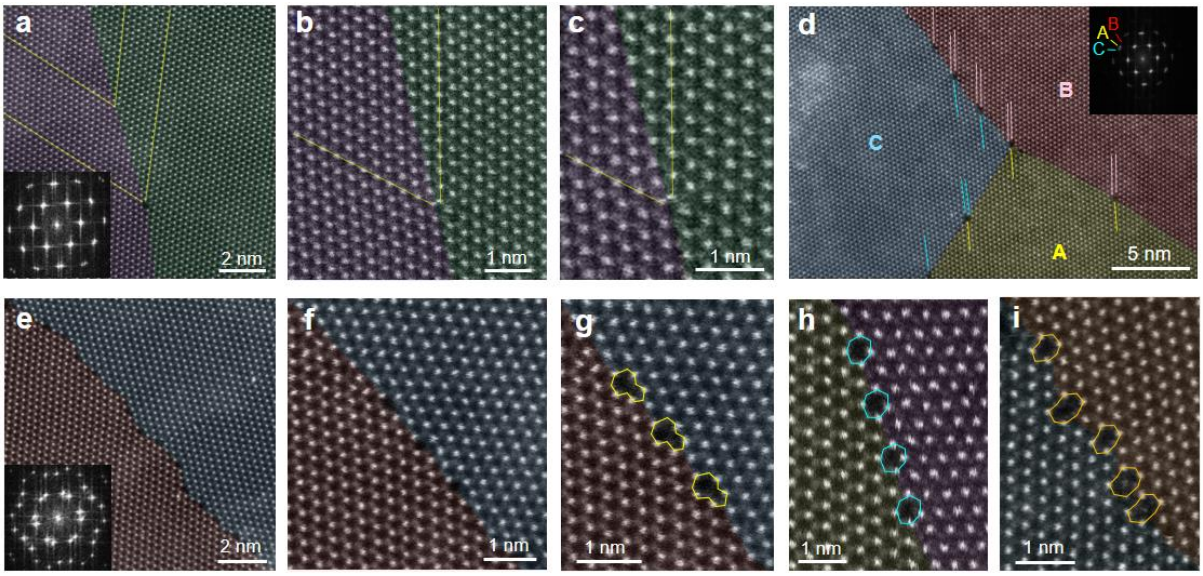

Figure 3.17. (a-d) ADF-STEM images of GBs of H_2-WS_2. (a-c) GB structures with misorientation angle of ~4°. (d) Three-fold merging GBs with 2° and -4° of mismatch angles. The marked lines indicate dislocations. (e-i) ADF-STEM images of GBs of large angle misoriented Ar-WS_2. Different merging angles of (e-g) 19°, (h) 24° and (i) 10° resulted in different GB structures: (e-g) 7-5-membered rings, (h) 7-membered rings and (i) 8-membered rings.

grains.[12–15] Instead, one-dimensional (1D) dislocation with small point defects (dislocation cores) were sparsely observed, as can be seen from the magnified images (Figure 3.17b,c). It is surprising that the crystalline structure is almost preserved even at the merged interface. Here, only few dislocations are expected to be enough to compensate the lattice discontinuity due to the very small misorientation angle and offset of the neighboring lattices. This allows the merging grains to form structurally continuous interface without forming severe structural defects along the boundary. Therefore, the electronic properties across the merged interface are not likely to be affected by such dislocations, resulting in nice atomic stitching. It is noted that such stitching has not been reported so far for merged TMD grains.

Figure 3.17d shows the GBs formed by three merging grains with small misorientation angles; the grains B and C are rotated by 2° and -4° with respect to the grain A, respectively. In this case, two parallel dislocation lines existing in one grain are connected to one dislocation in

another grain at a dislocation core. Accordingly, the dislocation core is slightly larger than that seen in Figure 3.17b,c. This result also demonstrate that the small misorientation angles can give very smooth atomic-scale connection by simply forming a few excess atomic lines to compensate lattice discontinuity and release the possible strain.

Figure 3.17e displays the GB of two merged grains with misorientation angle of 19°, which was grown in pure Ar flow. This large misorientation angle resulted in a continuous defect line along the boundary. In this case, a series of connected 7-5 membered rings was observed along the GB, as shown in the magnified images of Figure 3.17f,g. Moreover, different types of defect structures were widely observed along other large-angle GBs. Figures 3.17h,i show the GBs formed for grains merged with angles of 24° and 10°, respectively. Series of 7-membered ring defects (Figure 3.17h) and 8-membered rings (Figure 3.17i) were observed along the respective GBs. The observation of these linearly arranged defects is consistent with the previous literatures on TMDs that report different types of GBs consisting of a number of irregular atomic rings along the GB.[13–15] Therefore, the low misorientation angle realized by the CVD with a high H_2 concentration produces unique GB structures, which would give much less influence on the physical and chemical properties.

It is difficult to differentiate the role of hydrogen from the effect of low angle misorientation-induced connection observed here, because the WS_2 grains cannot be aligned in the absence of H_2 during the growth. Given that large misorientation angles lead to defects forming along the GBs, the misorientation angle is considered to be a key factor in forming consistent stitching between neighboring WS_2 grains. However, as discussed in Figure 3.2e, the H_2 supplied during CVD growth may also contribute to effective stitching by minimizing (or eliminating) formation of lattice defects.

3.3.5. Influence of GBs on chemical and physical properties of WS_2

There are several methods to visualize GBs in TMD monolayers, such as oxidation[26,54,55] and Joule heating.[56] Most of them utilize the relatively high chemical reactivity of GBs. In order to investigate the chemical stability of GBs, I oxidized the merged WS_2 grains in air at 300 °C for two hours. Figures 3.18a,b show the SEM images of H_2- and Ar-WS_2 grains, respectively, taken after the oxidation. As previously reported,[26] large-angle misoriented Ar-WS_2 grains showed clear visible defects along the GBs after this mild oxidation (Figure 3.18b). On the other hand, the H_2-WS_2 sample (Figure 3.18a) showed difference in oxidation behavior. The boundary between WS_2 grains oriented in the opposite directions (marked with red and blue triangles) exhibited a clear oxidation line similar to those observed for the misaligned grains (Figure 3.18b). This is because a mirror twin boundary is present between these 180°-rotated grains.[11] On the contrary, no visible line was observed for the grains connected with the same orientation (two red triangles). This demonstrates that the low angle misorientation gives consistent stitching that is chemically more stable than other rotated GBs, being consistent with our ADF-STEM observations (see Figure 3.17a-c).

The presence of GBs is also known to deteriorate the carrier transport properties of 2D materials, because they act as a scattering site for carriers while also introduce defect states in

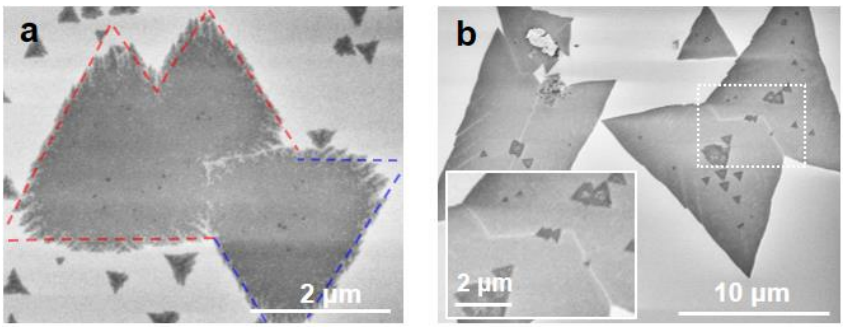

Figure 3.18. SEM images of (a) H_2-WS_2 and (b) Ar-WS_2 grains after oxidation. Red and blue triangles in (a) indicate upward- and downward-oriented aligned grains, respectively. Inset in (b) shows the magnified image of dotted square.

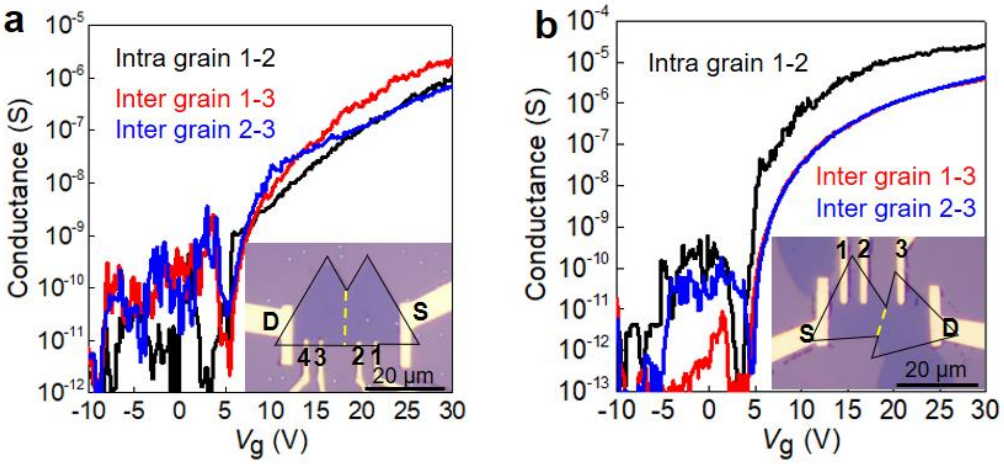

Figure 3.19. Transfer curves of merged H_2-WS_2 (a) and Ar-WS_2 grains (b). Insets show optical micrographs of the measured devices.

the middle of the energy band that trap carriers.[11,13,15] Four-terminal devices were fabricated on merged WS_2 grains with Ti/Au electrodes defined by EB lithography. Insets in Figure 3.19 show optical micrographs of the devices made with H_2-WS_2 (a) and Ar-WS_2 (b) grains with merged angles of 1-2° and ~11°, respectively. In the case of the Ar-WS_2 (Figure 3.19b), inter-grain conductance was clearly lower than the intra-grain conductance. These merged grains may have a GB similar to that shown in Figure 3.17i, as the misorientation angle (~11°) is very close. Thus, a linear chain of the irregular and distorted atomic rings formed along the GB should be responsible for the observed low conductance. In contrast, the H_2-WS_2 grains show almost no conductance degradation across the interface, as shown in Figure 3.19a. This result suggests that the sparsely distributed dislocations (see Figure 3.17a-c) do not significantly affect the carrier transport, which is promising for realization of high performance electronic devices.

3.4. Conclusions

The epitaxial growth of aligned WS_2 on c-plane sapphire substrates is demonstrated using high concentration of hydrogen during the CVD growth. The presence of hydrogen can enhance WS_2-sapphire interaction, likely by exposing an Al-rich surface on the sapphire substrate. This change of the chemical state of the sapphire surface induced by hydrogen was supported by XPS and water contact angle measurements. The DFT calculations suggest the Al-rich surface enhances the coupling between a WS_2 grain and sapphire, which can potentially affect the grain alignment and PL intensity. The H_2-induced alignment is critical for obtaining low misorientation angles between merged WS_2 grains. Inspection of the merging areas by ADF-STEM revealed the unique and smooth reconstructed interface structure with sparsely located 1D dislocations, which can release the small strain between adjacent grains. In stark contrast, the highly misaligned WS_2 grains grown in pure Ar showed linear arrays of distorted atomic rings along the boundaries between merged grains. These boundary structures were found to influence the chemical stability of the WS_2 and the carrier transport, implying that realizing low angle connection by the epitaxial growth of WS_2 is essential to obtain high quality sheets. This study is expected to shed light on the formation of well-stitched grains and at the same time offers an important guiding principle to obtain high-quality TMD films that can be applied to future electronic and optoelectronic devices.

References

(1) Wang, Q. H.; Kalantar-Zadeh, K.; Kis, A.; Coleman, J. N.; Strano, M. S. Electronics and Optoelectronics of Two-Dimensional Transition Metal Dichalcogenides. *Nat. Nanotechnol.* **2012**, *7*, 699–712.

(2) Jariwala, D.; Sangwan, V. K.; Lauhon, L. J.; Marks, T. J.; Hersam, M. C. Emerging Device Applications for Semiconducting Two-Dimensional Transition Metal Dichalcogenides. *ACS Nano* **2014**, *8*, 1102–1120.

(3) Lee, Y.-H.; Zhang, X.-Q.; Zhang, W.; Chang, M.-T.; Lin, C.-T.; Chang, K.-D.; Yu, Y.-C.; Wang, J. T.-W.; Chang, C.-S.; Li, L.-J.; Lin, T.-W. Synthesis of Large-Area MoS_2 Atomic Layers with Chemical Vapor Deposition. *Adv. Mater.* **2012**, *24*, 2320–2325.

(4) Zhan, Y.; Liu, Z.; Najmaei, S.; Ajayan, P. M.; Lou, J. Large-Area Vapor-Phase Growth and Characterization of MoS_2 Atomic Layers on a SiO_2 Substrate. *Small* **2012**, *8*, 966–971.

(5) Lee, Y.-H.; Yu, L.; Wang, H.; Fang, W.; Ling, X.; Shi, Y.; Lin, C.-T.; Huang, J.-K.; Chang, M.-T.; Chang, C.-S.; Dresselhaus, M.; Palacios, T.; Li, L.-J.; Kong, J. Synthesis and Transfer of Single-Layer Transition Metal Disulfides on Diverse Surfaces. *Nano Lett.* **2013**, *13*, 1852–1857.

(6) Wang, S.; Rong, Y.; Fan, Y.; Pacios, M.; Bhaskaran, H.; He, K.; Warner, J. H. Shape Evolution of Monolayer MoS_2 Crystals Grown by Chemical Vapor Deposition. *Chem. Mater.* **2014**, *26*, 6371–6379.

(7) Yun, S. J.; Chae, S. H.; Kim, H.; Park, J. C.; Park, J.-H.; Han, G. H.; Lee, J. S.; Kim, S. M.; Oh, H. M.; Seok, J.; Jeong, M. S.; Kim, K. K.; Lee, Y. H. Synthesis of Centimeter-Scale Monolayer Tungsten Disulfide Film on Gold Foils. *ACS Nano* **2015**, *9*, 5510–5519.

(8) Gao, Y.; Liu, Z.; Sun, D.-M.; Huang, L.; Ma, L.-P.; Yin, L.-C.; Ma, T.; Zhang, Z.; Ma, X.-L.; Peng, L.-M.; Cheng, H.-M.; Ren, W. Large-Area Synthesis of High-Quality and Uniform Monolayer WS_2 on Reusable Au Foils. *Nat. Commun.* **2015**, *6*, 8569.

(9) Kang, K.; Xie, S.; Huang, L.; Han, Y.; Huang, P. Y.; Mak, K. F.; Kim, C.-J.; Muller, D.; Park, J. High-Mobility Three-Atom-Thick Semiconducting Films with Wafer-Scale Homogeneity. *Nature* **2015**, *520*, 656–660.

(10) Xu, Z.-Q.; Zhang, Y.; Lin, S.; Zheng, C.; Zhong, Y. L.; Xia, X.; Li, Z.; Sophia, P. J.; Fuhrer, M. S.; Cheng, Y.-B.; Bao, Q. Synthesis and Transfer of Large-Area Monolayer WS_2 Crystals: Moving Toward the Recyclable Use of Sapphire Substrates. *ACS Nano* **2015**, *9*, 6178–6187.

(11) van der Zande, A. M.; Huang, P. Y.; Chenet, D. A.; Berkelbach, T. C.; You, Y.; Lee, G.-H.; Heinz, T. F.; Reichman, D. R.; Muller, D. A.; Hone, J. C. Grains and Grain Boundaries in Highly Crystalline Monolayer Molybdenum Disulphide. *Nat. Mater.* **2013**, *12*, 554–561.

(12) Najmaei, S.; Liu, Z.; Zhou, W.; Zou, X.; Shi, G.; Lei, S.; Yakobson, B. I.; Idrobo, J.-C.; Ajayan, P. M.; Lou, J. Vapour Phase Growth and Grain Boundary Structure of Molybdenum Disulphide Atomic Layers. *Nat. Mater.* **2013**, *12*, 754–759.

(13) Zhou, W.; Zou, X.; Najmaei, S.; Liu, Z.; Shi, Y.; Kong, J.; Lou, J.; Ajayan, P. M.; Yakobson, B. I.; Idrobo, J.-C. Intrinsic Structural Defects in Monolayer Molybdenum Disulfide. *Nano Lett.* **2013**, *13*, 2615–2622.

(14) Azizi, A.; Zou, X.; Ercius, P.; Zhang, Z.; Elías, A. L.; Perea-López, N.; Stone, G.; Terrones, M.; Yakobson, B. I.; Alem, N. Dislocation Motion and Grain Boundary Migration in Two-Dimensional Tungsten Disulphide. *Nat. Commun.* **2014**, *5*, 4867.

(15) Ly, T. H.; Perello, D. J.; Zhao, J.; Deng, Q.; Kim, H.; Han, G. H.; Chae, S. H.; Jeong, H. Y.; Lee, Y. H. Misorientation-Angle-Dependent Electrical Transport across

Molybdenum Disulfide Grain Boundaries. *Nat. Commun.* **2016**, *7*, 10426.

(16) Dumcenco, D.; Ovchinnikov, D.; Marinov, K.; Lazić, P.; Gibertini, M.; Marzari, N.; Sanchez, O. L.; Kung, Y.-C.; Krasnozhon, D.; Chen, M.-W.; Bertolazzi, S.; Gillet, P.; Fontcuberta i Morral, A.; Radenovic, A.; Kis, A. Large-Area Epitaxial Monolayer MoS_2. *ACS Nano* **2015**, *9*, 4611–4620.

(17) Ago, H.; Endo, H.; Solís-Fernández, P.; Takizawa, R.; Ohta, Y.; Fujita, Y.; Yamamoto, K.; Tsuji, M. Controlled van Der Waals Epitaxy of Monolayer MoS_2 Triangular Domains on Graphene. *ACS Appl. Mater. Interfaces* **2015**, *7*, 5265–5273.

(18) Ago, H.; Fukamachi, S.; Endo, H.; Solís-Fernández, P.; Mohamad Yunus, R.; Uchida, Y.; Panchal, V.; Kazakova, O.; Tsuji, M. Visualization of Grain Structure and Boundaries of Polycrystalline Graphene and Two-Dimensional Materials by Epitaxial Growth of Transition Metal Dichalcogenides. *ACS Nano* **2016**, *10*, 3233–3240.

(19) Okada, M.; Sawazaki, T.; Watanabe, K.; Taniguch, T.; Hibino, H.; Shinohara, H.; Kitaura, R. Direct Chemical Vapor Deposition Growth of WS_2 Atomic Layers on Hexagonal Boron Nitride. *ACS Nano* **2014**, *8*, 8273–8277.

(20) Yu, H.; Yang, Z.; Du, L.; Zhang, J.; Shi, J.; Chen, W.; Chen, P.; Liao, M.; Zhao, J.; Meng, J.; Wang, G.; Zhu, J.; Yang, R.; Shi, D.; Gu, L.; Zhang, G. Precisely Aligned Monolayer MoS_2 Epitaxially Grown on H-BN Basal Plane. *Small* **2017**, *13*, 1603005.

(21) Gutiérrez, H. R.; Perea-López, N.; Elías, A. L.; Berkdemir, A.; Wang, B.; Lv, R.; López-Urías, F.; Crespi, V. H.; Terrones, H.; Terrones, M. Extraordinary Room-Temperature Photoluminescence in Triangular WS_2 Monolayers. *Nano Lett.* **2013**, *13*, 3447–3454.

(22) Yuan, L.; Huang, L. Exciton Dynamics and Annihilation in WS_2 2D Semiconductors. *Nanoscale* **2015**, *7*, 7402–7408.

(23) Kormányos, A.; Zólyomi, V.; Drummond, N. D.; Burkard, G. Spin-Orbit Coupling, Quantum Dots, and Qubits in Monolayer Transition Metal Dichalcogenides. *Phys. Rev.*

X **2014**, *4*, 011034.

(24) Liu, L.; Kumar, S. B.; Ouyang, Y.; Guo, J. Performance Limits of Monolayer Transition Metal Dichalcogenide Transistors. *IEEE Trans. Electron Devices* **2011**, *58*, 3042–3047.

(25) Rong, Y.; Fan, Y.; Koh, A. L.; Robertson, A. W.; He, K.; Wang, S.; Tan, H.; Sinclair, R.; Warner, J. H. Controlling Sulphur Precursor Addition for Large Single Crystal Domains of WS_2. *Nanoscale* **2014**, *6*, 12096–12103.

(26) Zhang, Y.; Zhang, Y.; Ji, Q.; Ju, J.; Yuan, H.; Shi, J.; Gao, T.; Ma, D.; Liu, M.; Chen, Y.; Song, X.; Hwang, H. Y.; Cui, Y.; Liu, Z. Controlled Growth of High-Quality Monolayer WS_2 Layers on Sapphire and Imaging Its Grain Boundary. *ACS Nano* **2013**, *7*, 8963–8971.

(27) McCreary, K. M.; Hanbicki, A. T.; Jernigan, G. G.; Culbertson, J. C.; Jonker, B. T. Synthesis of Large-Area WS_2 Monolayers with Exceptional Photoluminescence. *Sci. Rep.* **2016**, *6*, 19159.

(28) Gong, Y.; Ye, G.; Lei, S.; Shi, G.; He, Y.; Lin, J.; Zhang, X.; Vajtai, R.; Pantelides, S. T.; Zhou, W.; Li, B.; Ajayan, P. M. Synthesis of Millimeter-Scale Transition Metal Dichalcogenides Single Crystals. *Adv. Funct. Mater.* **2016**, *26*, 2009–2015.

(29) Sheng, Y.; Tan, H.; Wang, X.; Warner, J. H. Hydrogen Addition for Centimeter-Sized Monolayer Tungsten Disulfide Continuous Films by Ambient Pressure Chemical Vapor Deposition. *Chem. Mater.* **2017**, *29*, 4904-4911 .

(30) Perdew, J. P.; Burke, K.; Ernzerhof, M. Generalized Gradient Approximation Made Simple. *Phys. Rev. Lett.* **1996**, *77*, 3865–3868.

(31) Lee, K.; Murray, É. D.; Kong, L.; Lundqvist, B. I.; Langreth, D. C. A Higher-Accuracy van Der Waals Density Functional. *Phys. Rev. B* **2010**, *82*, 081101 (R).

(32) Cooper, V. R. Van Der Waals Density Functional: An Appropriate Exchange Functional. *Phys. Rev. B* **2010**, *81*, 161104.

(33) Morikawa, Y.; Iwata, K.; Terakura, K. Theoretical Study of Hydrogenation Process of Formate on Clean and Zn Deposited Cu(111) Surfaces. *Appl. Surf. Sci.* **2001**, *169*, 11–15.

(34) Vanderbilt, D. Soft Self-Consistent Pseudopotentials in a Generalized Eigenvalue Formalism. *Phys. Rev. B* **1990**, *41*, 7892–7895.

(35) Otani, M.; Sugino, O. First-Principles Calculations of Charged Surfaces and Interfaces: A Plane-Wave Nonrepeated Slab Approach. *Phys. Rev. B* **2006**, *73*, 115407.

(36) Gurarslan, A.; Yu, Y.; Su, L.; Yu, Y.; Suarez, F.; Yao, S.; Zhu, Y.; Ozturk, M.; Zhang, Y.; Cao, L. Surface-Energy-Assisted Perfect Transfer of Centimeter-Scale Monolayer and Few-Layer MoS_2 Films onto Arbitrary Substrates. *ACS Nano* **2014**, *8*, 11522–11528.

(37) Wu, S.; Huang, C.; Aivazian, G.; Ross, J. S.; Cobden, D. H.; Xu, X. Vapor–Solid Growth of High Optical Quality MoS_2 Monolayers with Near-Unity Valley Polarization. *ACS Nano* **2013**, *7*, 2768–2772.

(38) Schutte, W. J.; De Boer, J. L.; Jellinek, F. Crystal Structures of Tungsten Disulfide and Diselenide. *J. Solid State Chem.* **1987**, *70*, 207–209.

(39) Dobrovinskaya, E. R.; Lytvynov, L. A.; Pishchik, V. Properties of Sapphire. In *Sapphire*; Micro- and Opto-Electronic Materials, Structures, and Systems; Springer US, 2009; pp 55–176.

(40) Robertson, A. W.; Lin, Y.-C.; Wang, S.; Sawada, H.; Allen, C. S.; Chen, Q.; Lee, S.; Lee, G.-D.; Lee, J.; Han, S.; Yoon, E.; Kirkland, A. I.; Kim, H.; Suenaga, K.; Warner, J. H. Atomic Structure and Spectroscopy of Single Metal (Cr, V) Substitutional Dopants in Monolayer MoS_2. *ACS Nano* **2016**, *10*, 10227–10236.

(41) Aljarb, A.; Cao, Z.; Tang, H.-L.; Huang, J.-K.; Li, M.; Hu, W.; Cavallo, L.; Li, L.-J. Substrate Lattice-Guided Seed Formation Controls the Orientation of 2D Transition-Metal Dichalcogenides. *ACS Nano* **2017**, *11*, 9215-9222.

(42) Suenaga, K.; Ji, H. G.; Lin, Y.-C.; Vincent, T.; Maruyama, M.; Aji, A. S.; Shiratsuchi, Y.; Ding, D.; Kawahara, K.; Okada, S.; Panchal, V.; Kazakova, O.; Hibino, H.; Suenaga, K.; Ago, H. Surface-Mediated Aligned Growth of Monolayer MoS_2 and In-Plane Heterostructures with Graphene on Sapphire. *ACS Nano* **2018**, *12*, 10032–10044.

(43) Peimyoo, N.; Shang, J.; Cong, C.; Shen, X.; Wu, X.; Yeow, E. K. L.; Yu, T. Nonblinking, Intense Two-Dimensional Light Emitter: Monolayer WS_2 Triangles. *ACS Nano* **2013**, *7*, 10985–10994.

(44) Gao, J.; Li, B.; Tan, J.; Chow, P.; Lu, T.-M.; Koratkar, N. Aging of Transition Metal Dichalcogenide Monolayers. *ACS Nano* **2016**, *10*, 2628–2635.

(45) Han, H.-V.; Lu, A.-Y.; Lu, L.-S.; Huang, J.-K.; Li, H.; Hsu, C.-L.; Lin, Y.-C.; Chiu, M.-H.; Suenaga, K.; Chu, C.-W.; Kuo, H.-C.; Chang, W.-H.; Li, L.-J.; Shi, Y. Photoluminescence Enhancement and Structure Repairing of Monolayer $MoSe_2$ by Hydrohalic Acid Treatment. *ACS Nano* **2016**, *10*, 1454–1461.

(46) Wang, K.; Huang, B.; Tian, M.; Ceballos, F.; Lin, M.-W.; Mahjouri-Samani, M.; Boulesbaa, A.; Puretzky, A. A.; Rouleau, C. M.; Yoon, M.; Zhao, H.; Xiao, K.; Duscher, G.; Geohegan, D. B. Interlayer Coupling in Twisted WSe_2/WS_2 Bilayer Heterostructures Revealed by Optical Spectroscopy. *ACS Nano* **2016**, *10*, 6612–6622.

(47) Nayak, P. K.; Horbatenko, Y.; Ahn, S.; Kim, G.; Lee, J.-U.; Ma, K. Y.; Jang, A.-R.; Lim, H.; Kim, D.; Ryu, S.; Cheong, H.; Park, N.; Shin, H. S. Probing Evolution of Twist-Angle-Dependent Interlayer Excitons in $MoSe_2/WSe_2$ van Der Waals Heterostructures. *ACS Nano* **2017**, *11*, 4041–4050.

(48) Mouri, S.; Miyauchi, Y.; Matsuda, K. Tunable Photoluminescence of Monolayer MoS_2 via Chemical Doping. *Nano Lett.* **2013**, *13*, 5944–5948.

(49) McCreary, K. M.; Hanbicki, A. T.; Singh, S.; Kawakami, R. K.; Jernigan, G. G.; Ishigami, M.; Ng, A.; Brintlinger, T. H.; Stroud, R. M.; Jonker, B. T. The Effect of Preparation

Conditions on Raman and Photoluminescence of Monolayer WS_2. *Sci. Rep.* **2016**, *6*, 35154.

(50) Ago, H.; Tanaka, I.; Tsuji, M.; Ikeda, K.; Mizuno, S. Hole Doping to Aligned Single-Walled Carbon Nanotubes from Sapphire Substrate Induced by Heat Treatment. *J. Phys. Chem. C* **2008**, *112*, 18350–18354.

(51) Berkdemir, A.; Gutiérrez, H. R.; Botello-Méndez, A. R.; Perea-López, N.; Elías, A. L.; Chia, C.-I.; Wang, B.; Crespi, V. H.; López-Urías, F.; Charlier, J.-C.; Terrones, H.; Terrones, M. Identification of Individual and Few Layers of WS_2 Using Raman Spectroscopy. *Sci. Rep.* **2013**, *3*, 1755.

(52) Tsuda, M.; Watanabe, K.; Kamiyama, S.; Amano, H.; Akasaki, I.; Liu, R.; Bell, A.; A. Ponce, F. Mechanism of H_2 Pre-Annealing on the Growth of GaN on Sapphire by MOVPE. *Appl. Surf. Sci.* **2003**, *216*, 585–589.

(53) Chen, L.; Liu, B.; Ge, M.; Ma, Y.; Abbas, A. N.; Zhou, C. Step-Edge-Guided Nucleation and Growth of Aligned WSe_2 on Sapphire via a Layer-over-Layer Growth Mode. *ACS Nano* **2015**, *9*, 8368–8375.

(54) Ly, T. H.; Chiu, M.-H.; Li, M.-Y.; Zhao, J.; Perello, D. J.; Cichocka, M. O.; Oh, H. M.; Chae, S. H.; Jeong, H. Y.; Yao, F.; Li, L.-J.; Lee, Y. H. Observing Grain Boundaries in CVD-Grown Monolayer Transition Metal Dichalcogenides. *ACS Nano* **2014**, *8*, 11401–11408.

(55) Rong, Y.; He, K.; Pacios, M.; Robertson, A. W.; Bhaskaran, H.; Warner, J. H. Controlled Preferential Oxidation of Grain Boundaries in Monolayer Tungsten Disulfide for Direct Optical Imaging. *ACS Nano* **2015**, *9*, 3695–3703.

(56) Rong, Y.; Sheng, Y.; Pacios, M.; Wang, X.; He, Z.; Bhaskaran, H.; Warner, J. H. Electroluminescence Dynamics across Grain Boundary Regions of Monolayer Tungsten Disulfide. *ACS Nano* **2016**, *10*, 1093–1100.

Chapter 4

Influence of van der Waals Interaction on Growth and Physical Properties of Epitaxially Aligned WS_2

Abstract

In the previous chapter, the epitaxial growth of high quality WS_2 on c-plane sapphire substrate was demonstrated. Having similar hexagonal crystal structure with many TMDs, c-plane sapphire is commonly utilized as a growth substrate in CVD synthesis. Due to the similarity of crystal structure, c-sapphire substrate is expected to influence the growth of TMDs while few studies have been reported about this. Thus, in this chapter, I demonstrate that higher strain is induced in the epitaxially grown WS_2 grains via van der Waals interaction with sapphire as compared with misaligned WS_2 grains. In addition, this strain was found to enhance overlayer deposition on monolayer WS_2, while multilayer growth was not observed in non-epitaxial WS_2. PL of the epitaxially grown WS_2 grains was reduced reflecting effective van der Waals interaction with sapphire. Moreover, low-temperature PL measurement revealed strong influence of the c-plane sapphire surface on the optical property of WS_2. DFT calculation supports that the aligned WS_2 grains are more strongly bound to the sapphire surface, as compared with misaligned WS_2.

4.1. Introduction

The CVD growth of monolayer TMDs has been widely studied using various kinds of precursors, such as metal oxide and metalorganic gas, and different carrier gases, such as pure Ar and the mixed gas with H_2 or O_2, in order to increase the grain size and improve the film uniformity.[1–8] Also, different types of substrates have been studied, including insulators (SiO_2, sapphire) and metal substrates (Au and Ni foils).[2,9–12] Among them, c-plane (0001) sapphire which has a hexagonal surface crystal structure similar to those of WS_2 and MoS_2 is one of the most suitable template. Epitaxial growth of WS_2 was achieved on the sapphire substrate by flowing hydrogen during the CVD growth.[8] This epitaxial growth on sapphire is expected to give highly crystallized TMD films as compared with polycrystalline films consisting of randomly oriented grains that are widely formed on the SiO_2 substrate, because stitching of the merged grains can occur for the aligned TMD grains.[13–19] However, it is not clearly understood how the sapphire surface affects physical properties of the aligned TMDs.[20]

Therefore, in this work, I have investigated physical properties of the epitaxially aligned WS_2 grains by comparing with randomly oriented grains which are formed on the same c-plane sapphire substrate. It was found that the PL from aligned WS_2 grains is weaker than that of misaligned grains. This result is interpreted by substrate-induced higher strain in the aligned WS_2 due to effective van der Waals interaction between WS_2 and the sapphire surface. Selective overlayer deposition of multilayer WS_2 was also observed on the aligned grains, reflecting the induced strain. DFT calculation was performed to investigate the interaction between WS_2 grains and sapphire. Low-temperature PL revealed significant difference in the optical properties after detaching from the sapphire substrate. Carrier transport measurements were also performed to further understand the crystallinity of aligned and misaligned WS_2 grains.

4.2. Experimental method

4.2.1. CVD growth of WS_2

WS_2 was synthesized from WO_3 (99.998%, Alfa Aesar) and sulfur (99.999%, Mitsuwa Chemicals) precursors by ambient pressure CVD method. C-plane sapphire (Kyocera) with a low miscut angle (< 0.2˚) was used as substrate which was cleaned by sonicating in acetone and isopropyl alcohol prior to the CVD. For the CVD growth, a three-zone tubular furnace with a quartz tube (outer diameter is 26 mm) and a heating belt were used, as illustrated in Figure 4.1. Different from Figure 3.1, an additional inner quartz tube was used for more efficient reaction between precursors on growth substrate. During the CVD reaction, 500 ccm of pure Ar gas (99.999%) was flowed as a carrier gas. The temperatures of sulfur, WO_3, and sapphire substrate were set at 160 ˚C, 1080 ˚C, and 970 ˚C, respectively. After 30 min reaction, the sample was cooled down naturally inside the furnace while flowing Ar gas.

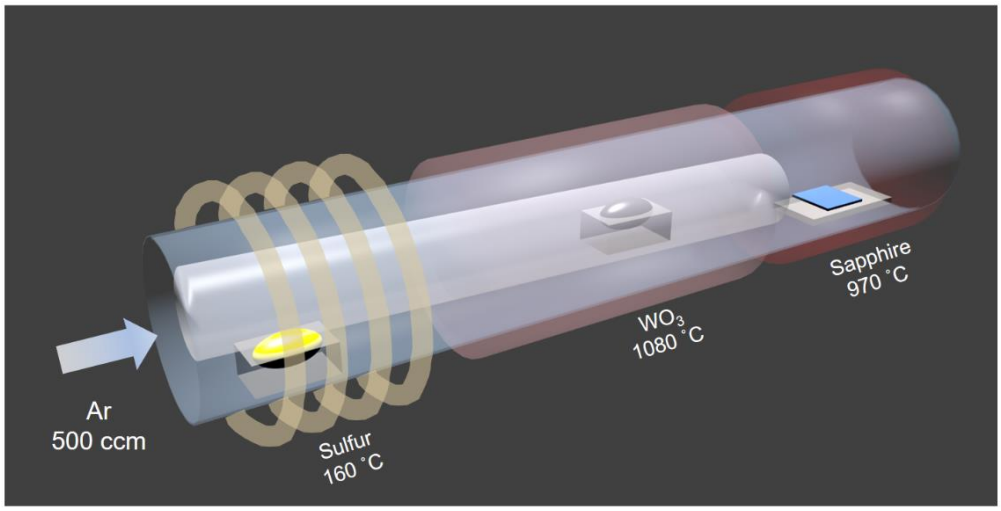

Figure 4.1. CVD setup used for growth of WS_2. A three-zone tubular furnace was used for heating WO_3 and sapphire heating with a ribbon heater for sulfur heating. Different from the set up in Figure 3.1, additional inner quartz tube is used for more efficient reaction between precursors on growth substrate.

4.2.2. Characterization methods

As-grown WS_2 was characterized by optical microscope (OM, Nikon Eclipse ME600) and AFM (Bruker Nanoscope V). To measure room-temperature PL and Raman spectra, a confocal Raman spectroscope (Tokyo Instrument Nanofinder30) with 473 nm laser excitation was used. For measuring PL spectra at low temperatures, Nanophoton Ramantouch was used with a Helium cryostat (Janis ST-500UC) using 532 nm laser excitation.

4.2.3. DFT calculations

Theoretical calculations were performed using DFT with the generalized gradient approximation (GGA-PBE)[21] and van der Waals corrections (vdW-DF2-C09)[22,23] implemented in the STATE package.[24] Vanderbilt ultrasoft pseudopotentials were used to describe electron-ion interactions.[25] Valence wave function and deficit charge density were expanded in terms of plane-wave basis with cutoff energy of 25 and 225 Ry, respectively. Surfaces of Al_2O_3 were simulated by a repeated slab model of α-Al_2O_3 thin films with 8 atomic layers with Al-terminated Al_2O_3 surfaces. To calculate the adsorption energy of a WS_2 grain on the Al_2O_3 slab, the 4×4 lateral cell was adopted to exclude the interaction with the periodic images of WS_2 grain. The triangular WS_2 grain with a lateral length of 1.3 nm was constructed with 15 W and 36 S atoms. The geometric structures were optimized until the force acting on atoms was less than 0.01 Ry/Å under the fixed lattice parameter.

4.2.4. Device fabrication and measurement

For fabricating WS_2-FETs, WS_2 grains grown on sapphire was transferred onto SiO_2/Si substrate using polystyrene and KOH.[26] Then, electrode patterns were defined by a photolithography process, followed by deposition of Ni (5 nm)/Au (25 nm) electrodes using an EB evaporator (Kennix KB-750) and lift-off process. Prior to the measurement, the device was annealed in Ar at 200 ˚C for 2h to remove polymer residue. The devices were measured with a semiconductor parameter analyzer (Keysight Technologies B1500A) in vacuum (~10^{-4} Pa) at room temperature.

4.3. Results and discussion

4.3.1. Aligned and misaligned WS_2 grains on c-plane sapphire

Figure 4.2a,b shows optical micrographs of as-grown WS_2 on c-plane sapphire. It was found that there exist two types of triangular-shaped WS_2 grains together on the single sapphire substrate. One is aligned grains whose side edge is parallel to the $[1\bar{1}00]$ axis of the underlying sapphire substrate (highlighted by red triangles in Figure 4.2a,b), indicating the epitaxially grown WS_2 grains. Another is randomly oriented (misaligned) grains highlighted by green triangles in Figure 4.2a,b. Interestingly, I found that overlayer deposition of multilayer WS_2 occurs preferentially on the aligned WS_2 grains; aligned grains showed many multilayer grains on their surface. On the other hand, the misaligned grains were almost free from multilayer deposition except for a small multilayer triangle only at the center of monolayer grain which acted as a nucleation site. Such difference is clearly seen in the corresponding AFM image

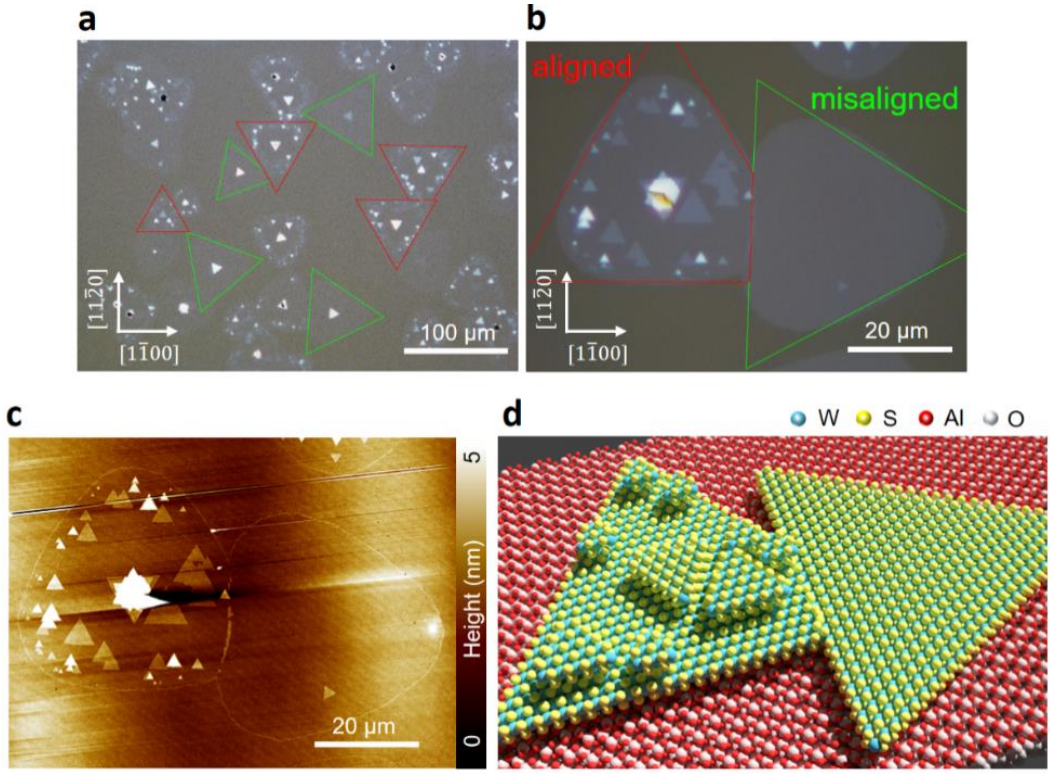

Figure 4.2. (a,b) Optical images of as-grown WS_2 grains on sapphire substrate with low (a) and high (b) magnifications. The crystalline axes of sapphire are shown by white arrows. (c,d) AFM height image and schematic of the WS_2 grains shown in (b,c). The overlayer deposition occurs only on the aligned grain (left grain), while the misaligned grain is free from multilayer (right grain).

(Figure 4.2c). This AFM image signifies that many multilayer grains formed on the aligned WS_2 are oriented in the same direction with the monolayer grain underneath. Figure 4.2d displays the atomic model of the aligned (left) and misaligned (right) WS_2 grains formed on sapphire where the former has multilayer grains on its surface. To confirm this result, I performed more than 20 CVD runs. As shown in Figure 4.3, in most of the CVD runs, the same tendency was observed; aligned WS_2 grains have multilayer grains on their surfaces.

It is speculated that van der Waals interaction between WS_2 and sapphire is stronger for the aligned WS_2 than the randomly oriented WS_2 grains.[8,27,28] This strong interaction can induce large strain in the aligned WS_2, because the mismatch of the

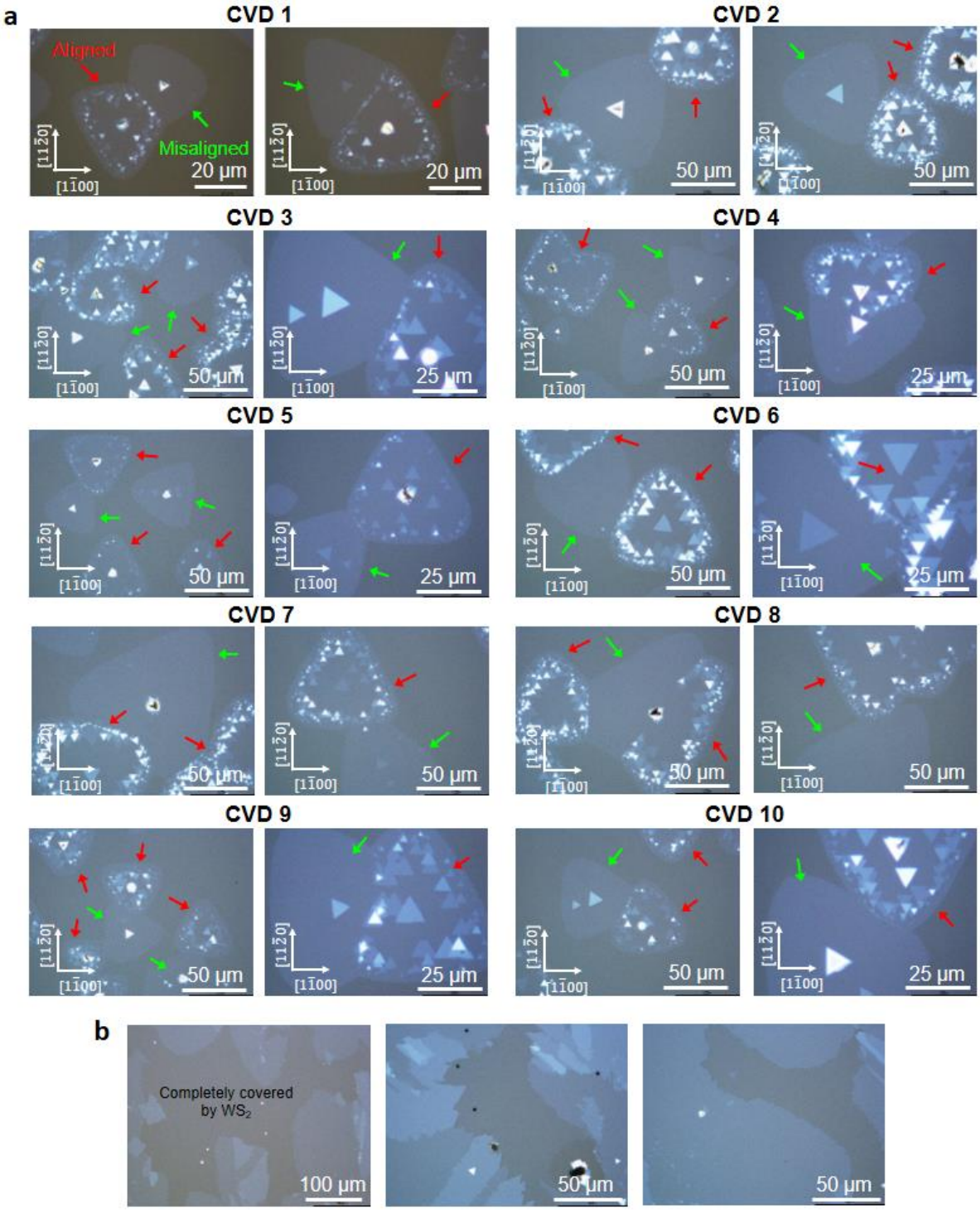

Figure 4.3. Optical micrographs of as-grown WS_2 grains on sapphire substrates. (a) The preferential overlayer deposition was observed on the aligned grains. (b) In a few cases, the sapphire surface was fully covered with WS_2 together with large multilayer grains.

	Growth parameters				Growth mode	
	Gas flow rate	WO_3	S	sapphire	Epitaxially aligned grains	Preferential multilayer growth
A	300 ccm	1080 °C	160 °C	970 °C	X	X
B	500 ccm				O	O
C	700 ccm				O	O
D	500 ccm	1075 °C	160 °C	770 °C	X	X
E				870 °C	X	X
F				970 °C	O	X
G				1070 °C	O	O

Table 4.1. CVD conditions used for sample (A) ~ (G) shown in Figure 4.4 and the observed growth modes.

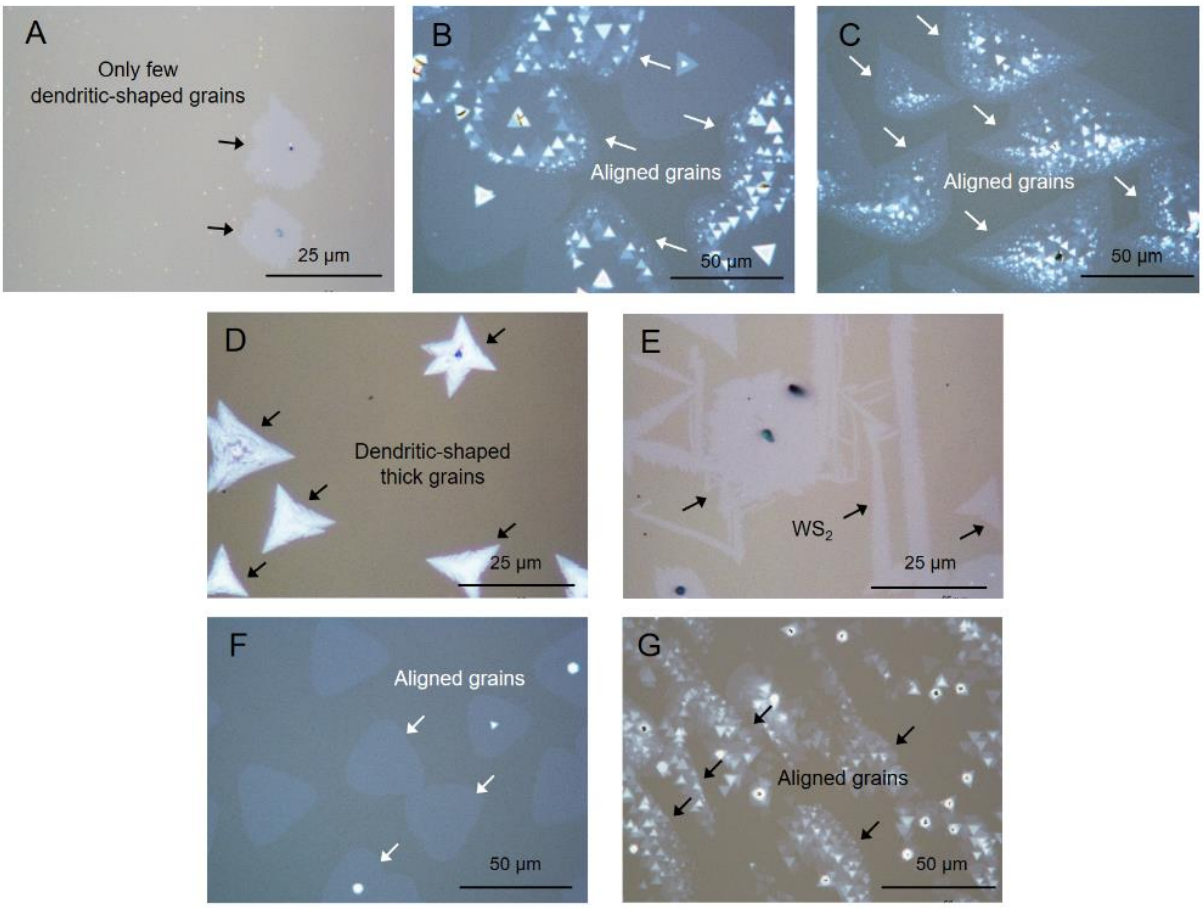

Figure 4.4. Optical images of as-grown WS_2 on c-plane sapphire synthesized using the growth conditions shown in Table 4.1.

lattice constants of WS_2 and sapphire is relatively large (4.76 Å for sapphire and 3.15 Å for WS_2).[29–32] This strain could induce distortion in crystal structure of WS_2, resulting in local fluctuation of electronic potential of WS_2.[33] Such specific electrical and/or geometrical distortion is expected to assist the nucleation of upper WS_2 grains because TMDs preferentially nucleates from the disordered sites.[20,34]

Influence of other CVD parameters on the growth behavior was also investigated. The results are summarized in Table 4.1 and Figure 4.4. As the gas flow rate was increased from 300 ccm to 700 ccm, the percentage of aligned grains increased, and the density of multilayer grains also increased. The higher flow rate can increase the supply rate of WO_3 and S feedstock, thus giving a larger amount of multilayer grains. At the same time, the increase of the S can improve the WS_2 orientation, as the higher S supply is known to give epitaxially aligned MoS_2.[35] I also investigated the effect of the temperature of sapphire substrate by changing it from 770 °C to 1070 °C (see Table 4.1). With the increase of the substrate temperature, the lateral growth was more promoted, reflecting the enhanced surface diffusion of the WS_2 intermediate species.

Generally, monolayer WS_2 exhibits strong PL reflecting its direct band gap. It is well acknowledged that the PL is sensitive to strain, defects, and carrier concentration. Figure 4.5a-c indicates the PL mapping images (PL intensity, full-width at half maximum (FWHM), and peak position) taken at the merged grains shown in Figure 4.2b,c. The PL spectra collected at the marked positions in Figure 4.5a are also shown in Figure 4.5d. Clear differences were observed between the aligned and the misaligned WS_2 grains. Compared with the misaligned WS_2 grain, the aligned grain showed lower PL intensity (Figure 4.5a), broader linewidth (Figure 4.5b), and slight red-shift (Figure 4.5c). As seen in the original PL spectra presented in Figure 4.5d, the PL intensity is clearly reduced in the aligned grain. As the monolayer areas was

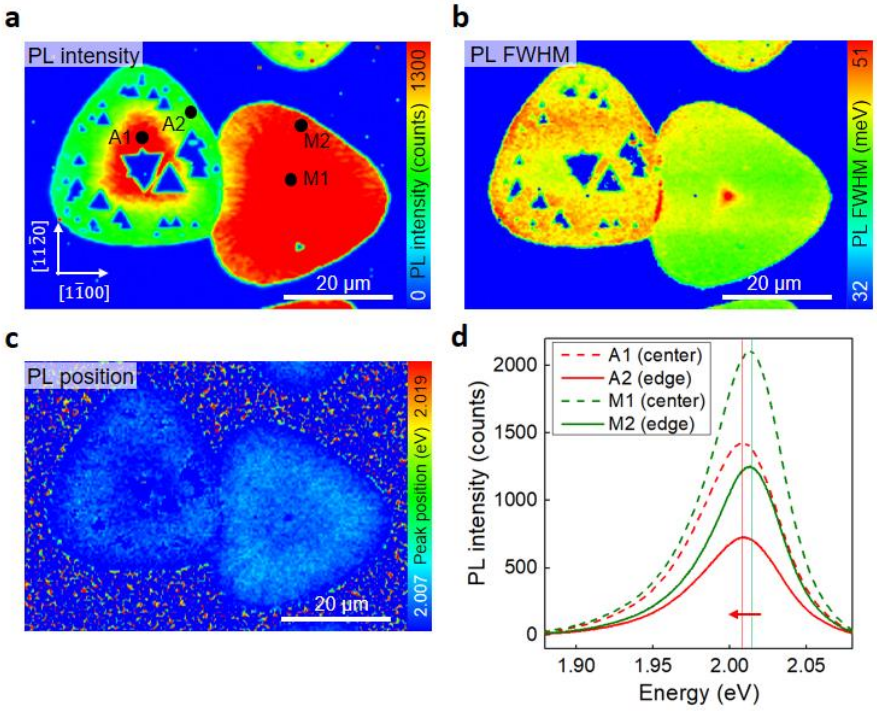

Figure 4.5. PL mapping images of the intensity (a), FWHM (b), and peak position (c). (d) PL spectra from the marked points in (a). A1, A2 are from the aligned grain and M1, M2 are from the misaligned grain.

measured in the aligned grain, the reduced PL intensity is not due to the formation of multilayer grains. The PL quenching occurs via non-radiative relaxation process of excitons that is formed by the photo-excitation. There are two possibilities in the reduced PL seen in the aligned WS_2 grains, low crystallinity and strong interaction with substrate (in this case sapphire).[36–39] As will be discussed later, the interaction with substrate is the main origin of the reduced PL. The different PL FWHM and peak positions (Figure 4.5b,c) can be also explained by the interaction with the sapphire surface, because the spectral weight of neutral excitons and charged trions modifies a PL spectrum of WS_2.[17,33,40,41]

To avoid possible influence from multilayer growth, I synthesized monolayer, aligned WS_2 grains by lowering WO_3 temperature during the CVD to reduce the supply of

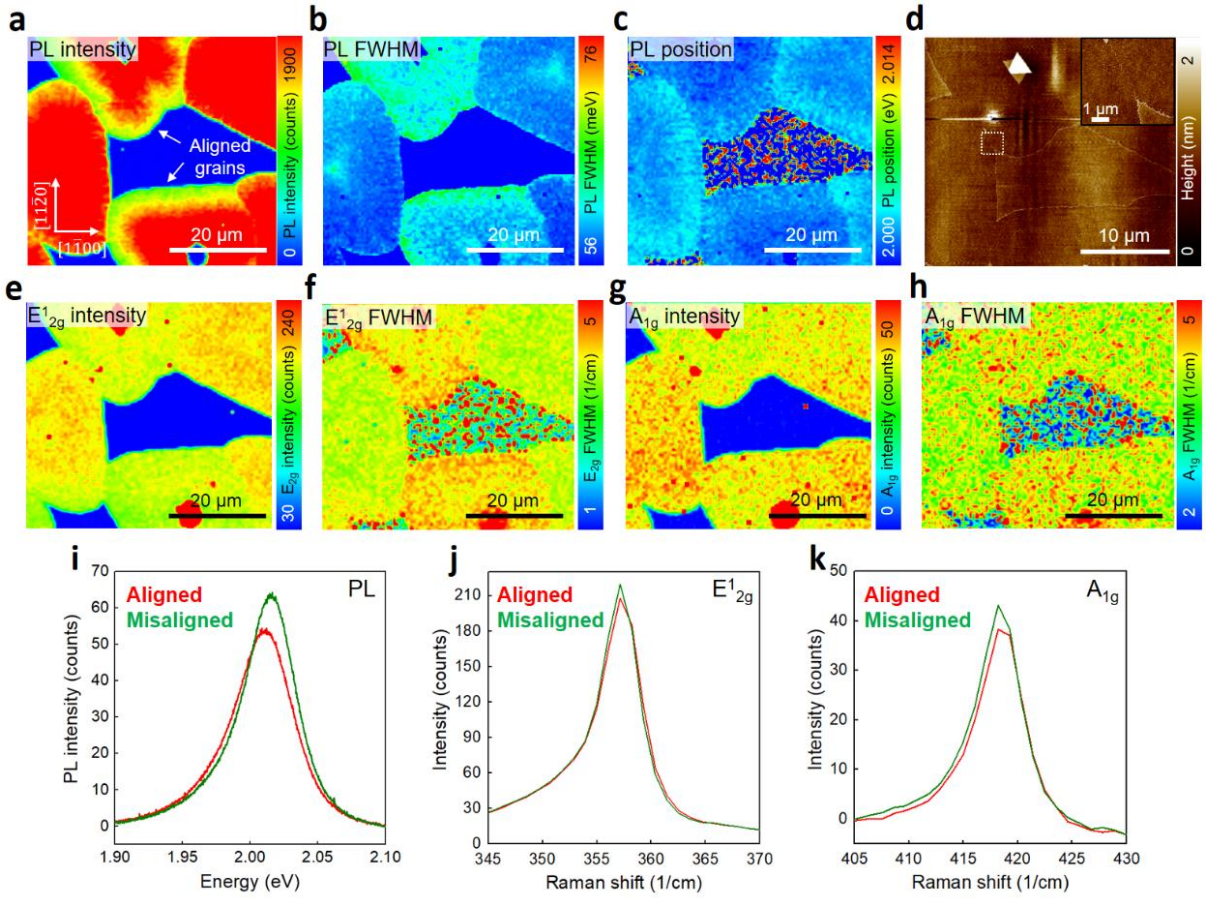

Figure 4.6. PL mapping images of the peak intensity (a), FWHM (b), and position (c) of monolayer WS_2 grains. (d) AFM height image. The inset shows a magnified image of the marked area. Raman E^1_{2g} mappings with intensity (e) and FWHM (f), and A_{1g} mappings with intensity (g) and FWHM (h). (i) PL, (j) E^1_{2g}, and (k) A_{1g} spectra taken from as-grown aligned and misaligned grains.

feedstock. The absence of multilayer was confirmed by AFM and Raman measurements (Figure 4.6). Figure 4.7 shows the detailed analysis of the aligned and misaligned, monolayer WS_2 grains. Here, a misaligned WS_2 grain rotated by ~45° with respect to [1$\bar{1}$00] axis of sapphire was chosen as a representative of misaligned grains in addition to the aligned grain (Figure 4.7a). The PL peak position and linewidth of each WS_2 grain measured at more than 30 points are compared in Figure 4.7b. It was confirmed that the PL linewidth is broader for the aligned grains (58.1±1.4 meV, red plots) than the misaligned ones (54.5±1.1 meV, green plots). The

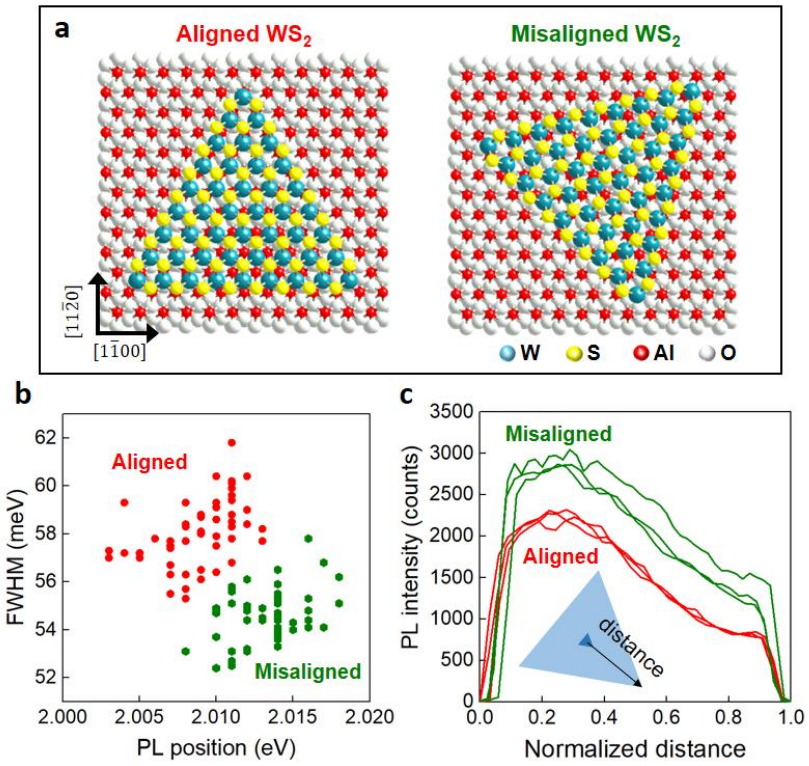

Figure 4.7. (a) Atomic models of aligned (0°) and misaligned WS_2 (~45°) grains on c-plane sapphire. (b) Distributions of PL FWHM and peak position of as-grown WS_2 grains. (c) Distribution of the PL intensity along the line shown in the inset. The x-axis is the normalized distance from the nucleation center, as illustrate in the inset.

red shift of the peak position was also seen from the misaligned grains (2.013±0.002 eV) to the aligned grains (2.009±0.003 eV). According to the previous literatures, this shift (~4 meV) corresponds to 0.3~0.5% of tensile strain introduced in the aligned grain.[42,43] Figure 4.7c indicates the PL intensity change measured from the center to the edge of WS_2 grains. Again, the PL intensity of the aligned grain is weaker than the misaligned grain. Also, the Raman intensity of the aligned WS_2 grain was weaker than misaligned grain (Figure 4.6j,k). The PL intensity gradually decreases from the center to the edge of the grains. In the high temperature atmosphere, the sapphire surface becomes more reactive due to heat-induced cleaning and surface reconstruction.[28] The sapphire surface below the edge area of a WS_2 grain is exposed to the high temperature

Ar flow for longer time, while the sapphire below the central area of WS_2 grain is protected by WS_2. Thus, it is considered that the sapphire surface under the edge area of the WS_2 grain interacts more strongly with WS_2 compared with central grain area, giving reduced PL intensity toward the edges.

4.3.2. DFT calculations

In order to understand the experimental observations, DFT calculation was performed using the model of a triangular WS_2 grain adsorbed on Al-terminated, c-plane sapphire surface. Figure 4.8a,b shows the calculation model of an epitaxially aligned WS_2 grain (consisting of 15 W atoms and 36 S atoms with 1.3 nm lateral size) on the sapphire surface. Two configurations, 0° (aligned) and 20° (misaligned), with respect to the $[1\bar{1}00]$ axis of the sapphire surface were studied. Figure 4.8c compares the optimized WS_2-sapphire distance and the calculated adsorption energy. It was found that the aligned WS_2 grain has a relatively shorter distance (1.65 Å) than the misaligned grain

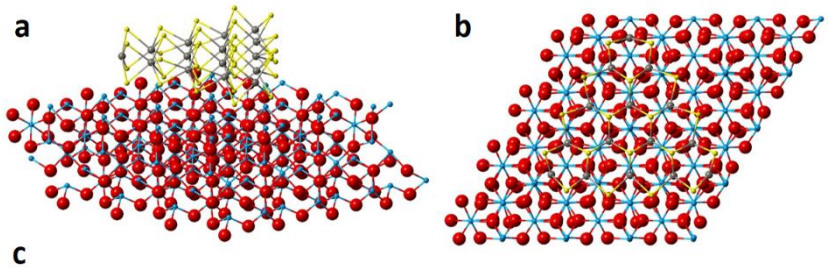

c

Grain orientation	WS_2-sapphire distance (Å)	Adsorption energy (eV/per WS_2 grain)
Aligned (0°)	1.65	+ 1.18
Misaligned (20°)	1.78	0

Figure 4.8. DFT calculation of a triangular WS_2 grain adsorbed on the c-plane sapphire. (a,b) Atomic models of the calculated model used for 0° orientation (epitaxially aligned). (a) Tile view and (b) top view. (c) Comparison of optimized WS_2-sapphire distances and adsorption energies. The positive value in the adsorption energy indicates higher adsorption energy, *i.e.* stronger WS_2-sapphire coupling.

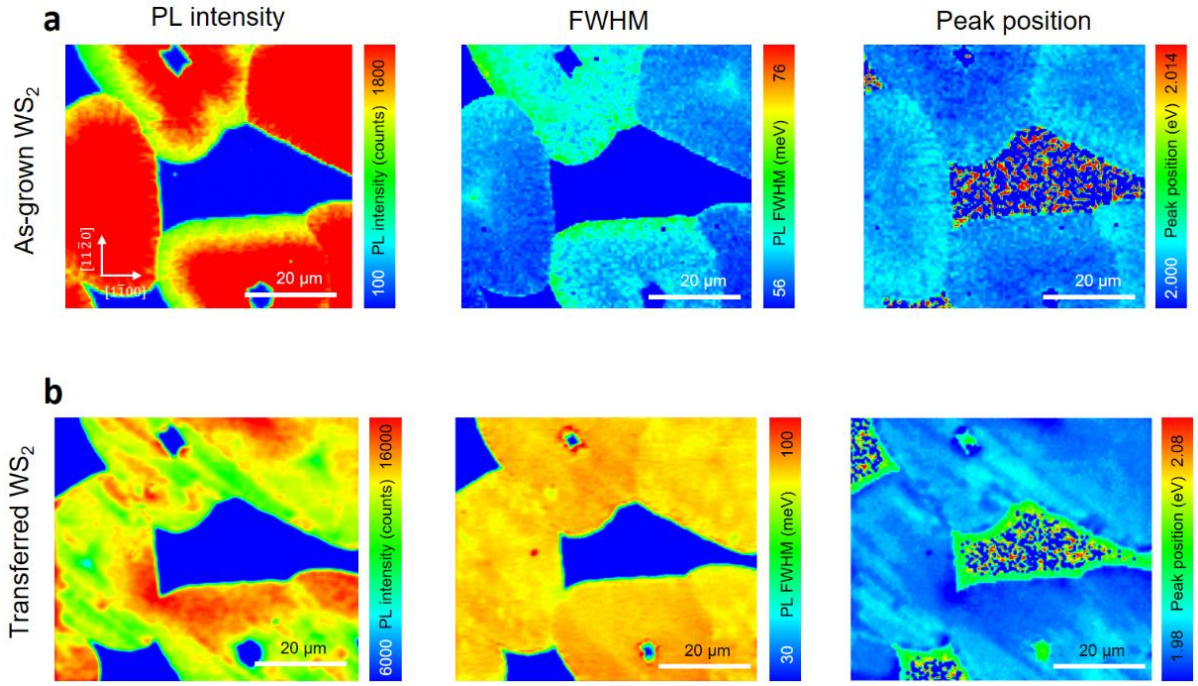

Figure 4.9. PL mapping images of identical WS_2 grains before (a) and after (b) transfer on SiO_2/Si substrate. The difference in PL intensity observed between aligned- and misaligned-grains in as-grown WS_2 disappeared after the transfer process. The wavy patterns observed in the PL intensity of the transferred WS_2 (b) are from wrinkles induced during transfer process.

(1.78 Å). The adsorption energy is higher for the aligned grain, probably due to the enhanced WS_2-sapphire coupling with the consistent symmetry. These results indicate that the aligned WS_2 grains are more strongly bound to the sapphire surface compared with misaligned ones. It is speculated that such strong coupling with the sapphire surface seen in the aligned WS_2 grain results in the reduction of the PL intensity and the line broadening (see Figure 4.5a-d). It is interesting to note that the graphene grains aligned on Cu (111) also suffers from strong strain,[44,45] suggesting that the grain alignment strongly affects the physical properties of 2D materials.

The strain in the aligned WS_2 grains was found to be released when detached from the sapphire surface. Figure 4.9 displays the PL mapping images of identical WS_2 grains taken before and after the transfer process. The weaker PL seen in the aligned

WS_2 grains (Figure 4.9a) showed the similar intensity with misaligned grains after the transfer (Figure 4.9b). Therefore, a different degree of coupling with sapphire substrate is considered to modulate the optical property of as-grown WS_2.

Also, to explain the preferential multilayer growth observed on the aligned grains, DFT calculation was performed for the strained bilayer WS_2 sheets. Van der Waals energy between the stacked bilayer WS_2 sheets were calculated while applying the tension to both the upper and lower layers. By inducing 4% of the tensile strain, the total energy of the stacked bilayers decreased by 2 meV per two pairs of S-W-S units. This indicates that the tensile strain enhances the van der Waals coupling between WS_2 layers, suggesting the ease of formation of multilayer grain on the strained WS_2 grain. When the tensile strain is introduced, a WS_2 layer can be slightly flattened so that the electron density within a layer is increased, thus giving stronger van der Waals coupling between the two strained WS_2 layers.[43] Although the actual system is more complicated than the present theoretical model, our present result qualitatively explains our experimental result.

4.3.3. PL spectra of MoS_2 grains on sapphire

For comparison, MoS_2 grains were also synthesized on c-plane sapphire using MoO_3 and S feedstocks using the similar setup shown in Figure 4.1.[46] The growth condition was modified to obtain both aligned and misaligned MoS_2 grains on the same sapphire substrate. As seen in Figure 4.10, the reduction of the PL intensity was also observed in the aligned MoS_2. Considering the similarity between WS_2 and MoS_2, such as a similar hexagonal crystal structure with comparable lattice constant, strong influence of the sapphire is deduced on the as-grown TMD materials.

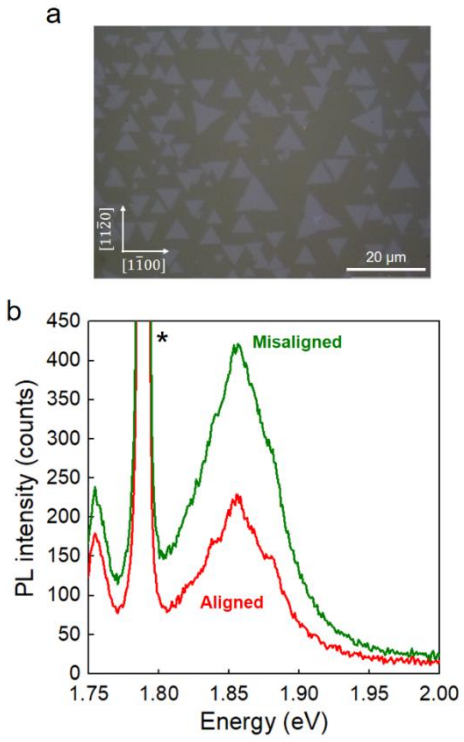

Figure 4.10. OM image and PL spectra of MoS_2 grown on c-plane sapphire. In OM image (a), preferentially oriented grains are observed along [1$\bar{1}$00] axis of sapphire substrate. PL spectra are shown in (b) where red and green spectra correspond to PL from aligned- and misaligned-grains, respectively. Asterisk (*) indicates the peaks from a sapphire substrate. The peak at ~1.76 eV corresponds to bound exciton in MoS_2.

4.3.4. WS_2 growth on other sapphire planes

The TMD alignment is originated from the symmetrical matching of TMD lattice and the crystalline surface of c-plane sapphire. I investigated other crystalline planes, a-plane [1$\bar{1}$00] and r-plane [1$\bar{1}$02] sapphire as growth substrates of WS_2. These substrates were placed in the CVD chamber together with c-plane sapphire. The optical micrographs of as-grown WS_2, the surface crystal structure of each sapphire plane, grain orientation distribution, and PL spectra are compared in Figure 4.11.

Totally different growth behavior was observed depending on the sapphire substrates. Although the growth condition is optimized for c-plane sapphire, clear difference can be seen for each of growth substrate, which indicates the crystal structure of a substrate

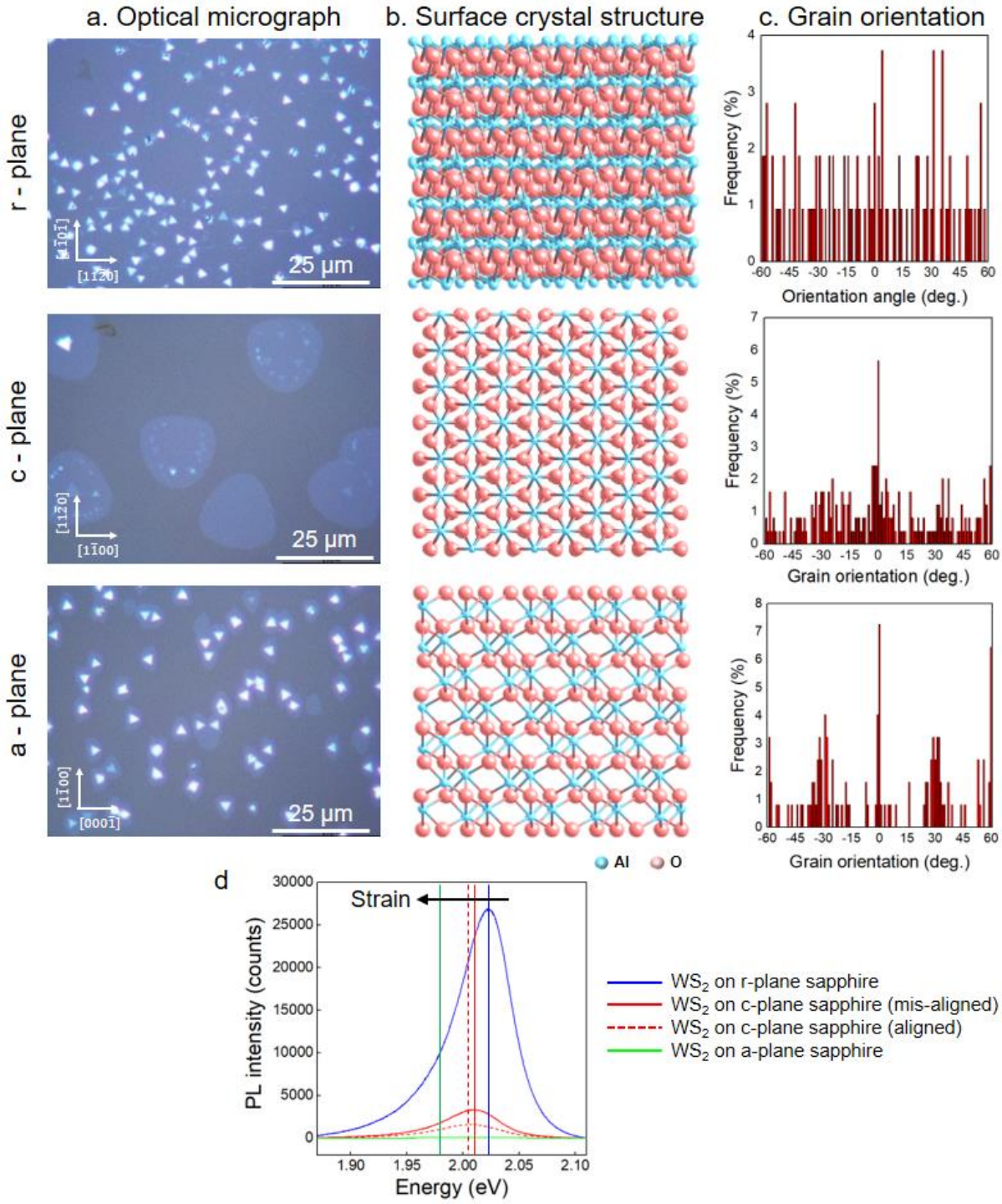

Figure 4.11. (a) OM images of CVD-grown WS_2 on different planes of sapphire substrates. (b) Surface crystal structure of each sapphire plane. (c) Grain orientation histogram of WS_2 grown on each sapphire plane. $[11\bar{2}0]$, $[1\bar{1}00]$, and $[000\bar{1}]$ axes are set as 0° for r-, c-, and a-plane sapphire, respectively. (d) PL spectra from the as-grown WS_2 grains.

significantly influences the growth of WS_2. I observed high WS_2 coverage on r-plane sapphire, but the grains are randomly oriented (Figure 4.11a). The intense PL emission was observed from these misoriented WS_2 grains (Figure 4.11d). These results reflect weak WS_2-sapphire interaction. On the other hand, WS_2 grown on a-plane showed a low WS_2 coverage, weak PL emission, and some preferential grain orientations. Thus, the a-plane sapphire induces stronger interaction with WS_2. As seen in Figure 4.11, the PL from WS_2 grown on r- and a-plane sapphire showed blue-and red-shift, respectively, with respect to that on c-plane sapphire. This could reflect the degree of strain induced in each WS_2.

4.3.5. Low temperature PL

For further analysis of WS_2 grains grown on sapphire, low temperature PL was measured, because the low temperature measurement allows us to understand intrinsic properties of TMDs which cannot be seen at room temperature due to thermally activated decay paths of excitons. Figure 4.12a shows PL spectra of as-grown, aligned (red) and misaligned (green) WS_2 grains measured at different temperatures in vacuum. Both the aligned and misaligned grains exhibited clear blue-shift of the PL peak from ~2.01 eV (300 K) to 2.10 eV (10 K).[47] Notably, all the PL spectra (both of aligned and misaligned grains) were found to be fitted with a single peak even at 10 K. Almost no subpeaks were observed even at the low temperatures. This result indicates that relaxation of excitons via trion formation or through defect states is strongly suppressed on the sapphire surface. This suggests that the exciton lifetime is very short on the sapphire due to strong van der Waals interaction. The PL intensity is plotted in Figure 4.12c. The PL intensity of the aligned WS_2 is lower than the misaligned WS_2 at all the

measured temperatures. Thus, WS_2-sapphire interaction is stronger for the aligned grains.[40] The linewidth decreased monotonically for both the aligned and misaligned grains (Figure 4.12d), indicating the suppression of exciton scattering by phonons.

Figure 4.12b shows the PL spectra taken after transferring WS_2 grains on SiO_2 substrate. In these transferred samples, multiple peaks were observed at all the measurement temperatures. The PL peaks of the transferred WS_2 grains consist of the subpeaks originated in neutral excitons, trions, and defect states (or less likely bi-excitons)[51] which were not detected in the as-grown samples. This signifies that the WS_2-substrate interaction is weakened, and the WS_2 is heavily doped due to the transfer process and from SiO_2 surface.[10,39] It is also noted that the PL peak shapes of the

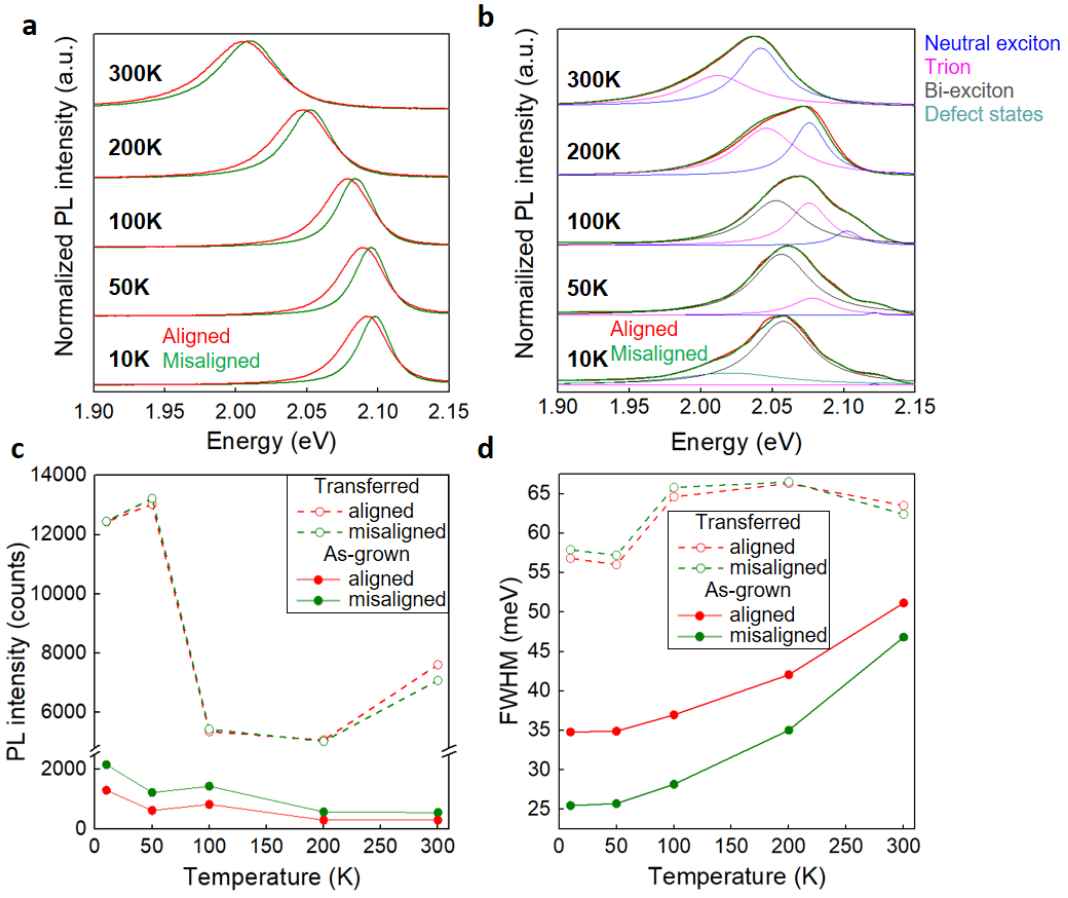

Figure 4.12. Normalized PL spectra of as-grown (a) and transferred (b) WS_2 grains measured at different temperatures. Plots of PL intensity (c) and FWHM (d) of as-grown and transferred WS_2. Legends used in (c) are the same in (d).

aligned and misaligned grains are almost the same, indicating the comparable crystal quality of the aligned and misaligned WS_2 grains. Thus, the possibility of low crystallinity of the aligned WS_2 grains can be excluded from the reasons of the reduced PL intensity seen in the as-grown grains (see Figures 4.5a,d, 4.7c, and 4.9a).

4.3.6. Transport property

I measured the carrier transport properties after transferring the WS_2 grains on SiO_2 substrates for back-gate device operation. I used photolithography and lift-off processes to pattern metal electrodes (Ni/Au). Figure 4.13 insets are optical micrographs of WS_2 devices. Figure 4.13a displays representative transfer curves of FETs of the aligned and misaligned WS_2 grains. Clear n-type carrier transport with a high on/off ratio (10^5-10^6) was observed for both the aligned and misaligned WS_2 grains. The carrier mobility was calculated by using the following equation:

$$\mu = \frac{g_{\mathrm{m}}}{C_{\mathrm{ox}} V_{\mathrm{d}}} \frac{L}{W} \tag{4.1}$$

where $g_{\mathrm{m}} = \mathrm{d}I_{\mathrm{d}}/\mathrm{d}V_{\mathrm{g}}$ is the transconductance obtained from the transfer curves, $C_{\mathrm{ox}} = 11.5$ nF/cm^2 is the capacitance per unit area of 300 nm-thick SiO_2, V_{d} is the applied drain voltage, and L and W represent the length and width of the both aligned and misaligned grains. Here, the carrier mobility was calculated by assuming a trapezoidal channel shape to take into account the geometrical effect. Figure 4.13b shows the distribution of mobility and on/off ratio measured for different grains. No clear difference was observed between the aligned and misaligned grains. This is consistent with the low-temperature PL spectra measured after the transfer (see Figure 4.13b). Thus, it can be

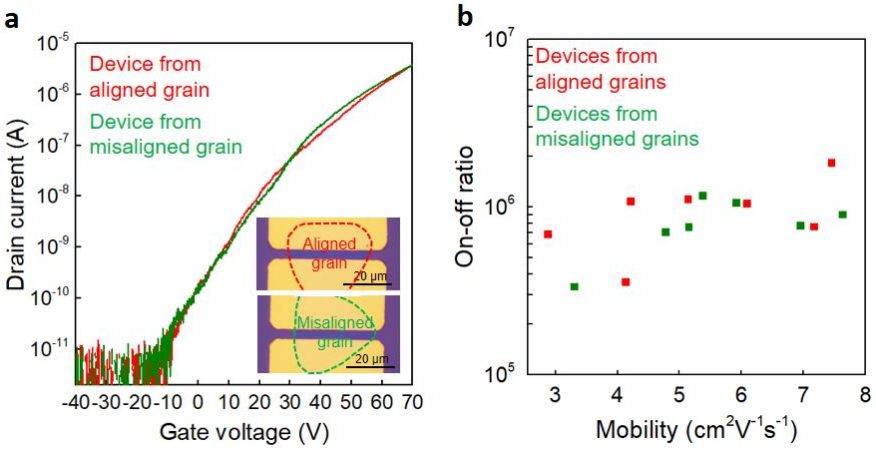

Figure 4.13. (a) Transfer curves of aligned and misaligned WS_2 grains which were measured after the transfer on SiO_2/Si substrate for back-gate geometry (V_d = 1 V). The inset shows OM images of fabricated FET devices. (b) Distribution of electron mobility and on-off ratio.

conclude the overlayer deposition as well as PL quenching in the aligned WS_2 grains is originated in the strong van der Waals interaction between WS_2 and sapphire.

This work offers several potential applications for modifying electronic and geometric structures of WS_2 when epitaxially grown on c-plane sapphire substrates. Firstly, the strong coupling with the sapphire surface induce larger strain which can be utilized to chemically functionalize or dope the TMD materials. Secondly, the preferential growth of multilayer WS_2 can be used to make high mobility transistors, because it is known that monolayer TMD suffers strong influence from the substrate and top gate insulator. Thirdly, well aligned TMD grains lead to the effective grain stitching that can be developed to wafer scale single-crystal TMD sheet. Finally, the orientation-controlled growth can be used to tune the electronic and magnetic properties by stacking different materials with controlled orientations (moiré effect).

4.4. Conclusions

This chapter presents that the aligned WS_2 grains suffer more strain due to stronger van der Waals interaction with sapphire substrate as compared with the misaligned WS_2. This strain induces the overlayer WS_2 deposition, resulting in the formation of multilayer WS_2 grains selectively on the aligned grains. The epitaxially grown grains showed reduced PL and Raman peaks. The DFT calculations indicate the strong coupling of WS_2 grains with the sapphire surface when the grains are aligned along the sapphire lattice. It was also found that the strong coupling with sapphire does not cause severe crystal defects in the epitaxially grown grains, even though strong strain is induced. This work gives new understanding of the influence of sapphire on the growth behavior of TMDs.

References

(1) Kang, K.; Xie, S.; Huang, L.; Han, Y.; Huang, P. Y.; Mak, K. F.; Kim, C.-J.; Muller, D.; Park, J. High-Mobility Three-Atom-Thick Semiconducting Films with Wafer-Scale Homogeneity. *Nature* **2015**, *520*, 656–660.

(2) Yu, H.; Liao, M.; Zhao, W.; Liu, G.; Zhou, X. J.; Wei, Z.; Xu, X.; Liu, K.; Hu, Z.; Deng, K.; Zhou, S.; Shi, J.-A.; Gu, L.; Shen, C.; Zhang, T.; Du, L.; Xie, L.; Zhu, J.; Chen, W.; Yang, R.; Shi, D.; Zhang, G. Wafer-Scale Growth and Transfer of Highly-Oriented Monolayer MoS_2 Continuous Films. *ACS Nano* **2017**, *11*, 12001–12007.

(3) Zhang, Y.; Zhang, Y.; Ji, Q.; Ju, J.; Yuan, H.; Shi, J.; Gao, T.; Ma, D.; Liu, M.; Chen, Y.; Song, X.; Hwang, H. Y.; Cui, Y.; Liu, Z. Controlled Growth of High-Quality Monolayer WS_2 Layers on Sapphire and Imaging Its Grain Boundary. *ACS Nano* **2013**, *7*, 8963–8971.

(4) Kang, K. N.; Godin, K.; Yang, E.-H. The Growth Scale and Kinetics of WS_2 Monolayers under Varying H_2 Concentration. *Sci. Rep.* **2015**, *5*, 13205.

(5) McCreary, K. M.; Hanbicki, A. T.; Jernigan, G. G.; Culbertson, J. C.; Jonker, B. T. Synthesis of Large-Area WS_2 Monolayers with Exceptional Photoluminescence. *Sci. Rep.* **2016**, *6*, 19159.

(6) Gong, Y.; Ye, G.; Lei, S.; Shi, G.; He, Y.; Lin, J.; Zhang, X.; Vajtai, R.; Pantelides, S. T.; Zhou, W.; Li, B.; Ajayan, P. M. Synthesis of Millimeter-Scale Transition Metal Dichalcogenides Single Crystals. *Adv. Funct. Mater.* **2016**, *26*, 2009–2015.

(7) Sheng, Y.; Tan, H.; Wang, X.; Warner, J. H. Hydrogen Addition for Centimeter-Sized Monolayer Tungsten Disulfide Continuous Films by Ambient Pressure Chemical Vapor Deposition. *Chem. Mater.* **2017**, *29*, 4904–4911.

(8) Ji, H. G.; Lin, Y.-C.; Nagashio, K.; Maruyama, M.; Solís-Fernández, P.; Sukma Aji, A.; Panchal, V.; Okada, S.; Suenaga, K.; Ago, H. Hydrogen-Assisted Epitaxial Growth of Monolayer Tungsten Disulfide and Seamless Grain Stitching. *Chem. Mater.* **2018**, *30*, 403–411.

(9) Gao, Y.; Liu, Z.; Sun, D.-M.; Huang, L.; Ma, L.-P.; Yin, L.-C.; Ma, T.; Zhang, Z.; Ma, X.-L.; Peng, L.-M.; Cheng, H.-M.; Ren, W. Large-Area Synthesis of High-Quality and Uniform Monolayer WS_2 on Reusable Au Foils. *Nat. Commun.* **2015**, *6*, 8569.

(10) Xu, Z.-Q.; Zhang, Y.; Lin, S.; Zheng, C.; Zhong, Y. L.; Xia, X.; Li, Z.; Sophia, P. J.; Fuhrer, M. S.; Cheng, Y.-B.; Bao, Q. Synthesis and Transfer of Large-Area Monolayer WS_2 Crystals: Moving Toward the Recyclable Use of Sapphire Substrates. *ACS Nano* **2015**, *9*, 6178–6187.

(11) Yun, S. J.; Chae, S. H.; Kim, H.; Park, J. C.; Park, J.-H.; Han, G. H.; Lee, J. S.; Kim, S. M.; Oh, H. M.; Seok, J.; Jeong, M. S.; Kim, K. K.; Lee, Y. H. Synthesis of Centimeter-Scale Monolayer Tungsten Disulfide Film on Gold Foils. *ACS Nano* **2015**, *9*, 5510–5519.

(12) Lim, Y. R.; Han, J. K.; Kim, S. K.; Lee, Y. B.; Yoon, Y.; Kim, S. J.; Min, B. K.; Kim, Y.; Jeon, C.; Won, S.; Kim, J.-H.; Song, W.; Myung, S.; Lee, S. S.; An, K.-S.; Lim, J. Roll-to-Roll Production of Layer-Controlled Molybdenum Disulfide: A Platform for 2D Semiconductor-Based Industrial Applications. *Adv. Mater.* **2018**, *30*, 1705270.

(13) van der Zande, A. M.; Huang, P. Y.; Chenet, D. A.; Berkelbach, T. C.; You, Y.; Lee, G.-H.; Heinz, T. F.; Reichman, D. R.; Muller, D. A.; Hone, J. C. Grains and Grain Boundaries in Highly Crystalline Monolayer Molybdenum Disulphide. *Nat. Mater.* **2013**, *12*, 554–561.

(14) Najmaei, S.; Liu, Z.; Zhou, W.; Zou, X.; Shi, G.; Lei, S.; Yakobson, B. I.; Idrobo, J.-C.; Ajayan, P. M.; Lou, J. Vapour Phase Growth and Grain Boundary Structure of Molybdenum Disulphide Atomic Layers. *Nat. Mater.* **2013**, *12*, 754–759.

(15) Zhou, W.; Zou, X.; Najmaei, S.; Liu, Z.; Shi, Y.; Kong, J.; Lou, J.; Ajayan, P. M.; Yakobson, B. I.; Idrobo, J.-C. Intrinsic Structural Defects in Monolayer Molybdenum Disulfide. *Nano Lett.* **2013**, *13*, 2615–2622.

(16) Azizi, A.; Zou, X.; Ercius, P.; Zhang, Z.; Elías, A. L.; Perea-López, N.; Stone, G.; Terrones, M.; Yakobson, B. I.; Alem, N. Dislocation Motion and Grain Boundary Migration in Two-Dimensional Tungsten Disulphide. *Nat. Commun.* **2014**, *5*, 4867.

(17) Ly, T. H.; Chiu, M.-H.; Li, M.-Y.; Zhao, J.; Perello, D. J.; Cichocka, M. O.; Oh, H. M.; Chae, S. H.; Jeong, H. Y.; Yao, F.; Li, L.-J.; Lee, Y. H. Observing Grain Boundaries in CVD-Grown Monolayer Transition Metal Dichalcogenides. *ACS Nano* **2014**, *8*, 11401–11408.

(18) Rong, Y.; He, K.; Pacios, M.; Robertson, A. W.; Bhaskaran, H.; Warner, J. H. Controlled Preferential Oxidation of Grain Boundaries in Monolayer Tungsten Disulfide for Direct Optical Imaging. *ACS Nano* **2015**, *9*, 3695–3703.

(19) Ly, T. H.; Perello, D. J.; Zhao, J.; Deng, Q.; Kim, H.; Han, G. H.; Chae, S. H.; Jeong, H. Y.; Lee, Y. H. Misorientation-Angle-Dependent Electrical Transport across Molybdenum Disulfide Grain Boundaries. *Nat. Commun.* **2016**, *7*, 10426.

(20) Chen, L.; Liu, B.; Ge, M.; Ma, Y.; Abbas, A. N.; Zhou, C. Step-Edge-Guided Nucleation and Growth of Aligned WSe_2 on Sapphire via a Layer-over-Layer Growth Mode. *ACS Nano* **2015**, *9*, 8368–8375.

(21) Perdew, J. P.; Burke, K.; Ernzerhof, M. Generalized Gradient Approximation Made Simple. *Phys. Rev. Lett.* **1996**, *77*, 3865–3868.

(22) Lee, K.; Murray, É. D.; Kong, L.; Lundqvist, B. I.; Langreth, D. C. A Higher-Accuracy van Der Waals Density Functional. *Phys. Rev. B* **2010**, *82*, 081101(R).

(23) Cooper, V. R. Van Der Waals Density Functional: An Appropriate Exchange Functional. *Phys. Rev. B* **2010**, *81*, 161104.

(24) Morikawa, Y.; Iwata, K.; Terakura, K. Theoretical Study of Hydrogenation Process of Formate on Clean and Zn Deposited Cu(111) Surfaces. *Appl. Surf. Sci.* **2001**, *169*, 11–15.

(25) Vanderbilt, D. Soft Self-Consistent Pseudopotentials in a Generalized Eigenvalue Formalism. *Phys. Rev. B* **1990**, *41*, 7892–7895.

(26) Gurarslan, A.; Yu, Y.; Su, L.; Yu, Y.; Suarez, F.; Yao, S.; Zhu, Y.; Ozturk, M.; Zhang, Y.; Cao, L. Surface-Energy-Assisted Perfect Transfer of Centimeter-Scale Monolayer and Few-Layer MoS_2 Films onto Arbitrary Substrates. *ACS Nano* **2014**, *8*, 11522–11528.

(27) Dobrovinskaya, E. R.; Lytvynov, L. A.; Pishchik, V. Properties of Sapphire. In *Sapphire*; Micro- and Opto-Electronic Materials, Structures, and Systems; Springer US, 2009; pp 55–176.

(28) Dumcenco, D.; Ovchinnikov, D.; Marinov, K.; Lazić, P.; Gibertini, M.; Marzari, N.; Sanchez, O. L.; Kung, Y.-C.; Krasnozhon, D.; Chen, M.-W.; Bertolazzi, S.; Gillet, P.; Fontcuberta i Morral, A.; Radenovic, A.; Kis, A. Large-Area Epitaxial Monolayer MoS_2. *ACS Nano* **2015**, *9*, 4611–4620.

(29) Castellanos-Gomez, A.; Roldán, R.; Cappelluti, E.; Buscema, M.; Guinea, F.; van der Zant, H. S. J.; Steele, G. A. Local Strain Engineering in Atomically Thin MoS_2. *Nano Lett.* **2013**, *13*, 5361–5366.

(30) Conley, H. J.; Wang, B.; Ziegler, J. I.; Haglund, R. F.; Pantelides, S. T.; Bolotin, K. I. Bandgap Engineering of Strained Monolayer and Bilayer MoS_2. *Nano Lett.* **2013**, *13*, 3626–3630.

(31) McCreary, K. M.; Hanbicki, A. T.; Singh, S.; Kawakami, R. K.; Jernigan, G. G.; Ishigami, M.; Ng, A.; Brintlinger, T. H.; Stroud, R. M.; Jonker, B. T. The Effect of Preparation Conditions on Raman and Photoluminescence of Monolayer WS_2. *Sci. Rep.* **2016**, *6*, 35154.

(32) Feng, S.; Yang, R.; Jia, Z.; Xiang, J.; Wen, F.; Mu, C.; Nie, A.; Zhao, Z.; Xu, B.; Tao, C.; Tian, Y.; Liu, Z. Strain Release Induced Novel Fluorescence Variation in CVD-Grown Monolayer WS_2 Crystals. *ACS Appl. Mater. Interfaces* **2017**, *9*, 34071–34077.

(33) Nakanishi, T.; Yoshida, S.; Murase, K.; Takeuchi, O.; Taniguchi, T.; Watanabe, K.; Shigekawa, H.; Kobayashi, Y.; Miyata, Y.; Shinohara, H.; Kitaura, R. The Atomic and Electronic Structure of 0° and 60° Grain Boundaries in MoS_2. *Front. Phys.* **2019**, *7*, 59.

(34) Ago, H.; Fukamachi, S.; Endo, H.; Solís-Fernández, P.; Mohamad Yunus, R.; Uchida, Y.; Panchal, V.; Kazakova, O.; Tsuji, M. Visualization of Grain Structure and Boundaries of Polycrystalline Graphene and Two-Dimensional Materials by Epitaxial Growth of Transition Metal Dichalcogenides. *ACS Nano* **2016**, *10*, 3233–3240.

(35) Suenaga, K.; Ji, H. G.; Lin, Y.-C.; Vincent, T.; Maruyama, M.; Aji, A. S.; Shiratsuchi, Y.; Ding, D.; Kawahara, K.; Okada, S.; Panchal, V.; Kazakova, O.; Hibino, H.; Suenaga, K.; Ago, H. Surface-Mediated Aligned Growth of Monolayer MoS_2 and In-Plane Heterostructures with Graphene on Sapphire. *ACS Nano* **2018**, *12*, 10032-10044.

(36) Kang, N.; Paudel, H. P.; Leuenberger, M. N.; Tetard, L.; Khondaker, S. I. Photoluminescence Quenching in Single-Layer MoS_2 via Oxygen Plasma Treatment. *J. Phys. Chem. C* **2014**, *118*, 21258–21263.

(37) Gao, J.; Li, B.; Tan, J.; Chow, P.; Lu, T.-M.; Koratkar, N. Aging of Transition Metal Dichalcogenide Monolayers. *ACS Nano* **2016**, *10*, 2628–2635.

(38) He, Z.; Wang, X.; Xu, W.; Zhou, Y.; Sheng, Y.; Rong, Y.; Smith, J. M.; Warner, J. H. Revealing Defect-State Photoluminescence in Monolayer WS_2 by Cryogenic Laser Processing. *ACS Nano* **2016**, *10*, 5847–5855.

(39) Yu, Y.; Yu, Y.; Xu, C.; Cai, Y.-Q.; Su, L.; Zhang, Y.; Zhang, Y.-W.; Gundogdu, K.; Cao, L. Engineering Substrate Interactions for High Luminescence Efficiency of Transition-Metal Dichalcogenide Monolayers. *Adv. Funct. Mater.* **2016**, *26*, 4733–4739.

(40) Liu, Z.; Amani, M.; Najmaei, S.; Xu, Q.; Zou, X.; Zhou, W.; Yu, T.; Qiu, C.; Birdwell, A. G.; Crowne, F. J.; Vajtai, R.; Yakobson, B. I.; Xia, Z.; Dubey, M.; Ajayan, P. M.; Lou, J. Strain and Structure Heterogeneity in MoS_2 Atomic Layers Grown by Chemical Vapour Deposition. *Nat. Commun.* **2014**, *5*, 5246.

(41) Chow, P. K.; Jacobs-Gedrim, R. B.; Gao, J.; Lu, T.-M.; Yu, B.; Terrones, H.; Koratkar, N. Defect-Induced Photoluminescence in Monolayer Semiconducting Transition Metal Dichalcogenides. *ACS Nano* **2015**, *9*, 1520–1527.

(42) Wang, Y.; Cong, C.; Yang, W.; Shang, J.; Peimyoo, N.; Chen, Y.; Kang, J.; Wang, J.; Huang, W.; Yu, T. Strain-Induced Direct–Indirect Bandgap Transition and Phonon Modulation in Monolayer WS_2. *Nano Res.* **2015**, *8*, 2562–2572.

(43) Pak, S.; Lee, J.; Lee, Y.-W.; Jang, A.-R.; Ahn, S.; Ma, K. Y.; Cho, Y.; Hong, J.; Lee, S.; Jeong, H. Y.; Im, H.; Shin, H. S.; Morris, S. M.; Cha, S.; Sohn, J. I.; Kim, J. M. Strain-Mediated Interlayer Coupling Effects on the Excitonic Behaviors in an Epitaxially Grown MoS_2/WS_2 van Der Waals Heterobilayer. *Nano Lett.* **2017**, *17*, 5634–5640.

(44) He, R.; Zhao, L.; Petrone, N.; Kim, K. S.; Roth, M.; Hone, J.; Kim, P.; Pasupathy, A.; Pinczuk, A. Large Physisorption Strain in Chemical Vapor Deposition of Graphene on Copper Substrates. *Nano Lett.* **2012**, *12*, 2408–2413.

(45) Frank, O.; Vejpravova, J.; Holy, V.; Kavan, L.; Kalbac, M. Interaction between Graphene and Copper Substrate: The Role of Lattice Orientation. *Carbon* **2014**, *68*, 440–451.

(46) Ago, H.; Endo, H.; Solís-Fernández, P.; Takizawa, R.; Ohta, Y.; Fujita, Y.; Yamamoto, K.; Tsuji, M. Controlled van Der Waals Epitaxy of Monolayer MoS_2 Triangular Domains on Graphene. *ACS Appl. Mater. Interfaces* **2015**, *7*, 5265–5273.

(47) Okada, M.; Miyauchi, Y.; Matsuda, K.; Taniguchi, T.; Watanabe, K.; Shinohara, H.; Kitaura, R. Observation of Biexcitonic Emission at Extremely Low Power Density in Tungsten Disulfide Atomic Layers Grown on Hexagonal Boron Nitride. *Sci. Rep.* **2017**,

7, 322.

Chapter 5

Chemical Control of Electrical Transport Polarity of Transition Metal Dichalcogenides for Advanced Electronics

Abstract

Monolayers of TMDs have attracted a great interest for post-silicon electronics and photonics due to their high carrier mobility, tunable band gap, and atom-thick two-dimensional structure. With the analogy to conventional silicon electronics, establishing a method to convert TMD to p- and n-type semiconductors is essential for various device applications, such as CMOS circuits and photovoltaics. In this chapter, a successful control of the electrical polarity of monolayer WSe_2 by chemical doping is demonstrated. Two different molecules, 4-NBD and DETA, were utilized to convert ambipolar WSe_2 FETs to p- and n-type, respectively. Moreover, the chemically doped WSe_2 showed increased effective carrier mobilities of 82 and 25 $cm^2V^{-1}s^{-1}$ for holes and electrons, respectively, which are much higher than those of the pristine WSe_2. The doping effects were studied by PL, Raman, XPS, and DFT calculations. Chemically tuned WSe_2 FETs were integrated into CMOS inverters, exhibiting extremely low power consumption (~0.17 nW). Furthermore, a p-n junction within a single WSe_2 grain was realized via spatially-controlled chemical doping. The chemical doping method reported in this chapter for controlling the transport properties of WSe_2 is expected to contribute to the development of TMD-based advanced electronics.

5.1. Introduction

Silicon forms the basis of the modern electronics, and controlled doping techniques have been widely used to fabricate both p- and n-type semiconductors made from silicon. Such spatially controlled doping techniques greatly contributed to the prevalence of Si-based CMOS circuits, photovoltaic cells, and optical sensors. Atomically thin TMD semiconductors, a part of the family of 2D materials, have attracted a great interest as a new alternative to silicon. This is because the monolayer TMDs show excellent electrical transport properties with high on/off ratios, strong PL in the visible range, and tunable band gap ranging from 1.5 to 2 eV depending on the combination of transition metals and chalcogenides.[1–8] Recent development of the CVD method for the wafer-scale growth of TMDs have accelerated the research on their electronic and optoelectronic devices, including logic circuits, photodetectors, solar cells, and light emitting diodes.[7,9–13]

However, the precise control of the polarity in TMD devices is still difficult, thus hindering practical applications. This is because most of TMDs, such as MoS_2 and WS_2, are n-type semiconductors due to the unavoidable presence of S vacancies.[14,15] Attempts to convert n-type MoS_2 or WS_2 to p-type semiconductors have been reported. For example, partial substitution of Mo (or W) atoms with Nb and other metal atoms changed MoS_2 (or WS_2) to p-type character. However, the $Mo_xNb_{1-x}S_2$ devices show very weak gate dependence, reflecting a heavily degenerated state originated in the inserted Nb atoms.[16] Different types of dopants, such as thiol-based molecules and Zn atoms, were also used to dope MoS_2.[17,18] In these works, the threshold voltage (V_{th}) of devices shifts to higher gate voltages reflecting hole doping, but the main carriers are still electrons as observed from the corresponding transfer characteristics.[17,18]

Being different from MoS_2 and WS_2, pristine WSe_2 is known to show ambipolar behavior. Chen *et al.* reported the p-doping effect of Au nanoparticles deposited on WSe_2.[19] However, the Au-coated WSe_2 still shows ambipolar behavior rather than p-type transport. Moreover, the PL from WSe_2 was strongly quenched by the nanoparticles, which is a disadvantage for optical applications. In ambient condition, p-type transport characteristics were observed for WSe_2.[20,21] Different metal contacts, Pd and Ag were used to operate p-type and n-type WSe_2, respectively,[22,23] though multiple electrode deposition processes are needed for the device fabrication. Partial substitution of Se atom with P was reported to induce p-type doping on WSe_2, but its influence on the electrical transport property was not studied.[24] In contrast, a mild plasma treatment was introduced to generate Se defect on WSe_2 to achieve n-type doping.[25] The defect engineering was utilized only for n-type doping but not for p-type doping and, more importantly, Se defects generally deteriorate the physical properties.

Consequently, it is difficult to obtain both p- and n-type transport properties using an identical TMD without changing the contact metal. Therefore, previous works combined different types of TMDs, such as p-type WSe_2 (or p-type $MoTe_2$) and n-type MoS_2, to fabricate CMOS circuits.[13,26,27] Alternatively, very high effective gate voltages were applied to operate p- and n-type WSe_2 channels with the aid of ionic liquid.[28] Recently molecular doping technique was applied to various exfoliated TMD flakes, and both p- and n-type doping effects were observed. In this work, however, different metals, Pd and Ti, were used for p- and n-doping, and the use of exfoliated TMD flakes limited the practical applications.[29]

In this chapter, the chemical doping of large-area CVD-grown WSe_2 monolayers was performed for selective conversion from ambipolar to p- and n-type semiconductors

without changing the contact electrodes. The doping treatments were found to increase the effective carrier mobilities up to four orders of magnitude above the threshold region with respect to the pristine WSe_2, obtaining maximum values of 82 $cm^2V^{-1}s^{-1}$ and 25 $cm^2V^{-1}s^{-1}$ for holes and electrons, respectively. The chemically doped WSe_2 monolayers were integrated into CMOS circuits that showed extremely low power consumption (~ 170 pW with V_{gain} of ~10). Moreover, spatially controlled doping was also achieved within a single WSe_2 grain to obtain separated p- and n-doped regions. The WSe_2 grain with the artificial p-n junction showed clear rectification behavior and optical response to visible light, implying its potential for photodetection applications.[30–34]

5.2. Experimental method

5.2.1. CVD growth of WSe_2 and WS_2

Monolayer WSe_2 was synthesize by Prof. Miyata's laboratory in Tokyo Metropolitan University using an improved salt-assisted CVD method with WO_3 and Se powders. KBr powder was used as a growth promoter.[22] In a tubular furnace, WO_3 and KBr were placed 2 cm and 9 cm upstream of the SiO_2/Si substrate. Temperatures of the substrate and the WO_3 were gradually increased to the growth temperature (780 °C) with a N_2/H_2 gas mixture at a flow rate of 400/1.2 ccm. After the substrate reached the growth temperature, Se was heated to 300~370 °C by using another furnace to supply Se vapor to grow WSe_2. After 10 min reaction, the sample was cooled down immediately.

In our laboratory, WS_2 was synthesized by ambient pressure CVD method using WO_3 powder and S power. Growth promoter was not used for WS_2 growth and c-plane sapphire was used as a growth substrate. The details of the WS_2 synthesis are reported elsewhere.[32]

5.2.2. Chemical doping

For p-type doping, a WSe_2 sample was immersed in aqueous solution of 4-NBD with concentrations of 10~100 mM and left in dark environment. The sample was kept in the solution at 60 °C for 30 minutes. For n-type doping, a WSe_2 sample was exposed to DETA vapor (~460 Pa vapor pressure) at 70 °C for 30 minutes.[35] In the closed petri dish with ~100 cm^3 volume, 300 μL of DETA was placed for applying DETA vapor to WSe_2.

5.2.3. Characterization

Optical micrographs were taken using an optical microscope (Nikon Eclipse ME 600), and the AFM height images were collected using a Nanoscope V Multimode SPM (Bruker Co.). PL and Raman spectra were measured using a confocal Raman spectroscope (Tokyo Instruments Inc., Nanofinder 30) under 532 nm laser excitation. XPS measurements were conducted in the beamline 10 (BL10) of SAGA Light Source (SAGA-LS) at 10^{-8} Pa with the incident energy of 600 eV. For the XPS measurement, WSe_2 grains were transferred to an Au-coated SiO_2/Si substrate, followed by respective doping processes.

5.2.4. DFT calculation

Electronic structure calculations of DETA, 4-NBD, and WSe_2 were conducted using the DFT implemented in the STATE code.[36] The exchange correlation interaction among interacting electrons is expressed by the generalized gradient approximation (GGA) with the PBE functional form. For the electron-ion interaction, ultrasoft pseudopotentials generated by the Vanderbilt scheme was adopted. The valence wave functions and deficit charge density were expanded in conjunction with a plane-wave basis set, applying cutoff energies of 25 and 225 Ryd, respectively. To obtain qualitative insight into the possibility of the charge transfer from the dopant molecules, 4-NBD and DETA, to WSe_2, the absolute values of the electron energy levels of isolated 4-NBD, DETA, and WSe_2 was evaluated by DFT calculations. For the evaluation of the energy level with respect to the vacuum, super cell calculations were conducted for isolated molecules and WSe_2 in which the molecules or WSe_2 are separated their periodic images by at least 1.5 nm vacuum spacing. For WSe_2, a 4×4 lateral periodicity was considered to evaluate the effect of chalcogen defects on the electronic energy band. The geometric structures were optimized until the remaining force acting on the atoms becomes smaller than 0.005 Ryd/Å.

5.2.5. Device fabrication and measurement

As the CVD process slightly damages the surface SiO_2 layer and gave gate leakage, the as-grown WSe_2 grains were transferred onto a fresh SiO_2(90 nm)/Si substrate using polystyrene as a support layer.[37] Prior to the transfer, the SiO_2 /Si substrates were cleaned by sonicating in acetone and isopropyl alcohol for 10 minutes each. For the fabrication of FETs, the transferred WSe_2 was spin-coated by photoresist and patterned using photolithography, followed by electron beam evaporation of Au(30 nm)/Ni(1 nm)

electrodes (Kennix KB-750) and lift-off process. Carrier transport properties were measured using a semiconductor parameter analyzer (Keysight Technologies B1500A) in vacuum (~10^{-4} Pa) at room temperature. To fabricate the inverter circuit, two WSe_2 FETs were externally connected by Au wire (99.95 %, 300 μm in diameter). The inverter performance was also measured in a vacuum (~10^{-4} Pa) at room temperature. For measuring the optical response of a p-n device, a 532 nm laser (Showa Optronics Co.) was used together with ND filters for controlling the laser power.

5.3. Results and Discussion

5.3.1. CVD growth and chemical doping of WSe_2

Figure 5.1 shows the experimental procedure employed to prepare p- and n-doped WSe_2. As written in the experimental section, triangular grains of monolayer WSe_2 were synthesized on SiO_2/Si substrates by thermal CVD using WO_3 and Se precursors. An optical microscope image of the as-grown WSe_2 is shown in Figure 5.1b. To avoid gate leakage, the as-grown WSe_2 was transferred to a fresh SiO_2 (90 nm)/Si substrate.[37] After the transfer, FETs with WSe_2 channels were fabricated by photolithography, Ni/Au electrode deposition, and lift-off processes.

For the p-type doping, WSe_2 was immersed in aqueous solution of 4-NBD (Figure 5.1c), while WSe_2 was exposed to DETA vapor for the n-type doping (Figure 5.1d). AFM images of pristine, 4-NBD and DETA doped WSe_2 grains are shown in Figure 5.2, where the monolayer thickness (~1 nm) and dopant deposition can be seen from the height profile. The as-grown, pristine WSe_2 had a thickness of ~ 1 nm and showed an intense PL at 760 nm, reflecting the direct band gap nature. These results confirm the

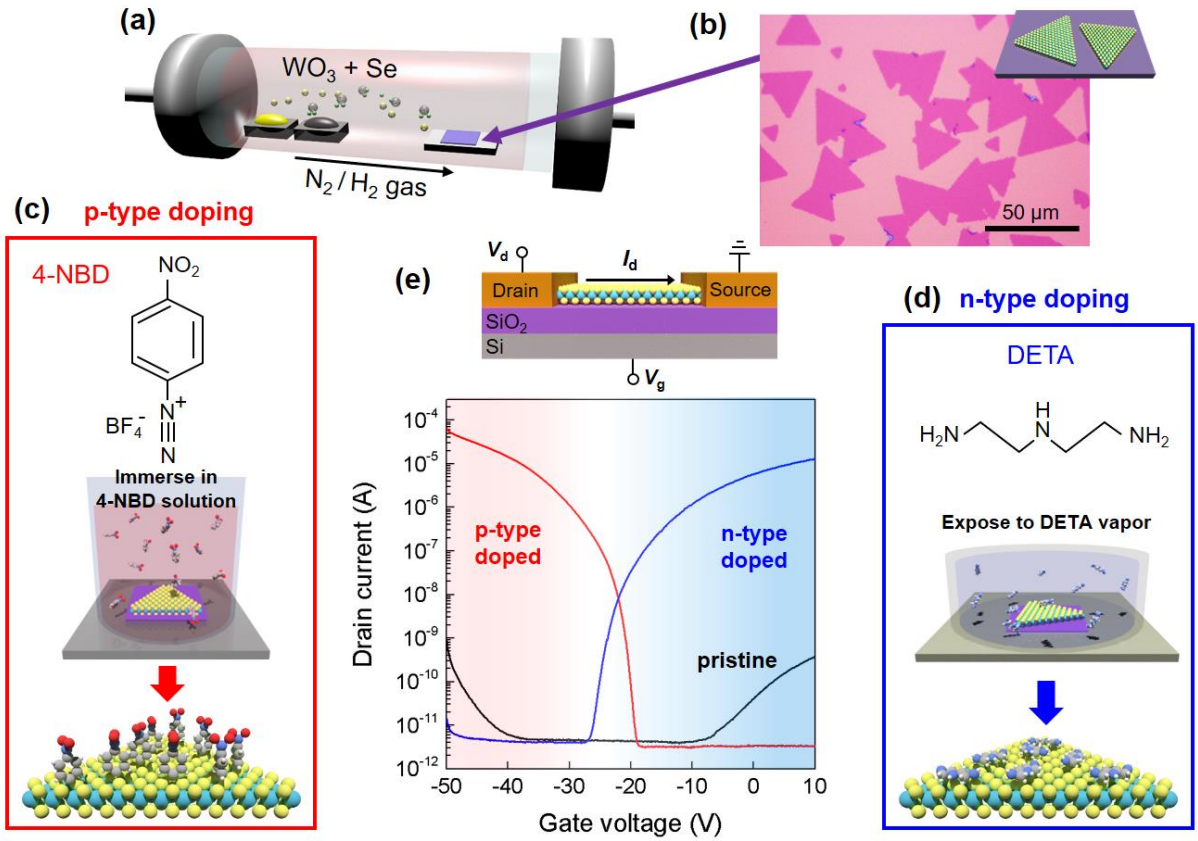

Figure 5.1. (a) Schematic of CVD growth of WSe_2 on SiO_2/Si substrate. (b) Optical micrograph of as-grown triangular WSe_2 grains. (c,d) Chemical doping processes using 4-NBD and DETA molecules for p- and n-type doping, respectively. (e) Transfer curves of pristine (black) and 4-NBD doped (red) and DEA doped (blue) WSe_2 measured with $V_d = 5$ V.

growth of monolayer WSe_2. Figure 5.1e shows the device structure of WSe_2-FET and the corresponding transfer characteristics measured before and after the chemical doping. Drain current (I_d) was measured as a function of gate voltage (V_g) applied from back side of the device through a SiO_2 layer. The pristine WSe_2 (black curve) showed ambipolar behavior with a slightly n-doped character. After the contact with 4-NBD and DETA dopants, the WSe_2 device changed to p- (red curve) and n-type (blue curve), respectively. The V_{th} shifted to more positive (p-doped) and more negative (n-doped) voltages after each doping. This implies that holes and electrons are

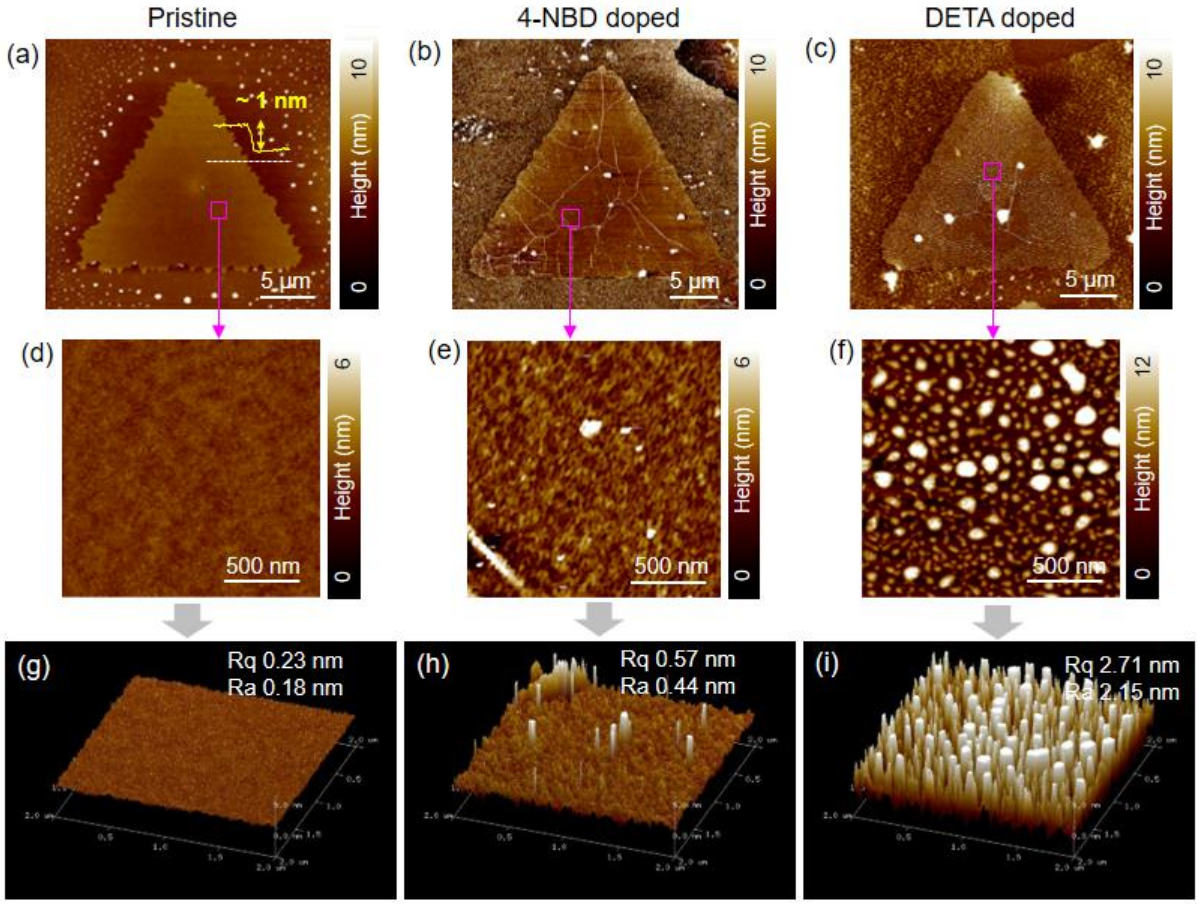

Figure 5.2. AFM height images of pristine (a), 4-NBD doped (b), and DETA doped (c) WSe_2 grains. (d-f) Magnified images of the marked positions. (g-i) Three-dimensional AFM images of those shown in (d-f).

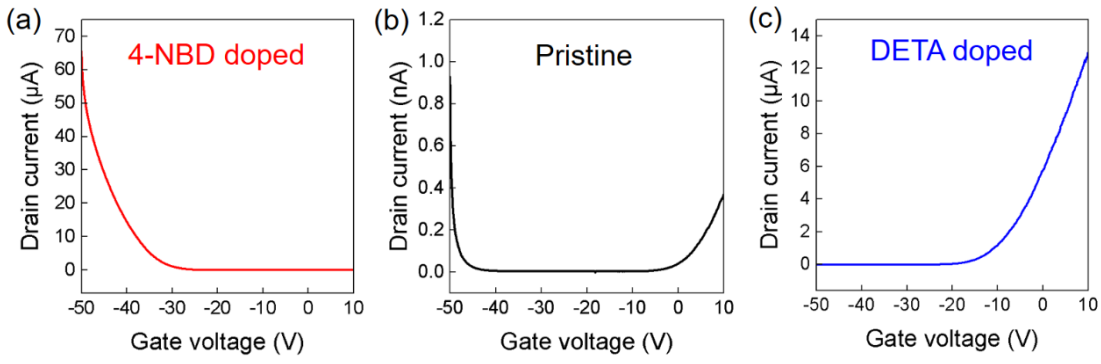

Figure 5.3. Transfer characteristics of WSe_2 FETs before doping (b) and after doping with 4-NBD (a) and DETA (c) with y-axis linear scale. Drain voltage is 5 V, and SiO_2 thickness is 90 nm.

accumulated not only by the gate voltage but also by the chemical doping effect. The transfer curves with linear scale of the drain current are shown in Figure 5.3.

5.3.2. Electrical transport properties after doping

It is noted that the slopes of the transfer curve after the doping are much steeper than those of the undoped devices (see Figure 5.1e, in which *y*-axis scale is logarithmic). Figure 5.4a,b shows more detailed analysis of the carrier transport of the doped WSe_2 monolayers. To avoid device-to-device variations, I measured the electrical transport of the same WSe_2 channels before and after the doping process. Because the V_{th} are different for the pristine and doped WSe_2 samples, the overdrive gate voltage (V_g-V_{th}) was used in the graphs for better comparison of the gate voltage dependence. The effective field-effect carrier mobility (μ) was calculated by using the following equation:

$$\mu = \frac{g_m}{C_{ox} V_d} \frac{L}{W} \tag{5.1}$$

where $g_m = dI_d/dV_g$ is the transconductance obtained from the transfer curve; C_{ox} = 38.3 $nFcm^{-2}$ is the capacitance per unit area of the 90 nm-thick SiO_2; V_d is the applied drain voltage; L and W represent the effective length and width of the channel. The effective carrier mobility was calculated by assuming a trapezoidal channel shape to take into account the geometrical effect. It is seen that the carrier mobility after the doping with both 4-NBD and DETA increased by more than 3-4 orders of magnitude.

Figure 5.4c compares the effective carrier mobilities of WSe_2 devices (20 devices were measured for each dopant). The measured hole and electron mobilities of the pristine WSe_2 were found to be rather low. This can originate in intrinsic defects in

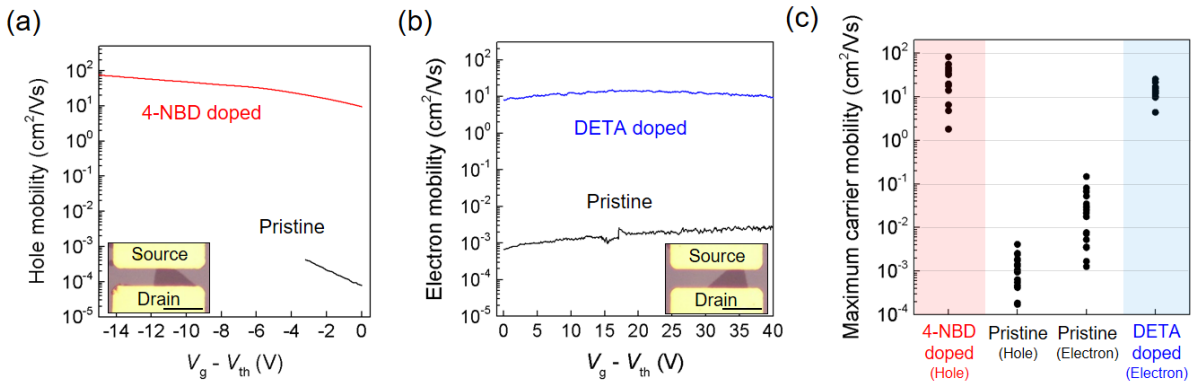

Figure 5.4. (a,b) Carrier mobilities of pristine (black) and doped (red and blue) WSe_2 devices plotted as a function of the overdrive gate voltage. The doping-induced change of the carrier mobility is shown by green curve. Insets show the optical images of the devices (scale bar: 20 μm). (c) Distributions of maximum hole and electron mobilities of pristine and doped WSe_2.

the as-grown WSe_2 grains, degradation due to air exposure, and/or possible damages induced by the device fabrication process, as based on our experience WSe_2 is easier to be oxidized than MoS_2 and WS_2. Interestingly, both the hole and electron mobilities drastically increased after the chemical doping, as can be seen in Figure 5.4c. The maximum carrier mobilities measured after the p- and n-type doping were 82 $cm^2\ V^{-1}s^{-1}$ (for holes) and 25 $cm^2\ V^{-1}s^{-1}$ (for electrons), respectively. It is speculated that influence of defects existing in WSe_2 is reduced by the chemical doping due to increased carrier concentration, contributing to the increase of the measured carrier mobilities. In addition, lowering the Schottky barrier height due to the chemical doping-induced Fermi level shift should be considered as another source of the increased effective carrier mobility. In previous literatures,[23,38–41] it has been proposed that the interface between the 2D material and the electrode plays an important role in the carrier transport due to strong modification of the Fermi level of the 2D material. Thus, it is highly likely that reduction of the contact resistance induced by the chemical doping largely contributes to the increased carrier mobility of WSe_2 FETs. The enhanced carrier

mobilities together with the polarity control would allow prospective use for high mobility switching devices.

5.3.3. Spectroscopy and DFT calculations

Figures 5.5a,b compare the PL spectra of monolayer WSe_2 before and after the doping with 4-NBD and DETA, respectively. The 4-NBD doping was found to increase the PL intensity and decrease the FWHM from 64 to 53 meV. The PL peak from the pristine WSe_2 can be deconvoluted with exciton and trion peaks located at ~1.64 eV and ~1.59 eV, respectively, as shown in Figure 5.6. As reported previously, it is considered that the trion in the pristine WSe_2 is a negative trion (A^-),[42] being consistent with the experimental observation that electrons are main charge carriers in the absence of a gate voltage (see Figure 5.1e). The 4-NBD doping increased the intensity of the exciton peak while reduced that of the trion (Figures 5.5a and 5.6a). The increased exciton peak can be accounted for by the reduction of the negative charges due to the supply of holes from 4-NBD, resulting in the decreased ratio of negative trions. The trion peak in the doped WSe_2 can be either remaining negative trions or newly formed positive

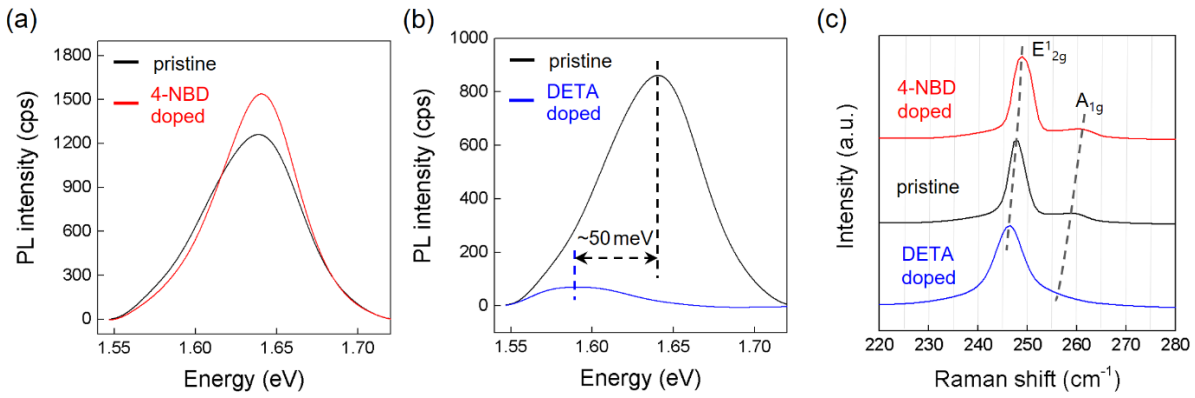

Figure 5.5. (a,b) PL spectra of pristine and doped WSe_2 measured on SiO_2/Si substrates. The identical WS_2 grains were used to monitor the doping-induced spectrum change. (c) Raman spectra of pristine and doped WSe_2.

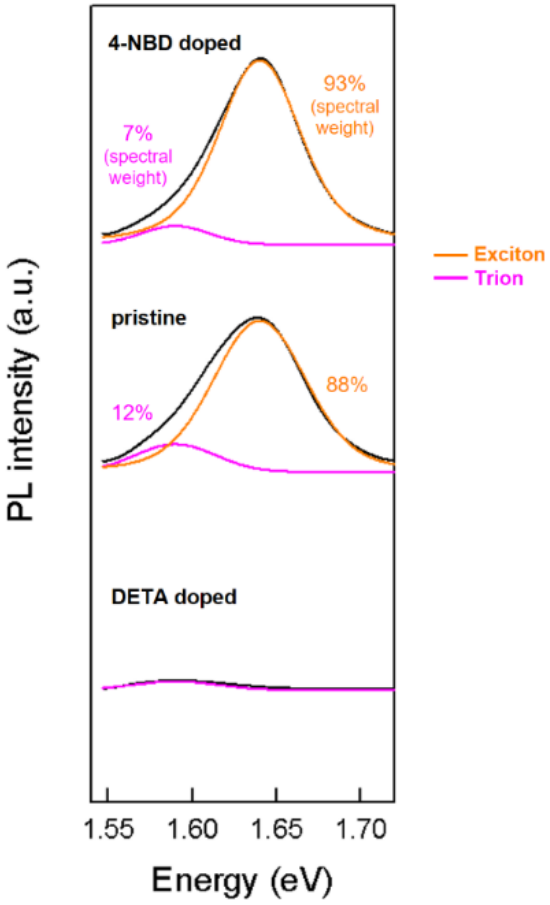

Figure 5.6. Peak fitting analysis of the PL spectra of the pristine and doped WSe_2. The original PL spectra are displayed in Figure 5.5a,b. Orange and magenta curves correspond to exciton and trion peaks, respectively.

trions. Although the origin of the trion peak is unclear, the PL spectra supports the hole doping to the WSe_2 induced by 4-NBD molecules.

The DETA doping gave a completely different change in the PL spectrum (Figure 5.5b). The PL peak was strongly suppressed and red-shifted by ~50 meV. The fitting analysis indicates that the spectral weight of the trion peak increased, while the exciton peak decreased significantly (see Figure 5.6). This can be explained by the increased concentration of negative trions, while preventing the formation of neutral excitons as a result of electron doping.[29,43] In this case, the observed trion peak should be originated

in the negative trions. The observed peak shift of ~50 meV after the DETA doping corresponds to the trion binding energy of WSe_2.[44,45]

Effects of the chemical doping on the Raman spectrum were also studied, as shown in Figure 5.5c. The E^1_{2g} band which corresponds to the in-plane vibration mode clearly shifted to higher and lower wavenumbers upon 4-NBD and DETA doping, respectively. The position of the out-of-plane mode (A_{1g} band) exhibited a similar tendency. Such doping-induced Raman shift is consistent with previous studies,[46,47] and can be explained by the change of the electron density in monolayer WSe_2; the n-type doping increases the electron-phonon scattering due to a higher electron concentration, while the p-type doping decreases the electron-phonon scattering.[46,47] The decrease of the A_{1g} peak intensity is also in accordance with the existing literature.[19,46] Thus, the Raman spectroscopy also supports the p/n selective doping in our CVD-grown WSe_2.

For further understanding of the changes of the WSe_2 electronic structure induced by 4-NBD and DETA molecules as well as the charge transfer phenomena, XPS measurement and DFT calculations were performed. Figure 5.7a,b shows XPS W_{4f} and Se_{3d} spectra of the pristine and the doped WSe_2. The chemical doping with 4-NBD molecule shifted the binding energies of both W_{4f} and Se_{3d} peaks to lower energies (see Figure 5.7c for the XPS peak positions). This shift implies that the Fermi level of the WSe_2 is moved downward to the valence band edge. On the other hand, the DETA doping increased the binding energies of both W_{4f} and Se_{3d} peaks, suggesting the shifting of the Fermi energy upward to the conduction band edge. These observed energy shifts are consistent with the previous literatures reporting the selective p/n-doping to MoS_2.[29,48,49] Therefore, the changes of the binding energies after the 4-NBD and DETA adsorption qualitatively supports the p-/n-selective doping by tuning the Fermi energy of the monolayer WSe_2.

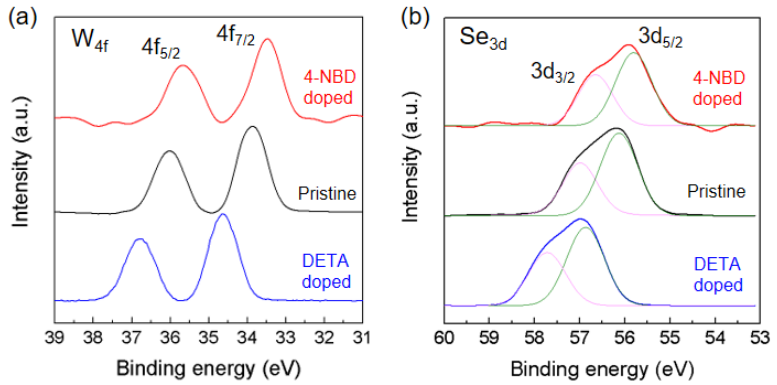

(c)

	W_{4f} peak		Se_{3d} peak	
	$4f_{5/2}$	$4f_{7/2}$	$3d_{3/2}$	$3d_{5/2}$
4-NBD doped	35.7 (-0.4)	33.5 (-0.4)	56.6 (-0.4)	55.8 (-0.4)
Pristine	36.1	33.9	57	56.2
DETA doped	36.8 (+0.7)	34.6 (+0.7)	57.7 (+.07)	56.9 (+0.7)

Figure 5.7. (a,b) XPS spectra (W_{4f} and Se_{3d}) of pristine and doped WSe_2. (c) XPS peak positions of pristine and doped WSe_2 (in eV). The number in the parenthesis indicates the relative peak position with respect to the pristine WSe_2. Note that the energy shift is dependent on the degree of doping (or amount of dopant).

Figures 5.8a,b display the energy levels of WSe_2, 4-NBD, and DETA, as determined by the DFT calculations. In the case of 4-NBD, the diazonium molecule forms a complex with BF_4^- anion.[50] Therefore, in the present calculation, the diazonium molecule is assumed to possess a singly occupied molecular orbital (SOMO) located between the highest occupied molecular orbital (HOMO) and the lowest unoccupied molecular orbital (LUMO). As seen in Figure 5.8a, the relative position of SOMO of 4-NBD and valence band edge (VBE) of WSe_2 supports the hole doping in WSe_2 via the electrons transfer to the SOMO.

DETA molecule has a closed-shell electronic structure and its HOMO locates within the band gap of pristine, monolayer WSe_2 (see Figure 5.8b for the band energy of the pristine WSe_2). However, the HOMO level is ~1.59 eV below the conduction band edge (CBE) of WSe_2 (Figure 5.8b). It is thought that there are several mechanisms

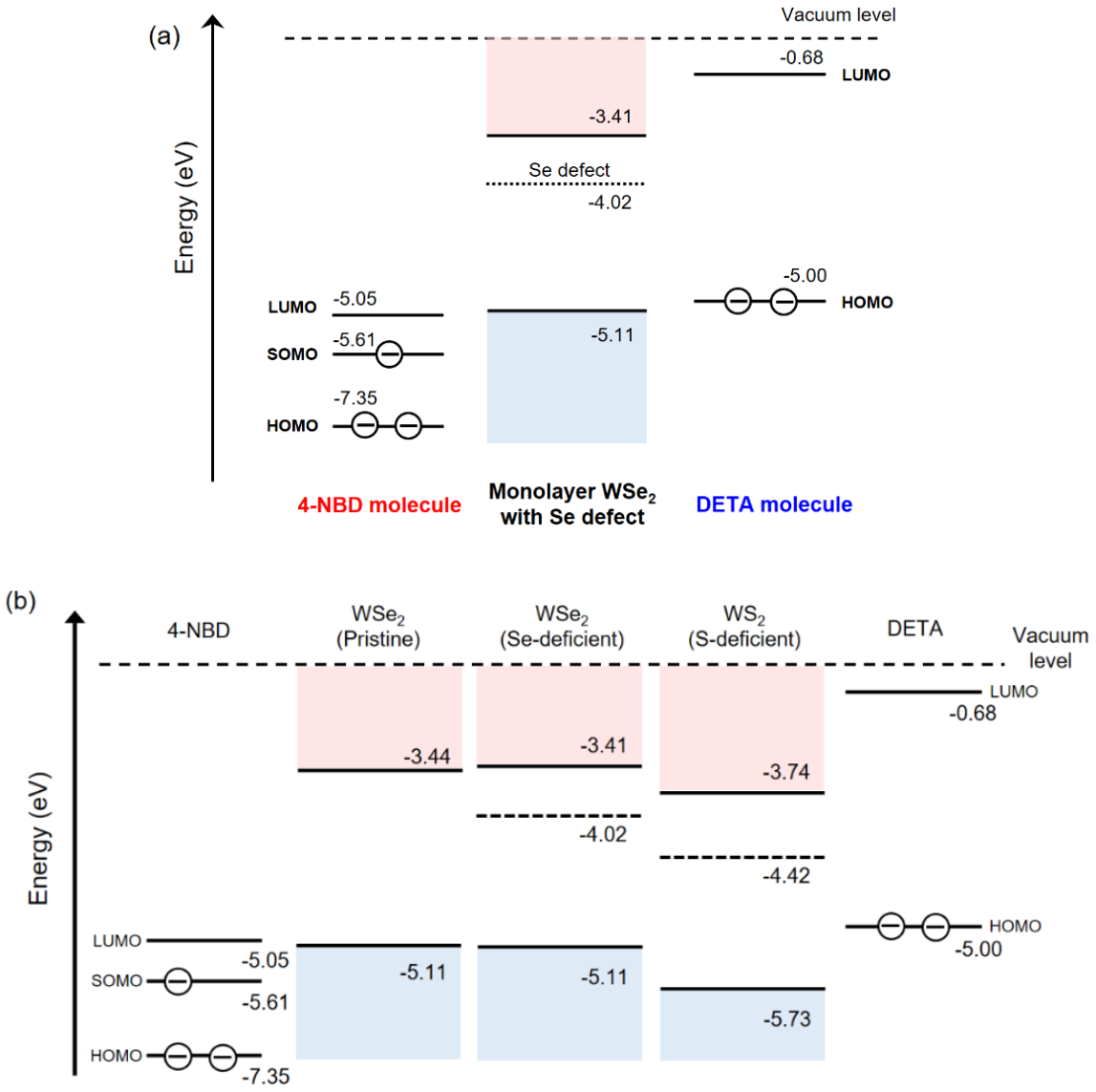

Figure 5.8. (a) Band diagram of pristine WSe_2, 4-NBD and DETA molecules. The energy levels were calculated by DFT. (b) Molecular orbital levels of 4-NBD and DETA molecules, and band structures of pristine WSe_2, Se-deficient WSe_2, and S-deficient WS_2 monolayers. Broken lines show newly appeared defect states. The energy levels were calculated by the DFT.

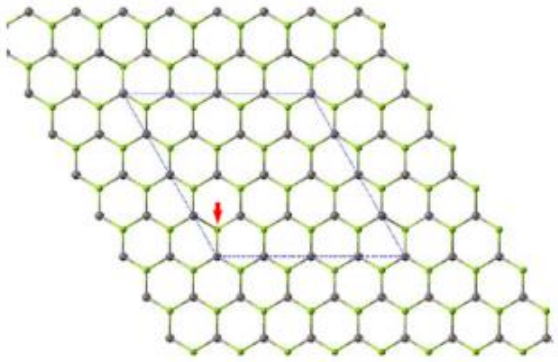

Figure 5.9. Atomic model of WSe_2 monolayer with single Se vacancy (indicated by the arrow) in 4×4 cell, which is used to calculate the defect-related band structure shown in Figures 5.8a,b. The Se vacancy is introduced to the upper Se site of the monolayer WSe_2. Green and gray atoms represent Se and W, respectively.

which assist the electron transfer from DETA to WSe_2. First, Se vacancies are frequently observed in WSe_2 samples,[51] which can be the origin of the relatively low effective carrier mobility observed in our pristine WSe_2 (see Figure 5.4c). Therefore, in Figure 5.8a, the band structure of the monolayer WSe_2 containing Se vacancies (one Se atom was removed from 4×4 unit cell, which corresponds to ~3% Se vacancy (see Figure 5.9 for the atomic structure)) is displayed. As seen in Figure 5.8a, the introduction of Se vacancies produced a new state, which is associated with the defect, at 0.61 eV below the CBE. This defect state is expected to act as an intermediate trap state through which the electrons transfer from DETA to WSe_2, thus assisting the n-type doping. Although the exact density of structural defects including Se vacancies is not clear, the post-growth treatment, such as exposure to ambient and the device fabrication process, may give more defects with variety of defect structures. It is noted that a STEM study revealed the presence of various crystal defects in monolayer MoS_2, suggesting the formation of localized electronic states within the band gap.[52] Other DFT calculations also indicated the formation of a defect state (or in-gap state) within the band gap when chalcogen vacancies are introduced in MoS_2 and $MoSe_2$.[53,54] Therefore, it is speculated that there is a possibility that the defect-related bands appear just above the HOMO level of DETA or close to the HOMO level, which can account for the experimentally observed n-type doping. The second possibility is the coordination of paired electrons of N atoms in DETA to W atoms of WSe_2, introducing the charge transfer to WSe_2. As this model is also based on the presence of Se vacancies to access a W metal, we speculate that the imperfect WSe_2 structure is related to the observed n-type doping induced by DETA molecules.

To support our interpretation of the doping mechanism in WSe_2, I also treated monolayer WS_2 with 4-NBD and DETA for the sake of comparison. The PL spectral

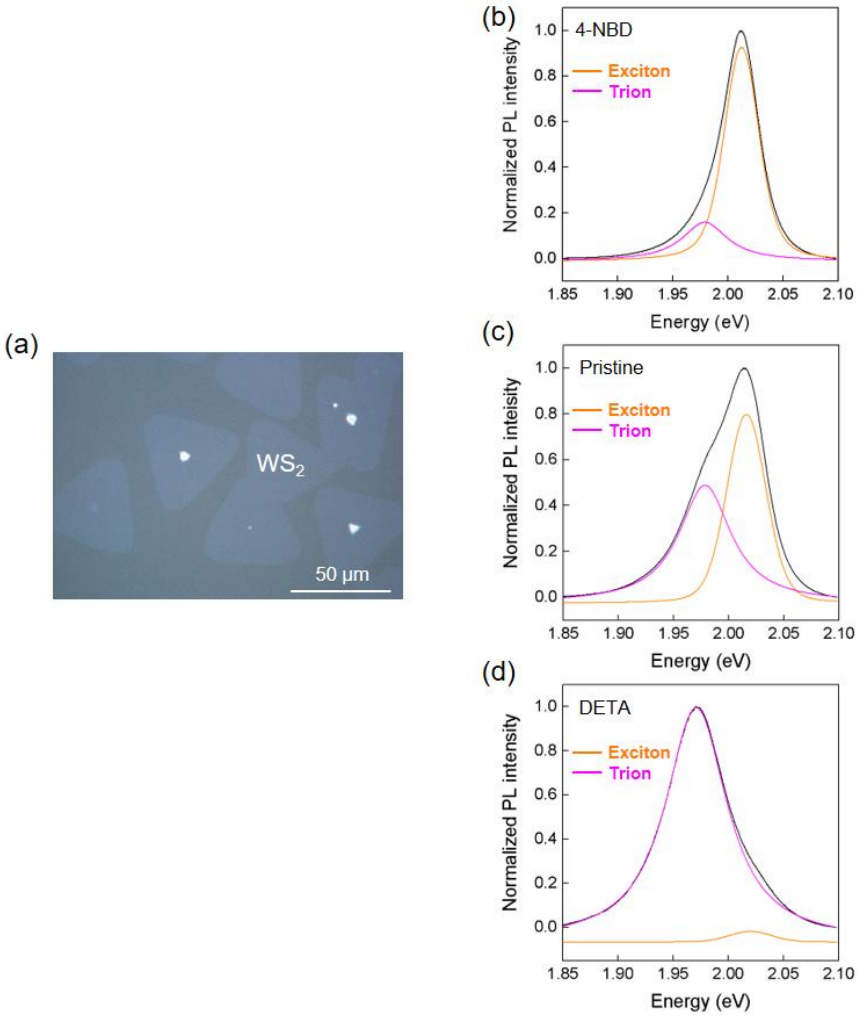

Figure 5.10. Investigation of chemical doping effect on WS_2 by PL analysis. (a) An optical micrograph of CVD-grown WS_2 on sapphire substrate. PL spectra of 4-NBD doped (b), pristine (c), and DETA doped (d) WS_2. Black curves are measured spectra, while orange and magenta curves are fitted curves which correspond to exciton and trion peaks.

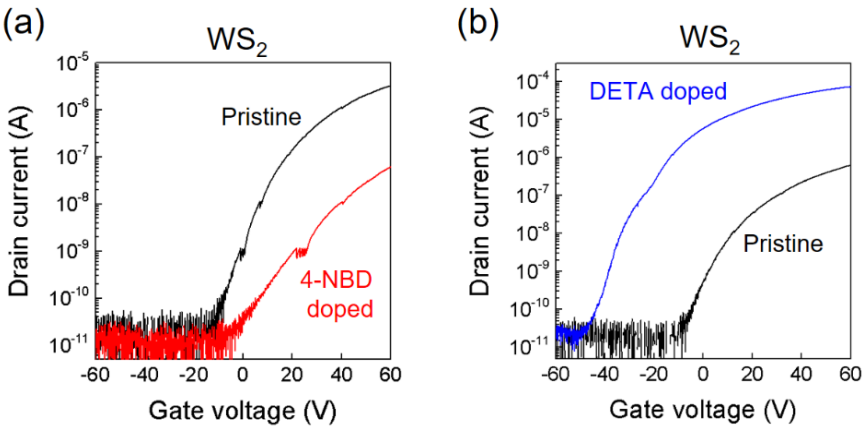

Figure 5.11. Transfer characteristics of WS_2 FETs before and after doping with 4-NBD (a) and DETA (b). V_d = 1V, SiO_2 thickness is 300 nm.

change is presented in Figure 5.10. A similar tendency was observed for monolayer WS_2, with an increased ratio of the exciton peak after 4-NBD doping, and the significant increase of the trion peak after DETA doping.[55,56] As shown in Figure 5.11a, the WS_2 FET showed the shift of V_{th} to positive gate voltages after dipping in 4-NBD solution, but it did not show p-type transport character. According to DFT calculations (see Figure 5.8b), the VBE of WS_2 is located below the SOMO of 4-NBD, making it difficult to inject holes from 4-NBD to WS_2. This is consistent with the FET result in which clear p-type transfer characteristics was not observed in 4-NBD doped WS_2 system (see Figure 5.11a). The exposure to DETA vapor shifted the V_{th} of WS_2 to negative voltages, indicating the n-type doping (Figure 5.11b). This agrees with the calculated band structure, as the defect state of WS_2 is closer to the HOMO level of DETA than the defect state of WSe_2 (see Figure 5.8b). Our experimental and theoretical results indicate that monolayer WSe_2 is suitable for obtaining clear p/n selective doping with the employed dopant molecules.

Previously, formation of a covalent bond was proposed between a 4-NBD molecule and monolayer TMD,[57,58] similar to the case of graphene and 4-NBD.[50] In the case of graphene, the covalent bond formation can be recognized from the appearance of defect-related Raman D-band. However, as the Raman spectrum of TMDs is not so sensitive to defects or covalent bond formation, it is difficult to experimentally discuss how the dopant molecules attach on the WSe_2. The p-doping effect in the 4-NBD doped WSe_2 was still observed after thorough washing with water, while n-type doping effect by DETA disappeared easily after washing with water. Thus, there is a possibility of chemisorption and physisorption for 4-NBD and DETA doping, respectively. However, the XPS spectra of 4-NBD doped WSe_2 (Figure 5.7a,b) did not show any apparent changes in the peak shapes except for shift of the peak positions to lower

binding energies. There is no solid evidence for the possible chemisorption of 4-NBD molecules on WSe_2 surface. Therefore, further study is necessary to understand the detailed doping mechanism by employing atomic scale imaging techniques, such as transmission electron microscope (TEM) and scanning tunneling microscope (STM).

5.3.4. Fabrication of a CMOS inverter

The controlled p- and n-type doping in WSe_2 was developed to fabricate a CMOS inverter. Figure 5.12a shows the input voltage (V_{in}) dependence of the output voltage (V_{out}) collected with different supply voltages (V_d). Here, the p- and n-FETs were externally connected in series by an Au wire to form the inverter, with the common back-gate being the input (V_{in}) (See Figure 5.12a inset). As can be seen in Figure 5.12a, the V_{in} signal was properly inverted. The V_{out} was kept at a value of V_d for V_{in} lower than ~ -28 V and dropped to ~0 V for V_{in} higher than ~-25 V, with a sharp inversion. Figure 5.12b shows the voltage gain, defined as $V_{gain} = -dV_{out}/dV_{in}$, which is one of the most important performance parameters of CMOS inverters. As can be expected from the sharp transition of V_{out} (Figure 5.12a), a maximum V_{gain} as high as 10 was achieved.

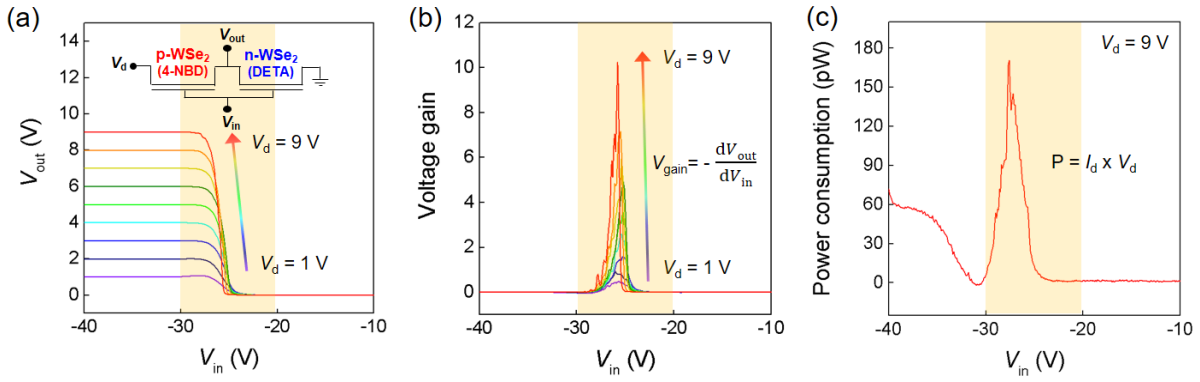

Figure 5.12. CMOS inverter operated with p- and n-doped WSe_2. (a) V_{out} plotted as a function of V_{in}. Inset shows the circuit diagram of the inverter. (b,c) Voltage gain and power consumption of the CMOS inverter.

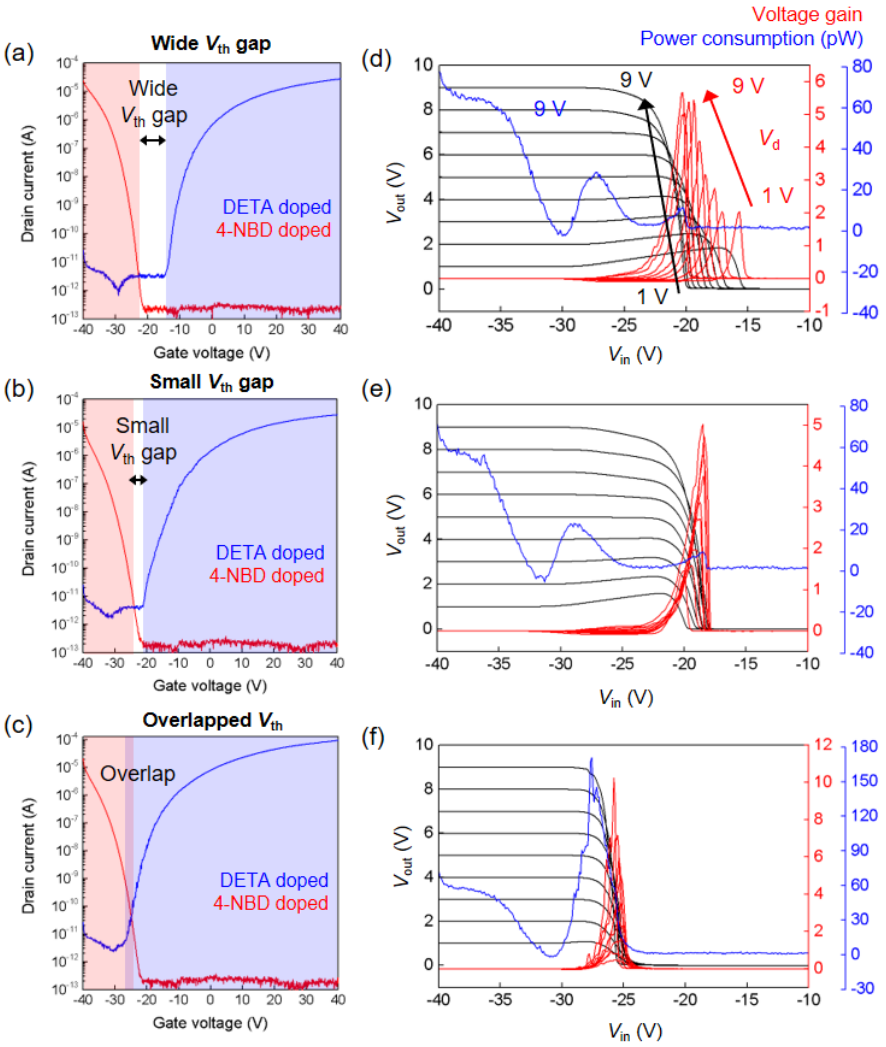

Figure 5.13. Detailed study of inverter performance. (a-c) Transfer characteristics of 4-NBD and DETA doped WSe_2. The gap between V_{th} of two transfer characteristics is the largest in (a) and smallest in (c). (d-f) Inverter performance corresponding to (a-c).

To the best of my knowledge, this is the first report of a CVD-grown WSe_2 CMOS inverter where both p- and n-channels are formed by respective doping treatments.[13,26,59–63] Considering that this CMOS circuit was fabricated on a SiO_2 (90 nm)/Si substrate with a back-gate geometry (C_{ox} = 38.3 nF cm^{-2}), the obtained gain can be further improved by increasing the capacitance via top-gate operation for a more effective switching control.[13,23]

One of the biggest benefits of CMOS circuits is their low power operation. Figure 5.12c shows the power consumption of the WSe_2-based inverter as a function of the input voltage. I found that my inverter can operate with an extremely low power consumption of ~170 pW. This value is three orders of magnitude lower than those from previous references using TMD channels.[13,26,59] I attribute this low power consumption to the optimized overlap of the transfer curves of p- and n-FETs, allowing to keep the current flow through the inverter low. As shown in Figure 5.13, the power consumption of my inverters increased with increasing the overlap of the transfer curves of p- and n-FETs. Liu *et al*. reported 1 μW power consumptions when the transfer curves of the individual FETs overlap at a drain current of ~1000 nA.[62] Zhang *et al.* reported 3.1 nW power consumptions when the overlap of the individual FETs transfer curves occurs at 1 nA.[59] In contrast, my p- and n-FETs overlapped at ~0.1 nA, thus efficiently minimizing the leakage current to prevent the power loss. Therefore, controlled doping through the optimization of the exposure time and dopant concentration is required for both p- and n-type WSe_2 to achieve low power CMOS inverters.

5.3.5. Fabrication of a p-n junction

For practical applications of TMD materials in electronic and optoelectronic devices, the p-n junction is the most important and basic working unit. Therefore, I fabricated a p-n junction within a single WSe_2 grain through spatially controlled p- and n-doping. The fabrication process is depicted in Figure 5.14. In brief, 4-NBD doping was performed through a photoresist window, followed by deposition of SiO_2 as a protective layer. Then, another window is opened in the SiO_2 layer for the successive DETA doping. Figures 5.15a,b show a false colored optical image and the corresponding

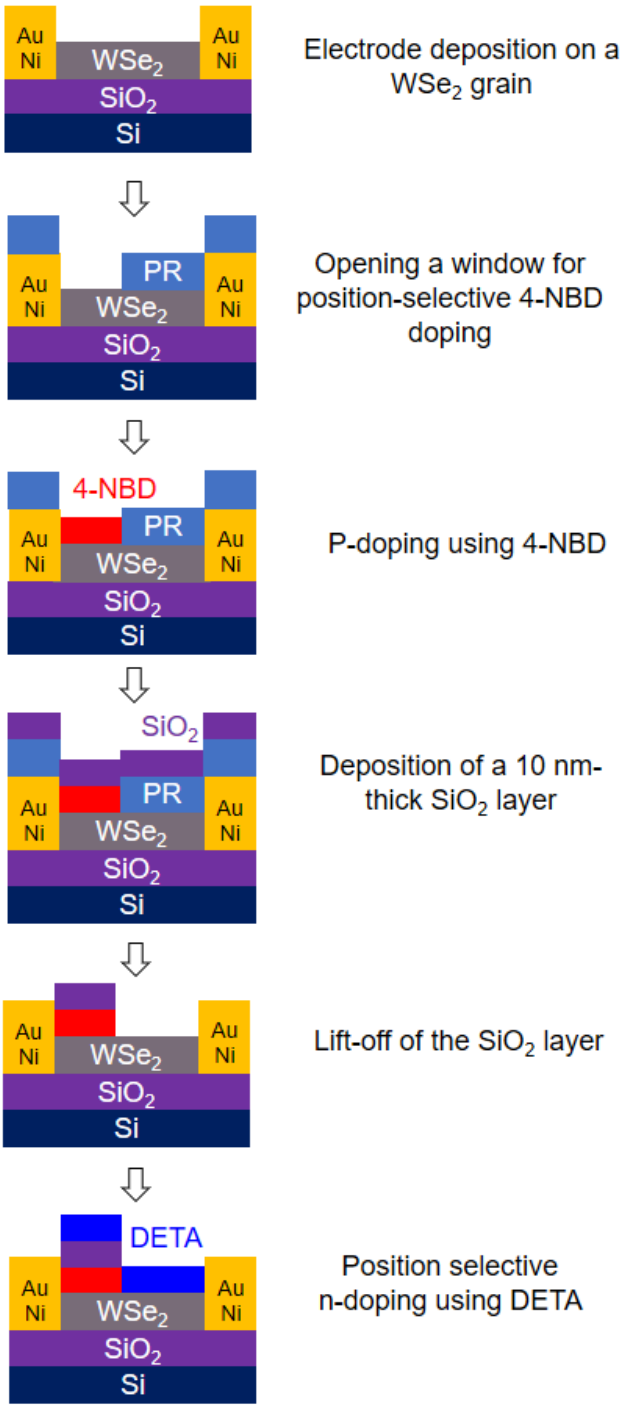

Figure 5.14. Fabrication process of the spatially controlled p-n junction in single WSe_2 grain. PR is photoresist.

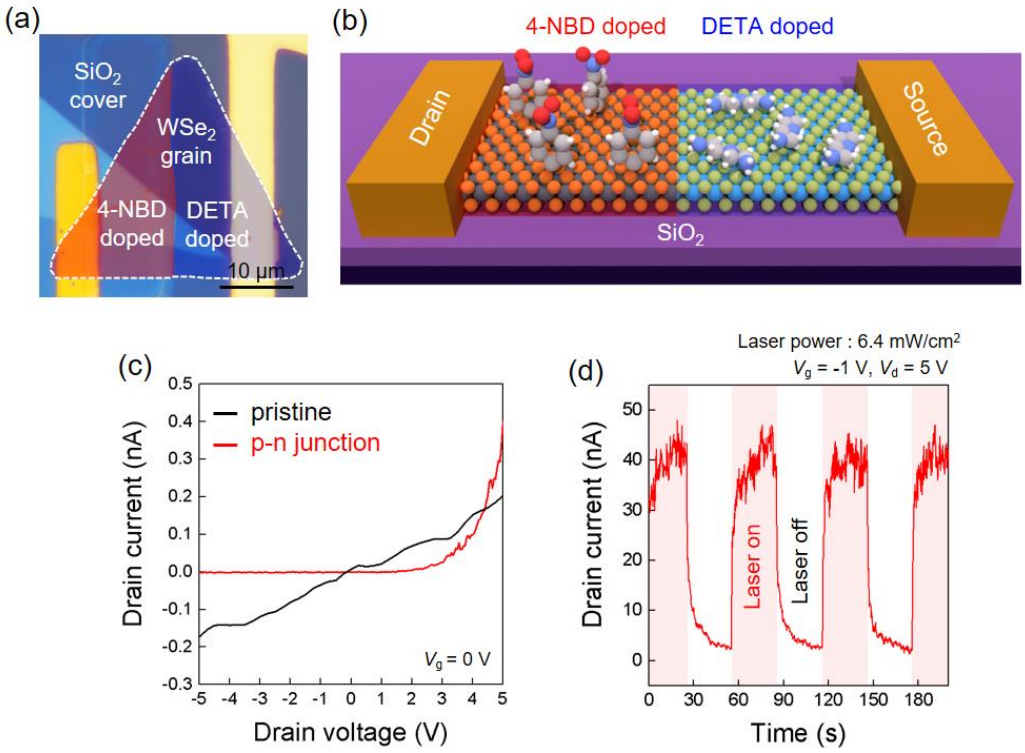

Figure 5.15. (a,b) Optical micrograph and schematic of a p-n junction made by the spatially controlled p/n doping within single WSe_2 grain. (c) Output curves of the pristine and p/n doped WSe_2 monolayer device. The device with p-n junction shows clear rectification behavior. (d) Light response of the WSe_2 device with p-n junction.

schematic model of the p-n doped single grain device fabricated in this work. Output characteristics of the WSe_2 before and after the formation of the p-n junction are shown in Figure 5.15c. While the pristine WSe_2 grain exhibited an almost linear I_d-V_d curve with high resistivity (black curve), after the spatially controlled p-n doping, the device showed a clear rectifying behavior (red curve). Such asymmetric transport behavior is a strong evidence of the formation of a p-n junction.[30,31,64] Under illumination with visible light (532 nm, 6.4 $mWcm^{-2}$), I observed a clear photoresponse (Figure 5.15d), demonstrating its potential in photodetection applications.

5.4. Conclusions

In this chapter, the effective and controlled chemical doping of CVD-grown WSe_2 was demonstrated. Spectroscopic analyses and DFT calculation proved that 4-NBD and DETA molecules allow efficient charge transfer to WSe_2, changing the ambipolar WSe_2 to p- and n-type semiconductors, respectively. The chemical doping with 4-NBD and DETA was found to significantly improve the effective carrier mobilities of both holes and electrons. The integration of the p- and n-type WSe_2 was also demonstrated for the operation of a low power CMOS inverter, originating from the high control of the degree of the doping. Moreover, the position selective doping has been developed to obtain the p-n junction within a single WSe_2 grain. The p-n doped WSe_2 grain showed clear rectification behavior and optical response, as required for optoelectronics applications. This chemical doping strategy can offer a versatile approach to modify the electrical property of TMD materials for various device applications.

References

(1) Zhu, Z. Y.; Cheng, Y. C.; Schwingenschlögl, U. Giant Spin-Orbit-Induced Spin Splitting in Two-Dimensional Transition-Metal Dichalcogenide Semiconductors. *Phys. Rev. B* **2011**, *84*, 153402.

(2) Wang, Q. H.; Kalantar-Zadeh, K.; Kis, A.; Coleman, J. N.; Strano, M. S. Electronics and Optoelectronics of Two-Dimensional Transition Metal Dichalcogenides. *Nat. Nanotechnol.* **2012**, *7*, 699–712.

(3) Cheiwchanchamnangij, T.; Lambrecht, W. R. L. Quasiparticle Band Structure Calculation of Monolayer, Bilayer, and Bulk MoS_2. *Phys. Rev. B* **2012**, *85*, 205302.

(4) Kang, K.; Xie, S.; Huang, L.; Han, Y.; Huang, P. Y.; Mak, K. F.; Kim, C.-J.; Muller, D.; Park, J. High-Mobility Three-Atom-Thick Semiconducting Films with Wafer-Scale Homogeneity. *Nature* **2015**, *520*, 656–660.

(5) McCreary, K. M.; Hanbicki, A. T.; Jernigan, G. G.; Culbertson, J. C.; Jonker, B. T. Synthesis of Large-Area WS_2 Monolayers with Exceptional Photoluminescence. *Sci. Rep.* **2016**, *6*, 19159.

(6) Smithe, K. K. H.; Suryavanshi, S. V.; Muñoz Rojo, M.; Tedjarati, A. D.; Pop, E. Low Variability in Synthetic Monolayer MoS_2 Devices. *ACS Nano* **2017**, *11*, 8456–8463.

(7) Aji, A. S.; Solís-Fernández, P.; Ji, H. G.; Fukuda, K.; Ago, H. High Mobility WS2 Transistors Realized by Multilayer Graphene Electrodes and Application to High Responsivity Flexible Photodetectors. *Adv. Funct. Mater.* **2017**, *27*, 1703448.

(8) Kim, H.; Ahn, G. H.; Cho, J.; Amani, M.; Mastandrea, J. P.; Groschner, C. K.; Lien, D.-H.; Zhao, Y.; Ager, J. W.; Scott, M. C.; Chrzan, D. C.; Javey, A. Synthetic WSe_2 Monolayers with High Photoluminescence Quantum Yield. *Sci. Adv.* **2019**, *5*, eaau4728.

(9) Jariwala, D.; Sangwan, V. K.; Lauhon, L. J.; Marks, T. J.; Hersam, M. C. Emerging Device Applications for Semiconducting Two-Dimensional Transition Metal Dichalcogenides. *ACS Nano* **2014**, *8*, 1102–1120.

(10) Tsai, M.-L.; Su, S.-H.; Chang, J.-K.; Tsai, D.-S.; Chen, C.-H.; Wu, C.-I.; Li, L.-J.; Chen, L.-J.; He, J.-H. Monolayer MoS_2 Heterojunction Solar Cells. *ACS Nano* **2014**, *8*, 8317–8322.

(11) Yang, W.; Shang, J.; Wang, J.; Shen, X.; Cao, B.; Peimyoo, N.; Zou, C.; Chen, Y.; Wang, Y.; Cong, C.; Huang, W.; Yu, T. Electrically Tunable Valley-Light Emitting Diode (VLED) Based on CVD-Grown Monolayer WS_2. *Nano Lett.* **2016**, *16*, 1560–1567.

(12) Wachter, S.; Polyushkin, D. K.; Bethge, O.; Mueller, T. A Microprocessor Based on a Two-Dimensional Semiconductor. *Nat. Commun.* **2017**, *8*, 14948.

(13) Pu, J.; Funahashi, K.; Chen, C.-H.; Li, M.-Y.; Li, L.-J.; Takenobu, T. Highly Flexible and High-Performance Complementary Inverters of Large-Area Transition Metal Dichalcogenide Monolayers. *Adv. Mater.* **2016**, *28*, 4111–4119.

(14) Carozo, V.; Wang, Y.; Fujisawa, K.; Carvalho, B. R.; McCreary, A.; Feng, S.; Lin, Z.; Zhou, C.; Perea-López, N.; Elías, A. L.; Kabius, B.; Crespi, V. H.; Terrones, M. Optical Identification of Sulfur Vacancies: Bound Excitons at the Edges of Monolayer Tungsten Disulfide. *Sci. Adv.* **2017**, *3*, e1602813.

(15) Ji, H. G.; Lin, Y.-C.; Nagashio, K.; Maruyama, M.; Solís-Fernández, P.; Sukma Aji, A.; Panchal, V.; Okada, S.; Suenaga, K.; Ago, H. Hydrogen-Assisted Epitaxial Growth of Monolayer Tungsten Disulfide and Seamless Grain Stitching. *Chem. Mater.* **2018**, *30*, 403–411.

(16) Suh, J.; Park, T.-E.; Lin, D.-Y.; Fu, D.; Park, J.; Jung, H. J.; Chen, Y.; Ko, C.; Jang, C.; Sun, Y.; Sinclair, R.; Chang, J.; Tongay, S.; Wu, J. Doping against the Native Propensity of MoS_2: Degenerate Hole Doping by Cation Substitution. *Nano Lett.* **2014**, *14*, 6976–

6982.

(17) Sim, D. M.; Kim, M.; Yim, S.; Choi, M.-J.; Choi, J.; Yoo, S.; Jung, Y. S. Controlled Doping of Vacancy-Containing Few-Layer MoS_2 via Highly Stable Thiol-Based Molecular Chemisorption. *ACS Nano* **2015**, *9*, 12115–12123.

(18) Xu, E. Z.; Liu, H. M.; Park, K.; Li, Z.; Losovyj, Y.; Starr, M.; Werbianskyj, M.; Fertig, H. A.; Zhang, S. X. P-Type Transition-Metal Doping of Large-Area MoS_2 Thin Films Grown by Chemical Vapor Deposition. *Nanoscale* **2017**, *9*, 3576–3584.

(19) Chen, C.-H.; Wu, C.-L.; Pu, J.; Chiu, M.-H.; Kumar, P.; Takenobu, T.; Li, L.-J. Hole Mobility Enhancement and p-Doping in Monolayer WSe_2 by Gold Decoration. *2D Mater.* **2014**, *1*, 034001.

(20) Zhou, H.; Wang, C.; Shaw, J. C.; Cheng, R.; Chen, Y.; Huang, X.; Liu, Y.; Weiss, N. O.; Lin, Z.; Huang, Y.; Duan, X. Large Area Growth and Electrical Properties of P-Type WSe_2 Atomic Layers. *Nano Lett.* **2015**, *15*, 709–713.

(21) Gao, Y.; Hong, Y.-L.; Yin, L.-C.; Wu, Z.; Yang, Z.; Chen, M.-L.; Liu, Z.; Ma, T.; Sun, D.-M.; Ni, Z.; Ma, X.-L.; Cheng, H.-M.; Ren, W. Ultrafast Growth of High-Quality Monolayer WSe_2 on Au. *Adv. Mater.* **2017**, *29*, 1700990.

(22) Li, S.; Wang, S.; Tang, D.-M.; Zhao, W.; Xu, H.; Chu, L.; Bando, Y.; Golberg, D.; Eda, G. Halide-Assisted Atmospheric Pressure Growth of Large WSe_2 and WS_2 Monolayer Crystals. *Appl. Mater. Today* **2015**, *1*, 60–66.

(23) Fang, H.; Chuang, S.; Chang, T. C.; Takei, K.; Takahashi, T.; Javey, A. High-Performance Single Layered WSe_2 p-FETs with Chemically Doped Contacts. *Nano Lett.* **2012**, *12*, 3788–3792.

(24) Kang, W. T.; Lee, I. M.; Yun, S. J.; Song, Y. I.; Kim, K.; Kim, D.-H.; Shin, Y. S.; Lee, K.; Heo, J.; Kim, Y.-M.; Lee, Y. H.; Yu, W. J. Direct Growth of Doping Controlled Monolayer WSe_2 by Selenium-Phosphorus Substitution. *Nanoscale* **2018**, *10*, 11397–

11402.

(25) Tosun, M.; Chan, L.; Amani, M.; Roy, T.; Ahn, G. H.; Taheri, P.; Carraro, C.; Ager, J. W.; Maboudian, R.; Javey, A. Air-Stable n-Doping of WSe_2 by Anion Vacancy Formation with Mild Plasma Treatment. *ACS Nano* **2016**, *10*, 6853–6860.

(26) Jeon, P. J.; Kim, J. S.; Lim, J. Y.; Cho, Y.; Pezeshki, A.; Lee, H. S.; Yu, S.; Min, S.-W.; Im, S. Low Power Consumption Complementary Inverters with n-MoS_2 and p-WSe_2 Dichalcogenide Nanosheets on Glass for Logic and Light-Emitting Diode Circuits. *ACS Appl. Mater. Interfaces* **2015**, *7*, 22333–22340.

(27) Cho, Y.; Park, J. H.; Kim, M.; Jeong, Y.; Yu, S.; Lim, J. Y.; Yi, Y.; Im, S. Impact of Organic Molecule-Induced Charge Transfer on Operating Voltage Control of Both n-MoS_2 and p-$MoTe_2$ Transistors. *Nano Lett.* **2019**, *19*, 2456–2463.

(28) Huang, J.-K.; Pu, J.; Hsu, C.-L.; Chiu, M.-H.; Juang, Z.-Y.; Chang, Y.-H.; Chang, W.-H.; Iwasa, Y.; Takenobu, T.; Li, L.-J. Large-Area Synthesis of Highly Crystalline WSe_2 Monolayers and Device Applications. *ACS Nano* **2014**, *8*, 923–930.

(29) Zhang, S.; Hill, H. M.; Moudgil, K.; Richter, C. A.; Walker, A. R. H.; Barlow, S.; Marder, S. R.; Hacker, C. A.; Pookpanratana, S. J. Controllable, Wide-Ranging n-Doping and p-Doping of Monolayer Group 6 Transition-Metal Disulfides and Diselenides. *Adv. Mater.* **2018**, *30*, 1806345.

(30) Lee, C.-H.; Lee, G.-H.; van der Zande, A. M.; Chen, W.; Li, Y.; Han, M.; Cui, X.; Arefe, G.; Nuckolls, C.; Heinz, T. F.; Guo, J.; Hone, J.; Kim, P. Atomically Thin p–n Junctions with van Der Waals Heterointerfaces. *Nat. Nanotechnol.* **2014**, *9*, 676–681.

(31) Li, M.-Y.; Shi, Y.; Cheng, C.-C.; Lu, L.-S.; Lin, Y.-C.; Tang, H.-L.; Tsai, M.-L.; Chu, C.-W.; Wei, K.-H.; He, J.-H.; Chang, W.-H.; Suenaga, K.; Li, L.-J. Epitaxial Growth of a Monolayer WSe_2-MoS_2 Lateral p-n Junction with an Atomically Sharp Interface. *Science* **2015**, *349*, 524–528.

(32) Aji, A. S.; Izumoto, M.; Suenaga, K.; Yamamoto, K.; Nakashima, H.; Ago, H. Two-Step Synthesis and Characterization of Vertically Stacked SnS–WS_2 and SnS–MoS_2 p–n Heterojunctions. *Phys. Chem. Chem. Phys.* **2018**, *20*, 889–897.

(33) Henning, A.; Sangwan, V. K.; Bergeron, H.; Balla, I.; Sun, Z.; Hersam, M. C.; Lauhon, L. J. Charge Separation at Mixed-Dimensional Single and Multilayer MoS_2/Silicon Nanowire Heterojunctions. *ACS Appl. Mater. Interfaces* **2018**, *10*, 16760–16767.

(34) Tan, D.; Wang, X.; Zhang, W.; Lim, H. E.; Shinokita, K.; Miyauchi, Y.; Maruyama, M.; Okada, S.; Matsuda, K. Carrier Transport and Photoresponse in GeSe/MoS_2 Heterojunction p–n Diodes. *Small* **2018**, *14*, 1704559.

(35) Kim, Y.; Ryu, J.; Park, M.; Kim, E. S.; Yoo, J. M.; Park, J.; Kang, J. H.; Hong, B. H. Vapor-Phase Molecular Doping of Graphene for High-Performance Transparent Electrodes. *ACS Nano* **2014**, *8*, 868–874.

(36) Morikawa, Y.; Iwata, K.; Terakura, K. Theoretical Study of Hydrogenation Process of Formate on Clean and Zn Deposited Cu(111) Surfaces. *Appl. Surf. Sci.* **2001**, *169*, 11–15.

(37) Gurarslan, A.; Yu, Y.; Su, L.; Yu, Y.; Suarez, F.; Yao, S.; Zhu, Y.; Ozturk, M.; Zhang, Y.; Cao, L. Surface-Energy-Assisted Perfect Transfer of Centimeter-Scale Monolayer and Few-Layer MoS_2 Films onto Arbitrary Substrates. *ACS Nano* **2014**, *8*, 11522–11528.

(38) Liu, X.; Qu, D.; Ryu, J.; Ahmed, F.; Yang, Z.; Lee, D.; Yoo, W. J. P-Type Polar Transition of Chemically Doped Multilayer MoS_2 Transistor. *Adv. Mater.* **2016**, *28*, 2345–2351.

(39) McDonnell, S.; Addou, R.; Buie, C.; Wallace, R. M.; Hinkle, C. L. Defect-Dominated Doping and Contact Resistance in MoS_2. *ACS Nano* **2014**, *8*, 2880–2888.

(40) Tsai, M.-Y.; Zhang, S.; Campbell, P. M.; Dasari, R. R.; Ba, X.; Tarasov, A.; Graham, S.; Barlow, S.; Marder, S. R.; Vogel, E. M. Solution-Processed Doping of Trilayer WSe_2 with Redox-Active Molecules. *Chem. Mater.* **2017**, *29*, 7296–7304.

(41) Chuang, H.-J.; Tan, X.; Ghimire, N. J.; Perera, M. M.; Chamlagain, B.; Cheng, M. M.-C.; Yan, J.; Mandrus, D.; Tománek, D.; Zhou, Z. High Mobility WSe_2 P- and n-Type Field-Effect Transistors Contacted by Highly Doped Graphene for Low-Resistance Contacts. *Nano Lett.* **2014**, *14*, 3594–3601.

(42) Li, Z.; Wang, T.; Lu, Z.; Jin, C.; Chen, Y.; Meng, Y.; Lian, Z.; Taniguchi, T.; Watanabe, K.; Zhang, S.; Smirnov, D.; Shi, S.-F. Revealing the Biexciton and Trion-Exciton Complexes in BN Encapsulated WSe_2. *Nat. Commun.* **2018**, *9*, 3719.

(43) Wu, Z.; Zhao, W.; Jiang, J.; Zheng, T.; You, Y.; Lu, J.; Ni, Z. Defect Activated Photoluminescence in WSe_2 Monolayer. *J. Phys. Chem. C* **2017**, *121*, 12294–12299.

(44) Jones, A. M.; Yu, H.; Ghimire, N. J.; Wu, S.; Aivazian, G.; Ross, J. S.; Zhao, B.; Yan, J.; Mandrus, D. G.; Xiao, D.; Yao, W.; Xu, X. Optical Generation of Excitonic Valley Coherence in Monolayer WSe_2. *Nat. Nanotechnol.* **2013**, *8*, 634–638.

(45) Chen, J.-W.; Lo, S.-T.; Ho, S.-C.; Wong, S.-S.; Vu, T.-H.-Y.; Zhang, X.-Q.; Liu, Y.-D.; Chiou, Y.-Y.; Chen, Y.-X.; Yang, J.-C.; Chen, Y.-C.; Chu, Y.-H.; Lee, Y.-H.; Chung, C.-J.; Chen, T.-M.; Chen, C.-H.; Wu, C.-L. A Gate-Free Monolayer WSe_2 Pn Diode. *Nat. Commun.* **2018**, *9*, 3143.

(46) Shi, Y.; Huang, J.-K.; Jin, L.; Hsu, Y.-T.; Yu, S. F.; Li, L.-J.; Yang, H. Y. Selective Decoration of Au Nanoparticles on Monolayer MoS_2 Single Crystals. *Sci. Rep.* **2013**, *3*, 1839.

(47) Loan, P. T. K.; Zhang, W.; Lin, C.-T.; Wei, K.-H.; Li, L.-J.; Chen, C.-H. Graphene/MoS_2 Heterostructures for Ultrasensitive Detection of DNA Hybridisation. *Adv. Mater.* **2014**, *26*, 4838–4844.

(48) Tarasov, A.; Zhang, S.; Tsai, M.-Y.; Campbell, P. M.; Graham, S.; Barlow, S.; Marder, S. R.; Vogel, E. M. Controlled Doping of Large-Area Trilayer MoS_2 with Molecular Reductants and Oxidants. *Adv. Mater.* **2015**, *27*, 1175–1181.

(49) Lin, J. D.; Han, C.; Wang, F.; Wang, R.; Xiang, D.; Qin, S.; Zhang, X.-A.; Wang, L.; Zhang, H.; Wee, A. T. S.; Chen, W. Electron-Doping-Enhanced Trion Formation in Monolayer Molybdenum Disulfide Functionalized with Cesium Carbonate. *ACS Nano* **2014**, *8*, 5323–5329.

(50) Bissett, M. A.; Konabe, S.; Okada, S.; Tsuji, M.; Ago, H. Enhanced Chemical Reactivity of Graphene Induced by Mechanical Strain. *ACS Nano* **2013**, *7*, 10335–10343.

(51) Lin, Y.-C.; Björkman, T.; Komsa, H.-P.; Teng, P.-Y.; Yeh, C.-H.; Huang, F.-S.; Lin, K.-H.; Jadczak, J.; Huang, Y.-S.; Chiu, P.-W.; Krasheninnikov, A. V.; Suenaga, K. Three-Fold Rotational Defects in Two-Dimensional Transition Metal Dichalcogenides. *Nat. Commun.* **2015**, *6*, 6736.

(52) Zhou, W.; Zou, X.; Najmaei, S.; Liu, Z.; Shi, Y.; Kong, J.; Lou, J.; Ajayan, P. M.; Yakobson, B. I.; Idrobo, J.-C. Intrinsic Structural Defects in Monolayer Molybdenum Disulfide. *Nano Lett.* **2013**, *13*, 2615–2622.

(53) Barja, S.; Refaely-Abramson, S.; Schuler, B.; Qiu, D. Y.; Pulkin, A.; Wickenburg, S.; Ryu, H.; Ugeda, M. M.; Kastl, C.; Chen, C.; Hwang, C.; Schwartzberg, A.; Aloni, S.; Mo, S.-K.; Frank Ogletree, D.; Crommie, M. F.; Yazyev, O. V.; Louie, S. G.; Neaton, J. B.; Weber-Bargioni, A. Identifying Substitutional Oxygen as a Prolific Point Defect in Monolayer Transition Metal Dichalcogenides. *Nat. Commun.* **2019**, *10*, 3382.

(54) Qiu, H.; Xu, T.; Wang, Z.; Ren, W.; Nan, H.; Ni, Z.; Chen, Q.; Yuan, S.; Miao, F.; Song, F.; Long, G.; Shi, Y.; Sun, L.; Wang, J.; Wang, X. Hopping Transport through Defect-Induced Localized States in Molybdenum Disulphide. *Nat. Commun.* **2013**, *4*, 2642.

(55) Okada, M.; Miyauchi, Y.; Matsuda, K.; Taniguchi, T.; Watanabe, K.; Shinohara, H.; Kitaura, R. Observation of Biexcitonic Emission at Extremely Low Power Density in Tungsten Disulfide Atomic Layers Grown on Hexagonal Boron Nitride. *Sci. Rep.* **2017**, *7*, 322.

(56) Ji, H. G.; Maruyama, M.; Aji, A. S.; Okada, S.; Matsuda, K.; Ago, H. Van Der Waals Interaction-Induced Photoluminescence Weakening and Multilayer Growth in Epitaxially Aligned WS_2. *Phys. Chem. Chem. Phys.* **2018**, *20*, 29790–29797.

(57) Chu, X. S.; Yousaf, A.; Li, D. O.; Tang, A. A.; Debnath, A.; Ma, D.; Green, A. A.; Santos, E. J. G.; Wang, Q. H. Direct Covalent Chemical Functionalization of Unmodified Two-Dimensional Molybdenum Disulfide. *Chem. Mater.* **2018**, *30*, 2112–2128.

(58) Li, D. O.; Gilliam, M. S.; Chu, X. S.; Yousaf, A.; Guo, Y.; Green, A. A.; Wang, Q. H. Covalent Chemical Functionalization of Semiconducting Layered Chalcogenide Nanosheets. *Mol. Syst. Des. Eng.* **2019**, *4*, 962–973.

(59) Zhang, H.; Li, C.; Wang, J.; Hu, W.; Zhang, D. W.; Zhou, P. Complementary Logic with Voltage Zero-Loss and Nano-Watt Power via Configurable MoS_2/WSe_2 Gate. *Adv. Funct. Mater.* **2018**, *28*, 1805171.

(60) Tosun, M.; Chuang, S.; Fang, H.; Sachid, A. B.; Hettick, M.; Lin, Y.; Zeng, Y.; Javey, A. High-Gain Inverters Based on WSe2 Complementary Field-Effect Transistors. *ACS Nano* **2014**, *8*, 4948–4953.

(61) Yu, L.; Zubair, A.; Santos, E. J. G.; Zhang, X.; Lin, Y.; Zhang, Y.; Palacios, T. High-Performance WSe_2 Complementary Metal Oxide Semiconductor Technology and Integrated Circuits. *Nano Lett.* **2015**, *15*, 4928–4934.

(62) Liu, S.; Yuan, K.; Xu, X.; Yin, R.; Lin, D.-Y.; Li, Y.; Watanabe, K.; Taniguchi, T.; Meng, Y.; Dai, L.; Ye, Y. Hysteresis-Free Hexagonal Boron Nitride Encapsulated 2D Semiconductor Transistors, NMOS and CMOS Inverters. *Adv. Electron. Mater.* **2018**, *5*, 1800419.

(63) Resta, G. V.; Balaji, Y.; Lin, D.; Radu, I. P.; Catthoor, F.; Gaillardon, P.-E.; De Micheli, G. Doping-Free Complementary Logic Gates Enabled by Two-Dimensional Polarity-Controllable Transistors. *ACS Nano* **2018**, *12*, 7039–7047.

(64) Li, H.-M.; Lee, D.; Qu, D.; Liu, X.; Ryu, J.; Seabaugh, A.; Yoo, W. J. Ultimate Thin Vertical p–n Junction Composed of Two-Dimensional Layered Molybdenum Disulfide. *Nat. Commun.* **2015**, *6*, 6564.

Chapter 6

Conclusions and Future Outlook

6.1. Conclusions

In this thesis, synthesis and applications of 2D TMD materials are demonstrated. In Chapter 3, epitaxial growth of WS_2 on c-plane sapphire substrate using H_2 carrier gas is demonstrated. By strong reducing effect of H_2 on the reaction of precursors, crystal quality of WS_2 is significantly improved. H_2 gas also changes the surface termination of c-plane sapphire, resulting in epitaxial growth of WS_2 on sapphire. Epitaxially grown WS_2 shows atomically smooth stitching between merging grains, which is revealed by detailed STEM study, and they show improved chemical stability against oxidation as well as good electrical transport properties across seamlessly stitched grain boundaries.

In Chapter 4, influence of c-plane sapphire substrate on the growth behavior of WS_2 is investigated. Due to similar hexagonal lattice structures of c-plane sapphire and WS_2, larger lattice strain is induced in the epitaxially aligned grains by strong van der Waals interaction with underlying sapphire. It causes PL quenching and preferential overlayer deposition on the epitaxially aligned WS_2 grains. Low-temperature optical study and FET measurement reveal that van der Waals interaction-induced lattice strain does not cause a degradation of crystal quality. DFT calculations on lattice orientation-dependent relaxation energies on sapphire well support the experimental data.

In Chapter 5, chemical tuning of electrical transport polarity of CVD grown WSe_2 is demonstrated. By using 4-NBD and DETA molecules as p- and n-type dopants, electrical polarity is successfully controlled to p- and n-type, respectively. In addition, the effective carrier mobility significantly increases after each doping treatment, and DFT calculation supports the observed doping. Using chemically doped WSe_2 FET devices, a CMOS inverter circuit is fabricated, which shows high voltage gain as well as extremely low power consumption. Furthermore, by combining chemical doping and lithography techniques, a p-n junction is fabricated within a single triangle grain of WSe_2, being half of the grain selectively p-doped and another half n-doped. This p-n junction shows clear rectification behavior together with light response.

6.2. Future outlook

As a result of devoted effort by many researchers, TMD research has dramatically advanced for last several years. Recent development of CVD technology realized wafer-scale synthesis of uniform TMD films.[1,2] Also new physical properties have been continuously discovered. Especially, optical and electronic properties of twisted TMD heterostructures with unique superlattice formation have been on the focus of many researchers.[3–5] As already known, atomically thin TMD monolayers possess large spin-orbit splitting in their valence and conduction bands.[6] Existence of degenerate energy states in a *K* valley makes TMDs have an additional spin degree of freedom. Furthermore, TMDs have degenerate inequivalent *K* points (*K* and *K*' or K^+ and K^-) in their hexagonal Brillouin zone which differently respond to circularly polarized light.[7] Thus, this valley-dependent optical selectivity lets TMDs have an additional valley degree of freedom. Consequently, the spin and valley degree of freedoms observed in TMDs cause unique optical and electronic properties, such as formation of spin,

valley polarized exciton and spin, valley hall effect.[8] Additional degree of freedoms in carriers make it possible to realize new paradigm of data manipulation with orders of magnitude higher processing capacity by using combination of electrical charge, spin, and valley. To realize this, further research is necessary. First, the crystal quality of CVD grown TMDs must be improved. In spite of the development of CVD technology, still the defect density in CVD-grown TMD crystals is high. In carrier dynamics in conduction and valence bands, these structural defects act as scattering sites and degrade the polarization controllability. Thus, more study is needed to further improve the crystal quality of CVD TMDs. Second, good insulating materials are necessary. As proved by many literatures, TMDs show more intrinsic and improved physical properties when encapsulated between h-BN layers.[9–11] Due to the subnanometer thickness of monolayer TMDs and their resultant sensitivity to the dielectric surrounding, it is very important to protect TMDs using an insulator. For this, h-BN, which is a 2D insulator without dangling bond, is being widely used. In spite of the development of h-BN CVD technique[12–14], it is still difficult to grow large, uniform, and highly crystalline h-BN so that most of people are using the small flakes of exfoliated h-BN. Therefore, further development of h-BN synthesis technique is highly required for continuing advance of 2D research. As insulating materials, there are additional choices other than h-BN, such as large band gap 2D materials, $Cu(OH)_2$, $Ni(OH)_2$, $Mg(OH)_2$, TaIc, GaS,[15] covalent organic frameworks,[16] and insulating 2D polymers.[17] Third, for continuing thrive of 2D research, it will be also important to keep looking for new physical properties from known materials and new materials with interesting properties. Research on the stacking of various 2D materials to investigate emergence of new physical property (Twistronics) is just on the beginning stage. There are many on-going works in this field so that significant advance is expected in the near future. There are other emerging 2D materials, for example, Nb_3X_8 family (X = Cl, Be, or I).[18] Similar to TMDs, Nb_3X_8 also have a two-dimensional layered

structure. Theoretical studies have expected variable band gap and ferromagnetism depending on their composition.[18] Also 2D perovskites have attracted attention. When thinned down to nanometer thickness, perovskites show different physical properties from the bulk because of the quantum confinement effect.[19–21] From this, we can expect thinning of various materials to see their property change in quantum confined condition.[22] Furthermore, there are many other promising 2D candidates, such as synthetic 2D polymer,[17] graphyne,[23,24] borophene,[25–27] germanene,[28,29] phosphorene,[30,31] and MXenes,[32,33] which have been proved to possess promising physical properties although most of them need more detailed experimental investigations.

References

(1) Yu, H.; Liao, M.; Zhao, W.; Liu, G.; Zhou, X. J.; Wei, Z.; Xu, X.; Liu, K.; Hu, Z.; Deng, K.; Zhou, S.; Shi, J.-A.; Gu, L.; Shen, C.; Zhang, T.; Du, L.; Xie, L.; Zhu, J.; Chen, W.; Yang, R.; Shi, D.; Zhang, G. Wafer-Scale Growth and Transfer of Highly-Oriented Monolayer MoS_2 Continuous Films. *ACS Nano* **2017**, *11*, 12001–12007.

(2) Kang, K.; Xie, S.; Huang, L.; Han, Y.; Huang, P. Y.; Mak, K. F.; Kim, C.-J.; Muller, D.; Park, J. High-Mobility Three-Atom-Thick Semiconducting Films with Wafer-Scale Homogeneity. *Nature* **2015**, *520*, 656–660.

(3) Jin, C.; Regan, E. C.; Yan, A.; Iqbal Bakti Utama, M.; Wang, D.; Zhao, S.; Qin, Y.; Yang, S.; Zheng, Z.; Shi, S.; Watanabe, K.; Taniguchi, T.; Tongay, S.; Zettl, A.; Wang, F. Observation of Moiré Excitons in WSe_2/WS_2 Heterostructure Superlattices. *Nature* **2019**, *567*, 76–80.

(4) Unuchek, D.; Ciarrocchi, A.; Avsar, A.; Watanabe, K.; Taniguchi, T.; Kis, A. Room-Temperature Electrical Control of Exciton Flux in a van der Waals Heterostructure. *Nature* **2018**, *560*, 340–344.

(5) Kunstmann, J.; Mooshammer, F.; Nagler, P.; Chaves, A.; Stein, F.; Paradiso, N.; Plechinger, G.; Strunk, C.; Schüller, C.; Seifert, G.; Reichman, D. R.; Korn, T. Momentum-Space Indirect Interlayer Excitons in Transition-Metal Dichalcogenide van der Waals Heterostructures. *Nat. Phys.* **2018**, *14*, 801–805.

(6) Zhu, Z. Y.; Cheng, Y. C.; Schwingenschlögl, U. Giant Spin-Orbit-Induced Spin Splitting in Two-Dimensional Transition-Metal Dichalcogenide Semiconductors. *Phys. Rev. B* **2011**, *84*, 153402.

(7) Schaibley, J. R.; Yu, H.; Clark, G.; Rivera, P.; Ross, J. S.; Seyler, K. L.; Yao, W.; Xu, X.

Valleytronics in 2D Materials. *Nat. Rev. Mater.* **2016**, *1*, 16055.

(8) Mak, K. F.; McGill, K. L.; Park, J.; McEuen, P. L. The Valley Hall Effect in MoS_2 Transistors. *Science* **2014**, *344*, 1489–1492.

(9) Uchiyama, Y.; Kutana, A.; Watanabe, K.; Taniguchi, T.; Kojima, K.; Endo, T.; Miyata, Y.; Shinohara, H.; Kitaura, R. Momentum-Forbidden Dark Excitons in HBN-Encapsulated Monolayer MoS_2. *npj 2D Mater. Appl.* **2019**, *3*, 26.

(10) Li, Z.; Wang, T.; Lu, Z.; Jin, C.; Chen, Y.; Meng, Y.; Lian, Z.; Taniguchi, T.; Watanabe, K.; Zhang, S.; Smirnov, D.; Shi, S.-F. Revealing the Biexciton and Trion-Exciton Complexes in BN Encapsulated WSe_2. *Nat. Commun.* **2018**, *9*, 3719.

(11) Liu, S.; Yuan, K.; Xu, X.; Yin, R.; Lin, D.-Y.; Li, Y.; Watanabe, K.; Taniguchi, T.; Meng, Y.; Dai, L.; Ye, Y. Hysteresis-Free Hexagonal Boron Nitride Encapsulated 2D Semiconductor Transistors, NMOS and CMOS Inverters. *Adv. Electron. Mater.* **2018**, *5*, 1800419.

(12) Uchida, Y.; Nakandakari, S.; Kawahara, K.; Yamasaki, S.; Mitsuhara, M.; Ago, H. Controlled Growth of Large-Area Uniform Multilayer Hexagonal Boron Nitride as an Effective 2D Substrate. *ACS Nano* **2018**, *12*, 6236–6244.

(13) Uchida, Y.; Iwaizako, T.; Mizuno, S.; Tsuji, M.; Ago, H. Epitaxial Chemical Vapour Deposition Growth of Monolayer Hexagonal Boron Nitride on a Cu(111)/Sapphire Substrate. *Phys. Chem. Chem. Phys.* **2017**, *19*, 8230–8235.

(14) Lee, J. S.; Choi, S. H.; Yun, S. J.; Kim, Y. I.; Boandoh, S.; Park, J.-H.; Shin, B. G.; Ko, H.; Lee, S. H.; Kim, Y.-M.; Lee, Y. H.; Kim, K. K.; Kim, S. M. Wafer-Scale Single-Crystal Hexagonal Boron Nitride Film via Self-Collimated Grain Formation. *Science* **2018**, *362*, 817–821.

(15) Harvey, A.; Backes, C.; Boland, J. B.; He, X.; Griffin, A.; Szydlowska, B.; Gabbett, C.; Donegan, J. F.; Coleman, J. N. Non-Resonant Light Scattering in Dispersions of 2D

Nanosheets. *Nat. Commun.* **2018**, *9*, 4553.

(16) Miró, P.; Audiffred, M.; Heine, T. An Atlas of Two-Dimensional Materials. *Chem Soc Rev* **2014**, *43*, 6537–6554.

(17) Servalli, M.; Schlüter, A. D. Synthetic Two-Dimensional Polymers. *Annu. Rev. Mater. Res.* **2017**, *47*, 361–389.

(18) Kim, B. J.; Jeong, B. J.; Oh, S.; Chae, S.; Choi, K. H.; Nanda, S. S.; Nasir, T.; Lee, S. H.; Kim, K.-W.; Lim, H. K.; Chi, L.; Choi, I. J.; Hong, M.-K.; Yi, D. K.; Yu, H. K.; Lee, J.-H.; Choi, J.-Y. Structural and Electrical Properties of Nb_3I_8 Layered Crystal. *Phys. Status Solidi RRL – Rapid Res. Lett.* **2019**, *13*, 1800448.

(19) Jagielski, J.; Kumar, S.; Yu, W.-Y.; Shih, C.-J. Layer-Controlled Two-Dimensional Perovskites: Synthesis and Optoelectronics. *J. Mater. Chem. C* **2017**, *5*, 5610–5627.

(20) Dou, L.; Wong, A. B.; Yu, Y.; Lai, M.; Kornienko, N.; Eaton, S. W.; Fu, A.; Bischak, C. G.; Ma, J.; Ding, T.; Ginsberg, N. S.; Wang, L.-W.; Alivisatos, A. P.; Yang, P. Atomically Thin Two-Dimensional Organic-Inorganic Hybrid Perovskites. *Science* **2015**, *349*, 1518–1521.

(21) Erkılıç, U.; Solís-Fernández, P.; Ji, H. G.; Shinokita, K.; Lin, Y.-C.; Maruyama, M.; Suenaga, K.; Okada, S.; Matsuda, K.; Ago, H. Vapor Phase Selective Growth of Two-Dimensional Perovskite/WS_2 Heterostructures for Optoelectronic Applications. *ACS Appl. Mater. Interfaces* **2019**, *11*, 40503–40511.

(22) Forti, S.; Link, S.; Stöhr, A.; Niu, Y.; Zakharov, A. A.; Coletti, C.; Starke, U. Semiconductor to Metal Transition in Two-Dimensional Gold and Its van der Waals Heterostack with Graphene. *Nat. Commun.* **2020**, *11*, 2236.

(23) Li, Z.; Smeu, M.; Rives, A.; Maraval, V.; Chauvin, R.; Ratner, M. A.; Borguet, E. Towards Graphyne Molecular Electronics. *Nat. Commun.* **2015**, *6*, 6321.

(24) Li, Q.; Li, Y.; Chen, Y.; Wu, L.; Yang, C.; Cui, X. Synthesis of γ-Graphyne by

Mechanochemistry and Its Electronic Structure. *Carbon* **2018**, *136*, 248–254.

(25) Mannix, A. J.; Zhang, Z.; Guisinger, N. P.; Yakobson, B. I.; Hersam, M. C. Borophene as a Prototype for Synthetic 2D Materials Development. *Nat. Nanotechnol.* **2018**, *13*, 444–450.

(26) Mannix, A. J.; Zhou, X.-F.; Kiraly, B.; Wood, J. D.; Alducin, D.; Myers, B. D.; Liu, X.; Fisher, B. L.; Santiago, U.; Guest, J. R.; Yacaman, M. J.; Ponce, A.; Oganov, A. R.; Hersam, M. C.; Guisinger, N. P. Synthesis of Borophenes: Anisotropic, Two-Dimensional Boron Polymorphs. *Science* **2015**, *350*, 1513–1516.

(27) Sun, H.; Li, Q.; Wan, X. G. First-Principles Study of Thermal Properties of Borophene. *Phys. Chem. Chem. Phys.* **2016**, *18*, 14927–14932.

(28) Acun, A.; Zhang, L.; Bampoulis, P.; Farmanbar, M.; van Houselt, A.; Rudenko, A. N.; Lingenfelder, M.; Brocks, G.; Poelsema, B.; Katsnelson, M. I.; Zandvliet, H. J. W. Germanene: The Germanium Analogue of Graphene. *J. Phys. Condens. Matter* **2015**, *27*, 443002.

(29) Zhang, L.; Bampoulis, P.; Rudenko, A. N.; Yao, Q.; van Houselt, A.; Poelsema, B.; Katsnelson, M. I.; Zandvliet, H. J. W. Structural and Electronic Properties of Germanene on MoS_2. *Phys. Rev. Lett.* **2016**, *116*. 256804.

(30) Carvalho, A.; Wang, M.; Zhu, X.; Rodin, A. S.; Su, H.; Castro Neto, A. H. Phosphorene: From Theory to Applications. *Nat. Rev. Mater.* **2016**, *1*, 16061.

(31) Kou, L.; Chen, C.; Smith, S. C. Phosphorene: Fabrication, Properties, and Applications. *J. Phys. Chem. Lett.* **2015**, *6*, 2794–2805.

(32) Anasori, B.; Lukatskaya, M. R.; Gogotsi, Y. 2D Metal Carbides and Nitrides (MXenes) for Energy Storage. *Nat. Rev. Mater.* **2017**, *2*, 16098.

(33) Khazaei, M.; Ranjbar, A.; Arai, M.; Sasaki, T.; Yunoki, S. Electronic Properties and Applications of MXenes: A Theoretical Review. *J. Mater. Chem. C* **2017**, *5*, 2488–2503.

Acknowledgements

First, I would like to express my gratitude to Prof. Ago, who guided my pursuing PhD degree with kindness and patience for 5 years. Whenever I faced problems, Prof. Ago supported me to solve the problems and go through. Without this support, my PhD study must have been much more difficult. I also thank Prof. Ago for supporting my collaborations with nice research groups, and supporting my joining academic conferences and internship in UK.

I thank my collaborators, Dr. Kazu Suenaga, Prof. Susumu Okada, Prof. Kazunari Matsuda, Prof. Kosuke Nagashio, Prof. Yasumitsu Miyata, Dr. Yung-Chang Lin, Dr. Olga Kazakova, Dr. Vishal Panchal and Dr. Mina Maruyama for their dedicated collaborations and valuable comments.

I also thank our group members. First, I would like to thank Dr. Pablo Solís-Fernández who taught me valuable experimental skills and techniques in research. Thanks to his advices, I could learn a lot. I also appreciate Hino san who kindly supported my RA work for three years. Without her kindness, it must have been more tough. I thank Aji, Shiiba and Nakandakari who gave me valuable memories in Japan. I thank Dr. Uchida and Dr. Aji for valuable experimental advices. I thank Alexander Budiman Taslim Hayashi for coloring my Japanese life. And thank Ufuk for being my the best running mate of PhD course. I also thank Fukamachi san and Kawahara san for their kindly supporting the research. To all of the lab members, Nakano san, Ding san, Kinoshita, Suenaga, Izumoto, Terao, Koyanagi, Tanaka, Oyama, Akiyama, Murase, Motoyama, Honda, Watanabe, Kuriyamoto, I thank their kindness and helps. And wish good luck to Rasel and Hsin for their successful new start.

I would like to express my appreciation to JASSO and Kuma international scholarship foundations for financial support. Also, I appreciate Prof. Ago for supporting my PhD study by offering a RA position. During RA work, I could experience various interesting experiments and learn a lot.

Finally, I express sincere gratitude to my family in Korea who always dedicatedly supported my study in Japan.

List of publications

• Chapter 3

Ji, H. G.; Lin, Y.-C.; Nagashio, K.; Maruyama, M.; Solís-Fernández, P.; Sukma Aji, A.; Panchal, V.; Okada, S.; Suenaga, K.; Ago, H. Hydrogen-Assisted Epitaxial Growth of Monolayer Tungsten Disulfide and Seamless Grain Stitching. *Chem. Mater.* **2018**, *30*, 403–411.

• Chapter 4

Ji, H. G.; Maruyama, M.; Aji, A. S.; Okada, S.; Matsuda, K.; Ago, H. Van der Waals Interaction-Induced Photoluminescence Weakening and Multilayer Growth in Epitaxially Aligned WS_2. *Phys. Chem. Chem. Phys.* **2018**, *20*, 29790–29797.

• Chapter 5

Ji, H. G.; Solís-Fernández, P.; Yoshimura, D.; Maruyama, M.; Endo, T.; Miyata, Y.; Okada, S.; Ago, H. Chemically Tuned p- and n-Type WSe_2 Monolayers with High Carrier Mobility for Advanced Electronics. *Adv. Mater.* **2019**, *31*, 1903613.

• Publications not included in this thesis

[1] Aji, A. S.; Solís-Fernández, P.; **Ji, H. G**.; Fukuda, K.; Ago, H. High Mobility WS_2 Transistors Realized by Multilayer Graphene Electrodes and Application to High Responsivity Flexible Photodetectors. *Adv. Funct. Mater.* **2017**, *27*, 1703448.

[2] Suenaga, K.; **Ji, H. G**.; Lin, Y.-C.; Vincent, T.; Maruyama, M.; Aji, A. S.; Shiratsuchi, Y.; Ding, D.; Kawahara, K.; Okada, S.; Panchal, V.; Kazakova, O.; Hibino, H.; Suenaga, K.; Ago, H. Surface-Mediated Aligned Growth of Monolayer MoS_2 and In-Plane Heterostructures with Graphene on Sapphire. *ACS Nano* **2018**, *12*, 10032–10044.

[3] Erkılıç, U.; Solís-Fernández, P.; **Ji, H. G**.; Shinokita, K.; Lin, Y.-C.; Maruyama, M.; Suenaga, K.; Okada, S.; Matsuda, K.; Ago, H. Vapor Phase Selective Growth of Two-Dimensional Perovskite/WS_2 Heterostructures for Optoelectronic Applications. *ACS Appl. Mater. Interfaces* **2019**, *11*, 40503–40511.

[4] Lin, Y.-C.; **Ji, H. G**.; Chang, L.-J.; Chang, Y.-P.; Liu, Z.; Lee, G.-D.; Chiu, P.-W.; Ago, H.; Suenaga, K. Scanning Moiré Fringe Method: A Superior Approach to Perceive Defects, Interfaces, and Distortion in 2D Materials. *ACS Nano* **2020**, *14*, 6034-6042.

[5] Erkılıç, U.; **Ji, H. G**.; Ago, H. One-step vapour phase growth of two-dimensional formamidinium-based perovskite and its hot carrier dynamics. *In revision*